

Structure and dynamics of the MAGUK core of PSD-95

Jun Zhang

A dissertation submitted to the faculty of the University of North Carolina at Chapel Hill in partial fulfillment of the requirements for the degree of Doctor of Philosophy in the Department of Biochemistry and Biophysics.

Chapel Hill

2011

Approved by:

Andrew L. Lee, Advisor

Sharon Campbell, Reader

Edward Collins, Reader

Hengming Ke, Reader

Brian Kuhlman, Reader

© 2011

Jun Zhang

ALL RIGHTS RESERVED

Abstract

JUN ZHANG: Structure and dynamics of the MAGUK core of PSD-95

(Under the direction of Andrew L. Lee)

Protein allostery plays central roles in regulation of enzyme catalysis, signaling conduction and cellular metabolism. In this research, the interdomain allostery of postsynaptic density protein 95 (PSD-95), a key component of the postsynapse, was studied using NMR and other biophysical methods. Previous research has identified numerous PSD-95 interaction partners and revealed many PSD-95 mediated biological functions. Interestingly, interdomain allostery within PSD-95 has been found between PDZ3 and the following SH3/GK, and these allosteric events are regulated by phosphorylation. However, the structural mechanism of interdomain allostery and phosphorylation regulation is not addressed by *in vivo* studies on biological functions or *in vitro* studies on excised domains. In this dissertation, we studied the structural and dynamic effects of phosphorylation at the PDZ3/SH3 linker (Y397, S415 and S418). Upon phosphorylation, we found that the C-extension α -helix of PDZ3 is unfolded and undocked. We further examined the PDZ3-SH3 construct and showed that phosphorylation interrupts the domain interaction between PDZ3 and SH3. Using chemical shift perturbation and paramagnetic relaxation enhancement, we identified the PDZ3-SH3 interface. These experiments also suggested that CRIPT binding moves PDZ3 away from SH3. To understand interdomain allostery, we modeled the PDZ3-SH3-GK

structure using SAXS. Consistent with PRE results, we found PDZ3 is mainly docked to the Hook domain region of the SH3 domain, and CRIPT binding reshuffles the domain packing between PDZ3 and SH3-GK. To obtain a high resolution structural model of PDZ3-SH3-GK, we carried out Rosetta simulations in the presence of PRE and chemical shift perturbation constraints. We found that the PDZ3 domain uses its peptide binding groove to interact with the PDZ3-SH3 linker. This interaction brings PDZ3 close to SH3, whereas it can be disrupted by CRIPT binding. This Rosetta model also reveals that the positively charged face of the Hook domain, which is the binding interface for calmodulin, is masked by the PDZ3 domain. Therefore the model provides a basis for understanding interdomain allostery between SH3 and PDZ3. In this research we also discussed the possible mechanism by which PDZ3 and GK allostery is transferred.

To my maternal grandfather, Jiuding Chang,
whose respect for education and thirst for knowledge have encouraged me to pursue
achievement.

Acknowledgements

This dissertation would not have been finished without the support from a large network of persons. First and foremost, I want to express my utmost gratitude to my advisor Andrew Lee. During these five years, Drew has shared his scientific expertise with me, trained me for experimental techniques and cultured my scientific vision. As an international student, I received valuable help from Drew to improve my language.

I am grateful to my committee, Sharon Campbell, Edward Collins, Hengming Ke and Brian Kuhlman. I have benefited from their broad expertise and valuable suggestions, which greatly facilitated the project. Specially, Ed and Hengming gave me the opportunity to receive training of crystallography. Brian helped us with molecular dynamic simulations and Sharon helped us with protein phosphorylation and shared her expertise in NMR.

I would like to thank my classmates Steven Lewis and Oana Lungu in Brian's lab, who wrote and debugged the MD simulation program for me. I also want to thank Dorothy Erie and her student Dan Burke. I am very grateful that she taught me in person to use AFM. I would like to thank Huanchen Wang in Hengming Ke lab for technique support in crystallography, Dan Cline in Scott Singleton lab for training me for peptide synthesis and Finith Jernigan in David Lawrence lab for teaching me to use peptide synthesis machine.

I also would like to show my gratitude to individuals who provide us with facilities. I would like to thank Karl Koshlap and Greg Young for NMR technique assistance, Ashutosh Tripathy for macromolecular interaction facility, Steven Weigand and Xiaobing Zuo at Advanced Photon Source of National lab for SAXS data collection, and Brenda Temple for bioinformatics analysis.

It is a pleasure to thank my Lee lab members, especially Matthew Whitley who was my rotation tutor, Randall Mauldin and Josh Boyer who shared their valuable NMR expertise. I still receive their help even after they graduated. I also want to thank Tina Clay for preparing constructs and managing the lab, Mary Carroll, Tony Law and Chad Petit, Paul Sapienza, and Leanna Steier for providing me comfortable working environment.

The last but not the least, I am indebted to my family, my parents, my younger sister and my grandmother, whom I haven't seen for past four years.

Table of Contents

List of Tables	xii
List of Figures	xiii
List of Abbreviations and Symbols.....	xv
1. Introduction.....	1
1.1 Introduction to PDZ domains.....	2
1.2 PSD-95	5
1.3 Interdomain allostery and regulation of PSD-95.....	10
1.4 hPTP1E PDZ2	13
1.5 Overview of this work.....	13
1.6 NMR relaxation and protein dynamics	14
1.6.1 ps-ns timescale dynamics	17
1.6.2 CPMG relaxation dispersion	20
1.6.3 Application of PRE to protein structure and dynamics studies	24
1.6.4 Small Angle X-ray Scattering.....	28
2. Phosphorylation of a PDZ domain extension modulates binding affinity and interdomain interactions in the PSD-95 MAGUK.....	32
2.1 Introduction	32
2.2 Experimental Procedures.....	36
2.2.1 Protein expression and purification	36
2.2.2 Peptide synthesis.....	38
2.2.3 Isothermal Titration Calorimetry experiments	38
2.2.4 NMR assignments and relaxation experiments	38

2.2.5 SEA-HSQC experiments	39
2.3 Results	40
2.3.1 Phosphorylation of Y397 and purification of phosphorylated PDZ3	40
2.3.2 Phosphorylation-induced undocking of $\alpha 3$ lowers affinity for CRIPT ligand .	41
2.3.3 Phosphorylation of Y397 increases disorder in $\alpha 3$	44
2.3.4 Phosphorylation disrupts PDZ3-SH3 association.....	47
2.4 Discussion	50
2.4.1 Regulation in PDZ domains	50
2.4.2 Phosphorylation at Y397 allosterically regulates C-terminus binding.....	51
2.4.3 Phosphorylation tunes interdomain interactions in the PDZ3-SH3-GK MAGUK core	52
2.5 Concluding remarks	54
2.6 Acknowledgements	55
3. NMR study of allostery within PSD-95.....	56
3.1 Introduction	56
3.2 Experimental Procedures.....	60
3.2.1 Plasmid constructs.	60
3.2.2 Protein expression and purification.	60
3.2.3 Peptide synthesis.....	61
3.2.4 NMR experiments.....	61
3.2.5 Small angle X-ray scattering experiments.....	62
3.2.6 Rosetta molecular dynamics simulation.	63
3.3 Results	65
3.3.1 PDZ3 is adjacent to SH3 in tertiary structure and brought away by CRIPT peptide binding.	65
3.3.2 PDZ3 does not form stable and static complex with SH3-GK.....	69

3.3.3 PDZ3 is not docked into MAP1A binding groove.	70
3.3.4 PSG Structural modeling by SAXS.	71
3.3.5 Intradomain Flexibility of SH3-GK.	75
3.3.6 Preliminary modeling results of PSG using Rosetta.	77
3.4 Discussion	80
3.4.1 Interdomain contacts between PDZ3 and the Hook domain	81
3.4.2 The Roles of the PDZ3/SH3 linker.....	81
3.4.3 Allostery of PDZ3/GK and putative function of Hook domain	83
3.5 Acknowledgements	84
4. Crystallographic and NMR evaluation of the impact of peptide binding to the second PDZ domain of PTP1E	86
4.1 Introduction	86
4.2 Experimental Procedures.....	90
4.2.1 Protein expression and purification.	90
4.2.2 Peptide preparation.	91
4.2.3 Crystallization.....	91
4.2.4 Structure determination and refinement.	91
4.2.5 NMR spectroscopy.	93
4.2.6 RDC data collection and analysis.....	93
4.2.7 Binding affinities and populations.....	94
4.2.8 ¹⁵ N Relaxation dispersion.....	94
4.2.9 ps-ns dynamics.	95
4.3 Results and Discussion.....	96
4.3.1 Crystal structures of apo and peptide-bound PDZ2.....	96
4.3.2 Structure validation through solution RDCs.	101

4.3.3 Long-range “pure” dynamic propagation in PDZ2 also results from APC peptide binding.	103
4.3.4 μ s-ms timescale peptide binding dynamics.	106
4.4 Summary	113
4.5 Acknowledgements	114
Appendices.....	115
Bibliography	125

List of Tables

Table 1.1: Interdomain allostery with in PSD-MAGUKs	12
Table 1.2: Phosphorylation sites in PSD-95	12
Table 2.1: ITC binding parameters for PDZ3 and phosphoPDZ3	44
Table 3.1: Radius of gyration.....	71
Table 4.1: Data collection statistics	92
Table 4.2: Structure refinement statistics.....	96
Table 4.3: RMSDs of published PTP1E PDZ2 structures and crystal structures	100
Table 4.4: Q-factors calculated by fitting RDC data to structural models.....	102
Table 4.5: Contingency table of APC and RA-GEF2 induced ΔS^2_{axis}	106
Table 4.6: Local fitting results of 5% RA-GEF2 bound PDZ2 relaxation dispersion data	111
Table 4.7: Local fitting results of 5% APC bound PDZ2 relaxation dispersion data.....	112
Table 4.8: Global fitting results of 50% RA-GEF2 bound PDZ2 relaxation dispersion data.....	113
Table S4.1: Global fitting results of 5% RA-GEF2 bound PDZ2 relaxation dispersion data.....	117
Table S4.2: Global fitting results of 5% APC bound PDZ2 relaxation dispersion data.	118
Table S4.3. Residues for which RDCs values were used in Q-factor calculations.	119

List of Figures

Figure 1.1: The representative structure of PDZ domains	3
Figure 1.2: Domain architecture of PSD-95 like proteins	6
Figure 1.3: The crystal structure of the PDZ1/PDZ2 tandem.....	7
Figure 1.4: The crystal structure of the SH3-GK tandem.....	9
Figure 1.5: Timescales of protein dynamics and appropriate NMR methods	16
Figure 1.6: Dipole-dipole interaction and vector orientation.....	17
Figure 1.7: Impact of exchange rate on NMR lineshape	21
Figure 1.8: Paramagnetic labeling chemicals	25
Figure 2.1: Domain architecture of PSD-95	33
Figure 2.2: Purification of phosphoPDZ3.....	41
Figure 2.3: Chemical shift perturbation of Y397 phosphorylation.....	42
Figure 2.4: Linear resonance pattern of PDZ3, phosphoPDZ3 and $\Delta 7\text{ct } ^{15}\text{N}$ -HSQCs	43
Figure 2.5: C_{α} chemical shift differences of PDZ3 and phosphoPDZ3 relative to random coil.....	45
Figure 2.6: Backbone amide order parameters	46
Figure 2.7: T_2 analysis of PD3-SH3, Y397E and Y397E/S415E/S418E mutants.....	48
Figure 2.8: Schematic explanation of function of Y397, S415 and S418 phosphorylation in PSD-95.....	54
Figure 3.1: Minimal chemical shift perturbation on PDZ3 by PDZ3-SH3 packing.....	65
Figure 3.2: PDZ3 PRE perturbation by C445 MTSL labeling of PDZ3-SH3	66
Figure 3.3: PRE perturbation changes resulting from CRIPT peptide binding and PDZ3/S418 linker replacement.....	68
Figure 3.4: HSQC peak intensity statistics of PDZ3-SH3-GK.....	69
Figure 3.5: Intensity ratio of paramagnetic and diamagnetic spectrum of Y604C	71

Figure 3.6: SAXS scattering curves of apo and CRIPT bound PSG	72
Figure 3.7: Radius gyration distributions of apo and CRIPT bound PSG	73
Figure 3.8: EOM fitting results.....	74
Figure 3.9: Paramagnetic perturbations on W507 and W499.....	76
Figure 3.10: location of paramagnetic labeling sites	77
Figure 3.11: Rosetta modeling of PSG	78
Figure 3.12: Paramagnetic perturbation on PDZ3 ^{S414C} by S414C MTLs labeling	82
Figure 4.1: Cartoon representation of PDZ2 crystal structures	97
Figure 4.2: Methyl-bearing side-chain dynamics changes	105
Figure 4.3: Graphical comparison of side-chain dynamic changes	105
Figure 4.4: Two-state binding of RA-GEF2 and APC peptides	109
Figure S2.1: Solvent accessibility analysis by NMR.....	116
Figure S4.1: Crystal packing within the asymmetric unit for apo PDZ2.....	121
Figure S4.2: Involvement of residue 30-33 in crystal packing.....	121
Figure S4.3: Determination of K_D for PDZ2-APC peptide interaction by NMR titration	122
Figure S4.4: Distribution of residues used in calculation of Q-factors.....	123
Figure S4.5: Internal correlation time (τ_c) changes	124

List of Abbreviations and Symbols

ADP	adenosine-5'-diphosphate
AFM	atomic force microscope
APC	adenomatous polyposis coli-protein
ATP	adenosine-5'-triphosphate
BMRB	Biological Magnetic Resonance Data Bank
CPMG	Carr-Purcell-Meiboom-Gill
CSA	chemical shift anisotropy
CSP	chemical shift perturbation
EOM	ensemble optimization method
GK	guanylate kinase domain
HSQC	heteronuclear single quantum coherence
MAGUK	membrane-associated guanylate kinase
MD	molecular dynamics
μs-ms	microsecond to millisecond
MTSL	<i>S</i> -(2,2,5,5-tetramethyl-2,5-dihydro-1H-pyrrol-3-yl)methyl methanesulfonylthioate
NMR	nuclear magnetic resonance
NOE	nuclear Overhauser effect
PDB	Protein Data Bank
PDF	pair distribution function
PDZ	PSD95/Discs large/ZO-1

PDZ2	the second PDZ domain from PTP BL
PDZ3	the third PDZ domain from PSD-95
PRE	paramagnetic relaxation enhancement
PS	PDZ3-SH3
PSD-95	postsynaptic density protein 95
PSG	PDZ3-SH3-GK
ps-ns	picosecond to nanosecond
PTP-1E	protein tyrosine phosphatase 1E
R_1	spin-lattice (longitudinal) relaxation rate
R_2	spin-spin (transverse) relaxation rate
R_2^0	intrinsic R_2
R_2^{eff}	effective R_2
RA-GEF2	ras guanine nucleotide exchange factor 2
RDC	residual dipolar coupling
R_{ex}	transverse relaxation rate due to chemical exchange
R_g	radius of gyration
S^2	order parameter
S^2_{axis}	order parameter of the methyl symmetry axis
SAXS	small angle X-ray scattering
SB	Solomon-Bloembergen
SEA-HSQC	solvent exposed amides HSQC
SG	SH3-GK
SH3	src homology 3 domain

τ_c	total correlation time
τ_e	effective internal correlation time
τ_m	rotational correlation time
τ_s	electron relaxation time

Chapter 1

Introduction

Proteins are involved in nearly all biological processes. Studying protein function therefore lays the basis for understanding biological phenomena. Traditionally, protein structure is deemed to be most important in deciphering protein function at the atomic level. Indeed, the last several decades have witnessed an intense focus on protein structure, as demonstrated by over 70,000 deposited protein structures in Protein Data Bank; The last several decades have also witnessed dramatic progress in and great benefit from studies on protein structure: by studying protein structure, we understand how proteins function as enzymes, how proteins interact to transduce signals, how proteins are regulated in aspects of the synthesis, function and destination, and how novel proteins can be designed to possess functions of our interests.

Despite being insightful and powerful, studying protein structure does not provide a complete understanding of protein function. For example, it has been found that many eukaryotic proteins exist and function as intrinsically disordered proteins (IDPs). These proteins lack well defined structures, or are only transiently structured. The existence of IDPs can only be explained by inter-converting ensembles [1-3]. Actually, even for a protein with stable structure, its function cannot be fully recapitulated by its static protein structure alone. Another important property encoded in the primary sequence is protein dynamics. The dynamics here is referred to as the coordinate changes of protein atoms at

various time scales ranging from picoseconds (ps) to seconds. In essence, nearly all biological processes are ever exchanging, which requires proteins to possess dynamic properties. Numerous studies have proven that protein dynamics plays important roles in enzyme catalysis[1], ligand binding [2, 3], and allosteric transferring and regulation [4].

This thesis aims to understand interdomain allostery of postsynapse density protein 95 (PSD-95) from structural and dynamic aspects. PSD-95 consists of three PDZ domains, an SH3 domain and a non-catalytic GK domain. Recent studies have shown that interdomain communication is present in PSD-95. Especially, the PDZ domains of PSD-95 possess active roles more than scaffolds, as suggested by allosteric interaction of the PDZ domains with other domain components. Because of central importance of the PDZ domains for this project, the general features of PDZ domains will be introduced in the following section.

1.1 Introduction to PDZ domains

PDZ domains are named after the postsynaptic density protein-95 (PSD-95), *Drosophila* Discs large tumor suppressor, and zonula occludens-1 protein (Zo-1), which were the first three proteins found to share the domain. Following studies suggested that PDZ domains are ubiquitously found in bacteria, yeast, plants, viruses and animals [5]. In human beings, over 200 PDZ containing proteins have been identified [6, 7], most of which are signaling proteins. Usually PDZ domains occur with other protein interacting domains, such as SH3 and L27 [8].



Figure 1.1: The representative structure of PDZ domains. The binding groove formed by $\alpha 2$ and $\beta 2$ are denoted. The binding peptide (-QTSV) is shown in green sticks. The H-bonds between the PDZ domain and the peptide are shown in green dotted lines. The third α -helix, which is usually not deemed as a canonical element of PDZ domain, is shown in gray. The graphic was prepared based on the crystal structure of PSD-95 PDZ3 (PDB ID 1BE9) using PyMol.

The first solved crystal structure of a PDZ domain is the third PDZ domain (PDZ3) of PSD-95 by Doyle et al.[9]. As shown in Fig. 1.1, PDZ3 is folded into a compact globular structure, consisting of six β strands and two α -helices. $\beta 2$ and $\alpha 2$ form a peptide binding groove. With more PDZ domains identified and more homologue structures solved, the PDZ fold paradigm established by PSD-95 PDZ3 was confirmed again and again, though the homology of primary amino acid sequence of PDZ domain can be as low as 20 %.

PDZ domains are protein interacting modules. The basic function of a PDZ domain is to cluster various signaling proteins to facilitate protein interaction among target proteins. This may explain why PDZ domains occur multiple times in the same protein or along with other protein interacting modules. PDZ domains fulfill their recruitment role through binding the C-termini of target proteins. The recognition sequence contains approximately 4-7 amino acids. According to the sequence consensus of PDZ binding peptides, PDZ domains, as well as PDZ binding peptides, are cataloged into three classes: $-(S/T) X\Phi$ (Class I), $-(\Phi/\Psi) X\Phi$ (Class II) and $-G (E/D) XV$ (Class III), where X corresponds to any amino acid, Φ to hydrophobic residues and Ψ to aromatic residues[10]. The hydrophobic sidechain of the very C-terminal residues is docked into a hydrophobic patch of the PDZ binding groove. The carboxyl terminal is required for most PDZ peptide interactions, because the carboxyl group forms H-bonds with PDZ domain. There are exceptions to this. For example, syntrophin PDZ domain can also bind to internal fragments of target proteins [11]. A more systematic study suggested that PDZ domains are able to bind internal peptides, provided that the internal peptides can adopt into correct conformations for recognition [12].

The specific function of a PDZ domain can only be fully understood in the context of the full length PDZ bearing protein, despite the fact that an isolated PDZ domain and its target peptides may be well characterized. That means the particular function of a PDZ domain also depends on other domains present in the same protein. In reality, rarely does a PDZ domain alone constitute a single domain protein. Instead, PDZ domains are integrated into protein multiple times, or with other domains[13]. The domains other than PDZ may determine the location of the PDZ containing protein, the

components of signal complex or pathways involved. This is a straightforward reason why PDZ function is context dependent.

Ten years after the first reported structure of PDZ domains, these domains are found to interplay with other domains, more than just passive scaffolding. This interdomain allostery has been found in several PDZ containing proteins. The conformation of the PDZ domain from Par 6 changes upon interaction between CRIB and CDC42. CRIB is adjacent to the PDZ domain in Par 6, and forms a domain packing interface, which transfer the interdomain allostery [14]. Interdomain interaction is also exemplified by PDZ4/PDZ5 from GRIP [15], in which PDZ4 and PDZ5 domain are mutually dependent. The presence of one domain is indispensable for the correct folding and stability of the other domain. These cases of interdomain allostery pose a challenge to the traditional consideration of PDZ domain as simple modular binding domain.

1.2 PSD-95

Postsynaptic density protein 95 (PSD-95) is one of the most abundant proteins in postsynapse, which is the key component of neuron signal transduction apparatus [16, 17]. The known functions of PSD-95 established by existing research include postsynapse genesis, stability and strength, ion channel clustering and localization, signal complex organization [7, 16]. The functional mechanism of PSD-95 is still unclear. Malfunction or deficiency of PSD-95 was shown to result in impaired learning and memory [7, 16]. Recent studies suggested that PSD-95 is related to central nervous system diseases, such as Alzheimer's [18, 19] and Huntington's disease [20].

PSD-95 belongs to the protein family of membrane associated guanylate kinases (MAGUKs) [17]. In human beings, besides PSD-95, three other proteins are PSD-93, SAP102 and SAP 97 [17]. MAGUK is characterized by one or several PDZ domains, an SH3 domain and a non-catalytic GK domain, of which the three C-terminal domains, PDZ-SH3-GK is called MAGUK core. PSD-95 consists of five domains, PDZ1-3, SH3 and GK (Fig. 1.2). Isolated domain structures of PSD-95 have been solved by either crystallography or NMR. However, the full length structure of PSD-95 is still unavailable. The only point known about full length PSD-95 is that the five domains assemble into a C-shape molecule [21]. The following is a brief introduction to the five domains of PSD-95.

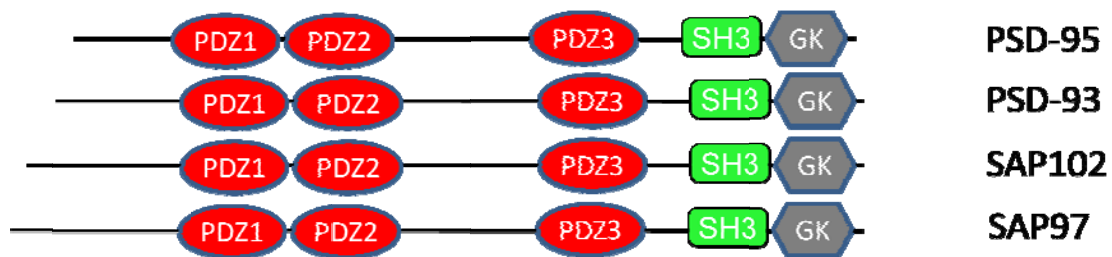


Figure 1.2: Domain architecture of PSD-95 like proteins.

N-terminus: The very N-terminal 60 amino acids of PSD-95 is a flexible loop based on secondary structure prediction, which is also confirmed by the study on PDZ1/PDZ2 [22]. Nevertheless, the first 13 residues are involved in PSD-95 multimerization, of which Cys3 and Cys5 are essential for multimerization [23, 24]. Multimerization of PSD-95 is critical for potassium channel Kv1.4 clustering. Cys3 and Cys5 are also palmitoylation sites for acyl transferases, such as P-PAT [25, 26].

Palmitoylation of PSD-95 is necessary for PSD-95 clustering and neurotransmission mediated by AMPA receptor.

PDZ1/PDZ2: PDZ1 and PDZ2 are connected by a short linker of 5-6 amino acids. The tandem PDZ1/PDZ2 structure has been solved by NMR and crystallography (Fig. 1.3) [22, 27]. A recent study by Wang et al. reveals that PDZ1 and PDZ2 forms an interdomain interface [27], and the orientation of the two domains is not random. The two domains are oriented in such a way that the binding grooves of PDZ1/PDZ2 are aligned, which makes peptide binding of two domains synergistic. Using residual dipolar coupling and MD simulation, Wang et al. showed that cypin peptide binding of PDZ1/PDZ2 increased domain flexibility[22]. These results suggest PDZ1 and PDZ2 function as an intact functional moiety.

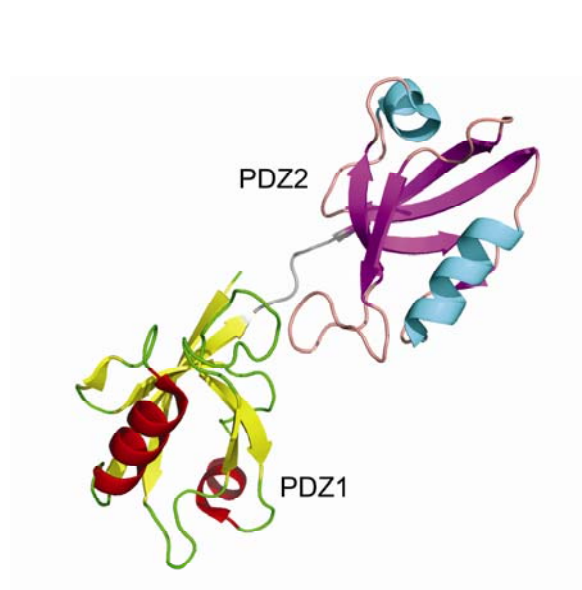


Figure 1.3: The crystal structure of the PDZ1/PDZ2 tandem.

PDZ3: PDZ3 is separated from PDZ1/PDZ2 by a 50 residue linker. PDZ3 is the first structurally solved PDZ domain [9]. It mainly binds to Class I targets, such as APC, NR2B, neuroligin, CRIPT, stargazin and Kv1.4 [28]. According to crystal structures of PDZ3 in apo and peptide bound forms, PDZ3 does not experience conformational changes[9]. The absence of conformational changes upon peptide binding tends to impose onto PDZ3 a passive profile typical of scaffolding proteins. PDZ3 in the context of full length PSD-95, however, seems to possess more “active” roles, which will be discussed later. Although PDZ3 from PSD-95 is deemed a structure paradigm for the PDZ family, it is quite atypical due to the presence of a third α helix ($\alpha 3$) (Fig. 1.1). It seems it is the third α helix that endows PDZ3 with interdomain allosteric roles. The $\alpha 3$ region is highly conserved throughout the MAGUK family. Deletion or replacement of $\alpha 3$ with random coil sequence in Dlg1 (a homology of PSD-95) removes the aforementioned interdomain allosteric behavior between SH3 and PDZ3[29]. This linker region between PDZ3 and SH3 is likely also a hot spot for regulation. Three phosphorylation sites have been identified, Y397[30], Ser415 and Ser418[31, 32]. Sequence alignment suggests these phosphorylation sites are quite conserved.

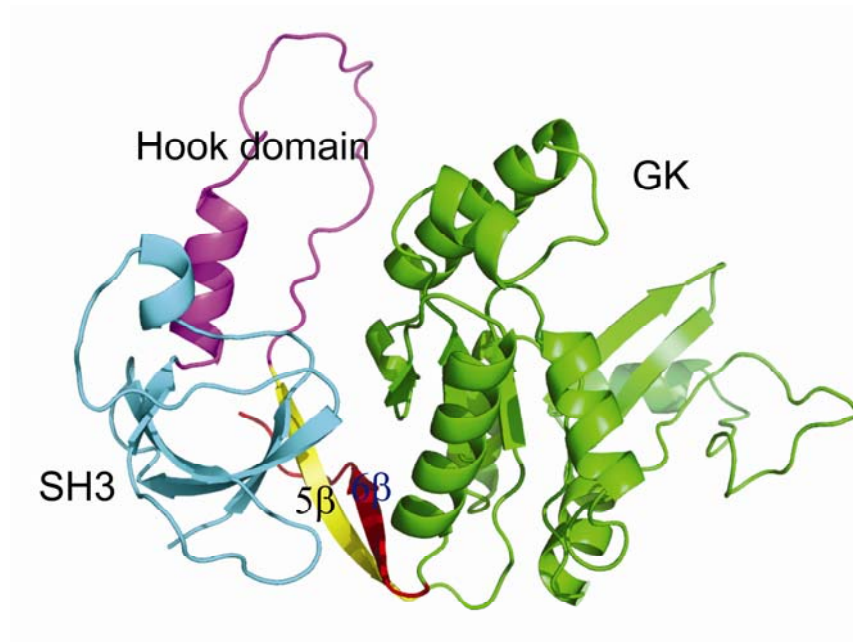


Figure 1.4: The crystal structure of the SH3-GK tandem. The SH3 domain is shown in cyan, the Hook domain in magentas, and the GK domain in green. The fifth and sixth β -stands are denoted and shown in yellow and red respectively.

SH3/GK: Canonically, SH3 is a protein interacting domain which recognizes a PXXP motif [33, 34]. The sidechains of prolines fit into hydrophobic groove of the SH3 domain. The SH3 domain of PSD-95 is modified by an insertion α -helix and flexible loop, which is called the Hook domain (Fig. 1.4)[35, 36]. The α -helix portion of the Hook domain is conserved throughout PSD-95, while the flexible loop shares low homology. Insertion of Hook domain partially occludes the PXXP binding groove. However, it was reported that the microtubule end-binding protein, EB3, directly interacts with SH3 using a proline-rich motif [37]. Several studies also suggest that the Hook domain, which is rich in positively charged residues, binds to calmodulin in a negatively charged groove [38, 39].

The SH3 domain in PSD95 is structurally dependent on the GK domain. Different from canonical SH3 domains which have 5 β -strands, SH3 in PSD-95 has 6 β -strands. The GK is inserted between the 5th and 6th β -strands, and forms a hydrophobic contact with the SH3 domain (Fig. 1.4). The GK domain of PSD-95 has 40% sequence homology to yeast guanylate kinase. Structurally, GK in PSD-95 resembles the open form of yeast guanylate kinase. However, unlike other guanylate kinases, the GK in PSD-95 has no catalytic activity to convert GMP to GDP. Instead, GK evolved into a protein binding domain. Currently identified GK binding targets include AKAP79/150[40], MAP1A [28], GAKIN[41] and GKAP[42]. The interaction of GK with MAP1A and GKAP was thoroughly studied by Reese et al [43]. This study identified key residues for MAP1A binding in GK, and suggested that the guanylate binding site of GK served as binding groove of MAP1A ([43]). During the binding process, GK domain experiences a transition from open to close conformation, while MAP1A assumes an extended conformation.

1.3 Interdomain allostery and regulation of PSD-95

All subdomains of PSD-95 have been studied at a structural level, though only after being excised from the reminder of PSD-95. However, emerging observations suggest the presence of interdomain communication within PSD-95 (and with MAGUK members). The first case is the interdomain allostery between PDZ3 and GK of PSD-95. It was found that binding of CRIPT to PDZ3 promotes the interaction of GK with its binder, MAP1A[28]. This type of domain communication also applies to other PSD-95 homologues, such as PSD-93, SAP97 and SAP102[28]. Interdomain allostery is also

exemplified by the PSD-95 homologue in drosophila, Dlg1, in which PDZ3 is indispensable for interaction between SH3 and Gukholder; while, the interaction between SH3 and Gukholder is abolished by the presence of PDZ3 binding peptides, such as APC and neuroligin[29]. Interdomain allostery is also found between PDZ3 and SH3. Many studies have shown that calmodulin binds to the Hook domain of SH3, and interestingly, the interaction between the Hook domain and calmodulin is enhanced by the presence of PDZ binding peptide, such as CRIPT[38]. As mentioned previously, SH3 and GK are structurally interdependent in MAGUK family proteins. Indeed, the interdomain allostery between SH3 and GK is evident from mutations at the Hook domain and Hook hinge of Dlg1, which constitutively activate the GK domain[44].

The allosteric behavior of PSD-95 suggests that PSD-95 is not only a scaffolding to concentrate signaling molecules to facilitate complex formation, but also a regulatory organizer to ensure the proper binders are targeted at the correct spatial and time order. In consideration of the numerous binders targeted and various biological functions involved by PSD-95, it is not surprising that PSD-95 is under tight regulation, such as palmitoylation and phosphorylation. Palmitoylation is mainly happening at the N-terminus of PSD-95, while phosphorylation is throughout the primary sequence. Many phosphorylation sites have been identified in PSD-95, most of which are located at domain boundaries. The function of phosphorylation is poorly documented, and not studied at a structural level yet. Phosphorylation of PSD-95 may interplay with interdomain allostery to fine tune PSD-95 functions. In the PSD-95 homologue, SAP97, phosphorylation of the N-terminal PDZ1 and the linker of PDZ2/PDZ3 by p38 γ prevents binding of GK to GKAP[45]. The structural and functional coupling of these five

domains in PSD-95, and the regulation of PSD-95 by dimerization and phosphorylation cannot be fully understood by the “divide and conquer strategy” which has mainly been used in structural studies on PSD-95. Since all five domains have solved structures, it is an opportune time to assemble them together to understand the interdomain allostery within PSD-95.

Understanding the interdomain allostery within PSD-95 is the main goal of this thesis. As a summary, all reported interdomain allostery and phosphorylation sites of PSD-95 are tabulated in Table 1.1 and Table 1.2.

Table 1.1: Interdomain allostery with in PSD-95 family

MAGUK protein	Effector Domain	Effector Event	Responsor Domain	Responding Event
SAP-97	PDZ3	CRIPT binding	Hook	Increase binding with calmodulin
SAP-97	PDZ2/PDZ3 linker	Phosphorylation	GK	Disrupt binding with GKAP
PSD-95	PDZ3	CRIPT binding	GK	Increase binding with MAP1A
Dlg1	SH3-Hook	Mutation	GK	Increase binding with Gukholder
Dlg1	PDZ3	CRIPT binding	GK	Disrupt binding With Gukholder

Table 1.2: Phosphorylation sites in PSD-95

Residue	Location
T19	N-terminus[46]
S25	N-terminus[46]
S73	PDZ1[47]
S142	PDZ1[32]
Y240	PDZ2[31, 32, 48]
T287	PDZ2/PDZ3 linker[49]
S290	PDZ2/PDZ3 linker[45]
S295	PDZ2/PDZ3 linker[32]
Y397	PDZ3[30]
S415	PDZ3/SH3 linker[48]
S418	PDZ3/SH3 linker[32, 48]
Y432	SH3[48]
Y533	SH3/GK boundary[50]

1.4 hPTP1E PDZ2

Protein tyrosine phosphatase BL (PTP BL) is a cytosolic non-receptor type phosphatase. This phosphatase is found to be involved in regulation of cell apoptosis, cytokinesis, cell surface expression of Fas, and suppression of ephrinB phosphorylation[51]. Full length PTP BL has 2490 amino acids. From the N-terminus, PTP BL consists of a KIND domain, a FERM domain, five PDZ domains (named as PDZ1-5) and a phosphatase catalytic domain. Of the five PDZ domains, the second PDZ domain (PDZ2) is thoroughly studied. PDZ2 binds to Class I (APC) and Class III peptides (RIL).

1.5 Overview of this work

The ultimate goal of this work is to understand how interdomain communication of PSD-95 is carried out and how phosphorylation regulates PSD-95 function. The motivation for this project is actually stem from studying the phosphorylation of PDZ3 as described in Chapter 2.

In Chapter 2, we studied the phosphorylation of PDZ3 at Y397, which is located at the third α -helix. Upon phosphorylation of Y397, as shown in our research, the third α -helix becomes undocked from the main part of PDZ3 and exists as an unfolded coil. We further showed that this phosphorylation weakens the domain packing between PDZ3 and SH3.

These results presented in Chapter 2 hint that interaction between SH3/GK may provide the structural basis by which interdomain allostery of PSD-95 can be carried out. Therefore in research described in Chapter 3, we made an effort to build a structural model of MAGUK core, PDZ3-SH3-GK. To build this model, we employed NMR paramagnetic relaxation enhancement (PRE) to provide long distance constraints and small angle X-ray scattering (SAXS) to probe the envelope of PDZ3-SH3-GK. The MAGUK core structure sheds light on how interdomain communication may be carried out. The MAGUK core structural model enables us to obtain full length PSD-95 structure with SAXS data. A structural mechanism for interdomain allostery of PDZ3/SH3 and PDZ3/GK are proposed, and function of the Hook domain is discussed.

In Chapter 4, we studied intramolecular allosteric-like behavior of hPTP BL PDZ2 using both NMR and crystallography. Our research settles a nagging ambiguity in PDZ2 studies: whether PDZ2 experience structural changes upon peptide binding. Our research suggested that peptide binding does not incur significant structural perturbation on PDZ2, whereas perturbations on fast time scale dynamics are radiated to distal sites from the peptide binding groove.

1.6 NMR relaxation and protein dynamics

Proteins can be thought of as dynamic machinery, which possesses motions on time scales from ps to seconds. Dynamics at different time scales is related to different motional modes, and to different biological functions (Fig. 1.5). Dynamic information of proteins can be studied by several experimental methods, such as fluorescence and infrared spectrum[52, 53]. However, atom specific information of a molecule cannot be

obtained by these two methods. X-ray crystallography B-factors provide site specific dynamic information, but interpretation of B-factors is highly skewed by the crystal packing. Besides, B-factors from flexible loop regions are unreliable due to poor electron density.

NMR is the most powerful tool by which to study protein dynamics. NMR provides a repertoire to probe dynamics on time scales from ps-s (Fig. 1.5). Two timescales relevant to this thesis are ps-ns, and μ s-s timescale dynamics, which are briefly introduced below.

NMR relaxation is the process by which nuclear spins return to thermal equilibrium state from an excited state created by a pulse or pulses of electromagnetic radiation [54]. For the nuclei of bio-molecular interest, such as ^{13}C and ^{15}N , the two most important relaxation mechanisms are dipole-dipole interactions and chemical shift anisotropy (CSA) [54, 55]. Both relaxation mechanisms are directly related to rotational and internal motions of proteins. It is the direct relationship of protein motions to relaxation that makes NMR capable of quantifying protein dynamics.

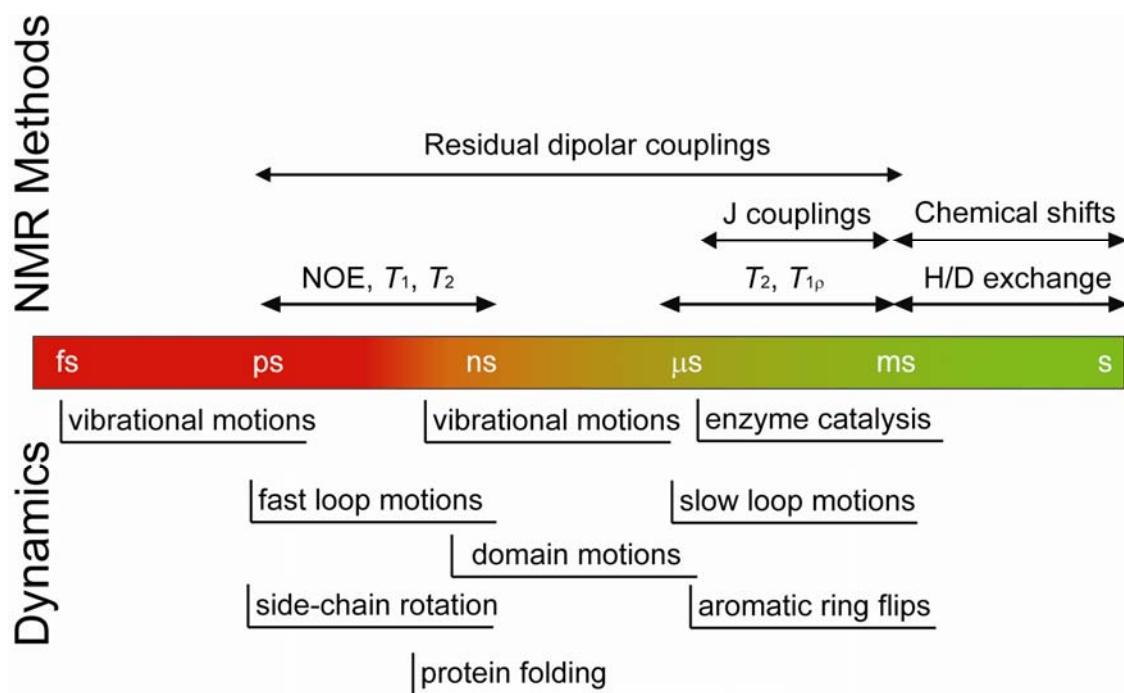


Figure 1.5: Timescales of protein dynamics and appropriate NMR methods.

In the presence of an external static magnetic field, NMR active nuclei of a molecule can be visualized as small magnetic dipoles. Besides experiencing the external field, nuclei also sense the presence of “tiny” local fields created by surrounding nuclei. The strength of the external field is constant, but the local fields created by nuclear dipoles are orientation dependent. As shown in Fig. 1.6, nucleus A senses a different strength and direction of the local field created by nucleus B, depending on the relative orientation of A and B. For a protein undergoing rotational and internal motions, the relative orientation of a pair of nuclei pairs also changes accordingly. Therefore fluctuating local fields are created by protein motions. The fluctuating local field facilitates the energy transfer between the nuclei of protein to the surrounding medium (spin lattice relaxation, longitudinal relaxation, R_1) and the dephasing or loss of coherence of spin (spin spin relaxation, transverse relaxation, R_2).

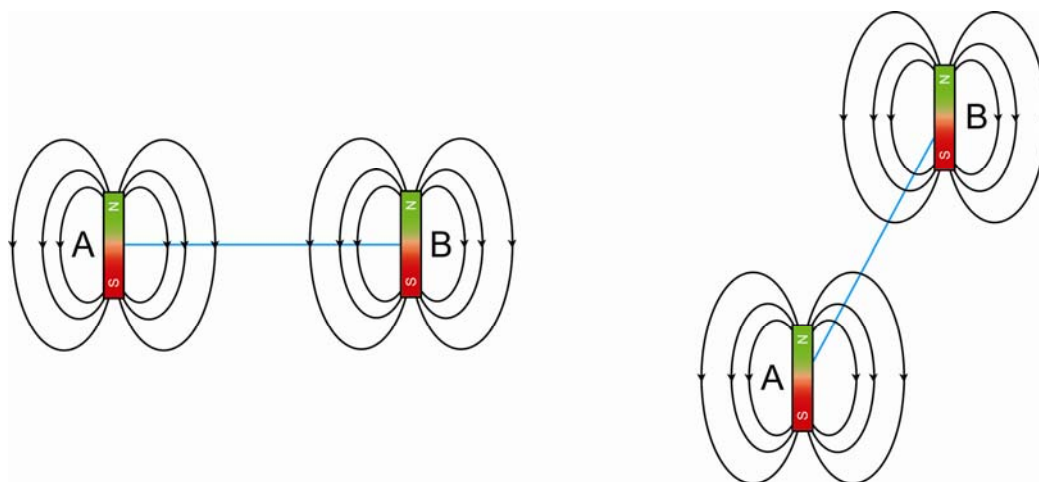


Figure 1.6: Dipole-dipole interaction and vector orientation. The magnetic moments of nucleus A and B, connected by covalent bond (cyan), are visualized as magnetic bars. The orientation of two nuclei affects the dipole-dipole interaction.

CSA arises from the variation in shielding from the external field. When a chemical bond in a tumbling molecule is changing its orientation relative to the static external field (the anisotropy of the chemical shift tensor), the extent to which the external field is shielded by the electron cloud varies. This variation in external field shielding produces variation in effective magnetic field experienced by nuclei. Therefore, similar to dipole-dipole interaction, a relaxation mechanism is formed.

1.6.1 ps-ns timescale dynamics

The mathematic relationship between protein motions and NMR relaxation is connected by the spectral density function, $J(\omega)$. The energy levels of an NMR active spin are quantized. Only the portion of motions at appropriate frequencies can stimulate spin energy transitions. This means that only a proper tumbling rate or frequency contributes to NMR relaxation. However, due to the stochastic nature of molecular motions, the frequency of protein motion cannot be described by one or several distinct

frequencies. A continuous function, the spectral density function $J(\omega)$, describes the likelihood of a motion at certain frequency. Experimentally, it is not feasible to map the whole spectral density function. Only several frequencies related to the nuclear spin resonance can be measured. The relationship between experimental R_1 , R_2 and spectral density function and the heteronuclear NOE[56] are given by the following equations[55]:

$$R_1 = R_1^{DD} + R_1^{CSA}$$

$$R_1^{DD} = \frac{1}{4}d^2[J(\omega_H - \omega_N) + 3J(\omega_N) + 6J(\omega_H + \omega_N)]$$

$$R_1^{CSA} = c^2 J(\omega_N)$$

$$R_2 = R_2^{DD} + R_2^{CSA} + R_{ex}$$

$$R_2^{DD} = \frac{1}{8}d^2[4J(0) + J(\omega_H - \omega_N) + 3J(\omega_N) + 6J(\omega_H) + 6J(\omega_H + \omega_N)]$$

$$R_2^{CSA} = \frac{1}{6}c^2[4J(0) + 3J(\omega_N)]$$

$$NOE = 1 + \frac{1}{4R_1}d^2(\gamma_H / \gamma_N)[6J(\omega_H + \omega_N) - J(\omega_H - \omega_N)]$$

$$d = \left(\frac{\mu_0 h \gamma_N \gamma_H}{8\pi^2} \right) \left(\frac{1}{r_{NH}^3} \right)$$

$$c = \frac{\omega_N \Delta\sigma}{\sqrt{3}}$$

in which, “DD” and “CSA” denote dipole-dipole and chemical shift anisotropy relaxation mechanisms, as mentioned; R_{ex} is the relaxation mechanism contributed by chemical exchange, which will be talked in the next section. γ is the gyromagnetic ratio of ^{15}N and ^1H , r is the length of N-H bond, $\Delta\sigma$ is the breadth of the CSA tensor, μ_0 is the permeability of free

space, and h is the Planck's constant. The spectral density function in above equations does not distinguish the rotational motion from protein internal motions, which are more relevant to protein functions. Lipari and Szabo, proposed a model to separate the protein rotational motions from protein internal motions[57, 58]. This model assumes that the internal motion of protein is much faster than protein tumbling and there is no correlation between the two. This model doesn't assume any specific geometry for protein internal motions. Therefore it is also known as "the model free" formalism. The spectral density function taking protein internal motion into consideration is shown as[55]:

$$J(\omega) = \frac{2}{5} \left(\frac{S^2 \tau_m}{1 + (\omega \tau_m)^2} + \frac{(1 - S^2) \tau_e}{1 + (\omega \tau_e)^2} \right)$$

$$\tau^{-1} = \tau_m^{-1} + \tau_e^{-1}$$

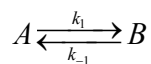
in which, τ_m is the protein tumbling correlation time and τ_e is the internal effective correlation time, S^2 is the order parameter for NH bond. Parameter τ_e describes the timescale of the internal motion, and S^2 describes the amplitude of the internal motions. The value of S^2 ranges from 0 to 1, indicating completely random internal motion of chemical bonds and completely rigid motions with respect to molecular frame. Therefore S^2 is closely related to the rigidity or secondary structure of a residue. Usually, residues involved in secondary structures possess higher S^2 , while the random coil or terminal residues without packing tend to have low S^2 . In this sense, backbone order parameters are not typically informative, since they are highly correlated with protein secondary structures.

On the contrary, order parameters of methyl bearing side chains (S_{axis}^2) of a protein vary from site to site. Measurement of methyl dynamics is based on quadrupole relaxation of deuterium in CH_2D methyl isotopomers [59]. Many studies have shown that S_{axis}^2 is directly

related to protein conformational entropy, and can be used to calculate protein conformation entropy [60-62]. Our studies on PDZ2 suggest S^2_{axis} is sensitive to ligand binding. The perturbation of S^2_{axis} resulting from peptide binding is propagated to sites distant from the binding groove [2, 3]. These results revealed for the first time the allosteric-like behavior of PDZ domain. Using dynamic information from S^2_{axis} , our recent study on the third PDZ domain from PSD-95 shows truncation of the third α -helix greatly prompts protein dynamics, and decreases peptide binding affinity by 20 fold[63].

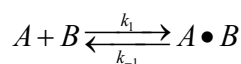
1.6.2 CPMG relaxation dispersion

Most biological processes, such as enzyme catalysis, protein folding, ligand binding and allosteric regulation, tend to occur on μs -ms timescale. Studying protein dynamics of μs -ms motions is of fundamental importance in understanding mechanisms of these biological processes. Fortunately these processes always incur chemical environment changes of nuclei. For example, ligand binding perturbs chemical shifts of surrounding binding groove; substrate binding and catalysis changes chemical shifts of enzyme active sites; conformational changes alters local protein structure and consequently environment of nuclei. Generally speaking, a process in which a spin experiences two or multiple chemical environments, and consequently two or more chemical shifts is referred to as chemical exchange[64]. The definition of exchange rate depends on the exchanging system: for a two-state exchanging system,



$$k_{\text{ex}} = k_1 + k_{-1}$$

For biomolecular association,



$$k_{\text{ex}} = k_1[B] + k_{-1}$$

in which, k_{ex} is the chemical exchange rate, and k_1 , k_{-1} are forward and reverse rates respectively.

Chemical exchange has profound effects on the appearance of NMR spectra according to the NMR chemical shift timescale (Fig. 1.7). Depending on the relative values of the exchange rate (k_{ex}) and the chemical shift difference ($\Delta\omega$), the exchange process is classified into three regimes: slow exchange ($k_{\text{ex}} \ll \Delta\omega$), intermediate ($k_{\text{ex}} \approx \Delta\omega$) and fast exchange ($k_{\text{ex}} \gg \Delta\omega$). In the slow exchange scenario, two distinct resonances are observed. With increasing of k_{ex} , two sets of peaks gradually become coalesced and broadened (intermediate exchange), and finally merge into a single sharp peak (fast exchange) whose chemical shift is the population weighted average of the two exchanging states.

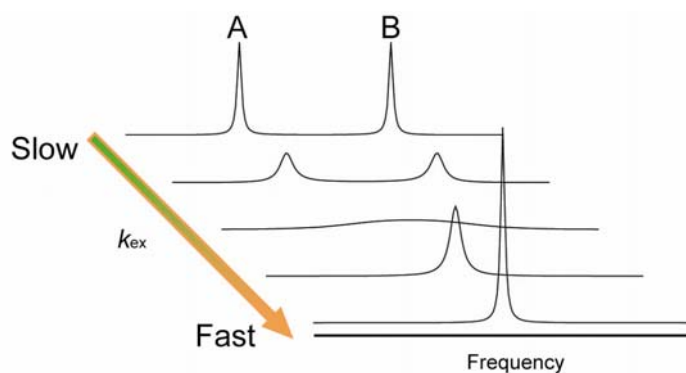


Figure 1.7: Impact of exchange rate on NMR lineshape.

Chemical exchange makes an extra contribution to spin relaxation besides intrinsic relaxation R_2^0 , making possible the analysis of chemical exchange using NMR. The analysis of chemical exchange depends on the so-called CPMG (Carr-Purcell-Meiboom-Gill) pulse train, which occupies a constant time block T , but contains varying numbers of 180° refocus pulses $(-\tau_{cp}-180^\circ-\tau_{cp}-)$ [65]. The interval between neighboring 180° pulses is called τ_{cp} , which can be varied from several μ s to 10 ms. The basic idea for how CPMG works is that when an exchanging process is comparable to the length of τ_{cp} , the relaxation due to chemical exchange cannot be refocused by the CPMG train. The effective or experimental relaxation rate R_2^{eff} depends on the density of 180° refocus pulses. By varying the number/frequency of 180° refocus pulses, the magnitudes of R_2^{eff} varies, and this dependence is known as relaxation dispersion. Experimentally, R_2^{eff} measured at specific τ_{cp} intervals is calculated using the following equation[66]:

$$R_2^{\text{eff}} = -\frac{1}{T} \ln\left(\frac{I}{I_0}\right)$$

where I and I_0 are the intensities with and without CPMG pulse train, T is the constant time block. By collecting R_2^{eff} at different τ_{cp} delays, a curve of R_2^{eff} versus τ_{cp} can be obtained.

The dependence of R_2^{eff} on τ_{cp} can be fitted by the Carver-Richards equation for two-state exchange[67]:

$$R_2(1/\tau_{cp}) = \frac{1}{2} \{R_{2a}^0 + R_{2b}^0 + k_{ex} + \frac{1}{\tau_{cp}} \cosh^{-1}[D_+ \cosh(\eta_+) - D_- \cosh(\eta_-)]\},$$

where,

$$D_{\pm} = \frac{1}{2} \left[\pm 1 + \frac{\Psi + 2\Delta\omega^2}{(\Psi^2 + \zeta^2)^{0.5}} \right]$$

$$\eta_{\pm} = \frac{\tau_{cp}}{\sqrt{2}} [\pm \Psi + (\Psi^2 + \zeta^2)^{0.5}]^{0.5}$$

$$\Psi = (R_{2a}^0 - R_{2b}^0 - p_a k_{ex} + p_b k_{ex})^2 - \Delta\omega^2 + 4p_a p_b k_{ex}^2$$

$$\zeta = 2\Delta\omega(R_{2a}^0 - R_{2b}^0 - p_a k_{ex} + p_b k_{ex})$$

in which, R_{2a} and R_{2b} are intrinsic relaxation rates of state A and B, p_a and p_b are the populations of state A and B, satisfying $p_a + p_b = 1$, and $\Delta\omega$ is the chemical shift difference between state A and B.

Relaxation dispersion contains kinetic and thermodynamic information. In combination of exchange rate k_{ex} and dissociation constant, forward rate and reverse rate constant can be further deduced. State populations (p_a and p_b) derived from relaxation dispersion curves provide the energy relationship of two states. It is noteworthy that CPMG relaxation dispersion enables detection of lowly populated state, i.e., excited state (<5%). Although relaxation dispersion only provides the magnitude of the chemical shift difference of two states, the sign of $\Delta\omega$ can be retrieved from HSQC/HMQC experiments[68]. With both magnitude and the sign of $\Delta\omega$, the chemical shift of the excited state can be obtained. Obtaining this kind of information can yield new insight into protein structural state. Using relaxation dispersion, Korzhnev deduced chemical shift and residual dipolar couplings of unfolding intermediate states of FF domain, and simulated the structure of intermediate state, which is unavailable for other methods[69].

1.6.3 Application of PRE to protein structure and dynamics studies

One of goals of this thesis is to build a structure model of MAGUK core, which consists of PDZ3, SH3 and GK domain. The molecule weight of MAGUK core is 47 KD. The size of the protein makes chemical shift assignments difficult. The chemical shifts of isolated PDZ3 was assigned by our lab, but the chemical shift assignments for SH3 and GK domain are unavailable. Without chemical shift assignment, it is impossible to employ NOE to find interdomain distance constraints. Moreover, our study showed MAGUK core is highly dynamic. This domain flexibility also makes obtaining high quality data unpractical. Besides, NOE is only suitable for providing short distance information, which may be not competent for our inter-domain packing situation. To overcome these difficulties, we adapted paramagnetic relaxation enhancement (PRE) to obtain long distance constraints.

Paramagnetism arises from unpaired electrons in an atom[70]. Just as the spinning of a positively charged nucleus creates a magnetic moment parallel to its spin direction (which is fundamental of NMR), spinning of a negatively charged electron generates a magnetic moment anti-parallel to its spin direction. For most elements, the magnetic moments of electrons are not detectable, because paired electrons tend to cancel each other's magnetic moments. Due to the configuration of electron orbitals, some elements have unpaired electrons, which produce strong local magnetic moments. With an external field applied, those local magnetic moments tend to align with the external field. This phenomenon is known as paramagnetism.

Historically, application of PRE was mainly confined to metalloproteins with paramagnetic metal ions, such as Cu^{2+} and Ni^{2+} [71]. Recent developments in the

synthesis of nitroxide chemicals make available paramagnetic labeling for protein molecules. This extends the application of PRE to studies of protein structure. At present, commercially available paramagnetic labeling reagents for proteins mainly consist of nitroxide derivatives and EDTA chelator derivatives (Fig. 1.8)[72]. Both types of chemicals can be conjugated to cysteine sidechains in proteins by formation of a disulfide bond.

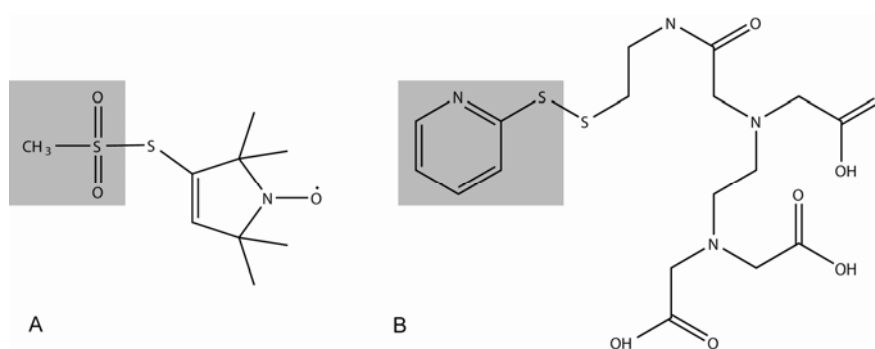


Figure 1.8: Paramagnetic labeling chemicals. (A) MTSL (B) EDTA derived paramagnetic chemicals. The shaded parts are leaving groups, which are not adducted to proteins or DNA.

In a paramagnetic system with anisotropic g-tensor, three observations are available: pseudo-contact shift (PCS), paramagnetic relaxation enhancement and residual dipolar couplings (RDC) (PRE) [73], if the spin labeling center are able to align the sample. Although PCS and RDC of a paramagnetic system contain information of molecular structure and dynamics, mathematic models to analyze these observations are not well developed, and application of PCS and RDC exceeds the scope of this work. We will not further discuss PCSs and RDCs of a paramagnetic system.

For a paramagnetic system with isotropic electron g-tensor, PRE is the only detectable effect. The PRE derives from the dipole-dipole relaxation between unpaired

electrons and the nucleus of interest, and increases rate of spin relaxation. The enhanced longitudinal relaxation rate Γ_1 and transverse relaxation rate Γ_2 are related to molecule structure and dynamics by the Solomon-Bloembergen equations (SB-equations) [74]:

$$\Gamma_1 = \frac{2}{5} \left(\frac{\mu_0}{4\pi} \right)^2 \gamma_I^2 g^2 \mu_B^2 S(S+1) J_{SB}(\omega_I)$$

$$\Gamma_2 = \frac{1}{15} \left(\frac{\mu_0}{4\pi} \right)^2 \gamma_I^2 g^2 \mu_B^2 S(S+1) \{4J_{SB}(0) + 3J_{SB}(\omega_I)\}$$

$$J_{SB}(\omega) = r^{-6} \frac{\tau_c}{1 + (\omega\tau_c)^2}$$

$$\tau_c = (\tau_r^{-1} + \tau_s^{-1})^{-1},$$

in which, γ is the gyromagnetic ratio, $\omega/2\pi$ is the Larmor frequency, r is the distance from paramagnetic center to the nucleus of interest, τ_c is the correlation time, τ_r is the protein rotational correlation time and τ_s is the electron relaxation time. $J(\omega)$ is the spectral density function. Note that S here is the spin quantum number for an electron (not to be confused with the order parameter). In this equation, r provides the distance information which is usually used as a constraint for structure calculation and refinement. Compared with NOE distance constraints, which are shorter than 6 Å, PRE can detect distance up to 25 Å.

Besides providing distance information suitable for structure calculation and refinement, the PRE provides information on protein dynamics [75, 76]. Particularly, the PRE is one of two methods other than relaxation dispersion to probe structural or dynamic information of minor population states. It is relatively straightforward to analyze

PRE data in the fast exchange on the NMR timescale. Consider a system exchanging between state A and B, in which the state A is highly populated, and far from paramagnetic labeling group, while the state B is of low population and near to labeling group. When the exchange rate k_{ex} between the two states is fast enough, i.e.

$k_{ex} \gg \Gamma_{2,B} - \Gamma_{2,A}$, the experimentally observed PRE, Γ_2^{app} can be approximated by following equation[75]:

$$\Gamma_2^{app} \approx p_A \Gamma_{2,A} + p_B \Gamma_{2,B},$$

where p_a and p_b are the percentage populations of states A and B, and $\Gamma_{2,A}$ and $\Gamma_{2,B}$ are the theoretical transverse PREs calculated based on structures of state A and B. Though state B is lowly populated, its vicinity to the labeling group produces strong PRE due to the r^{-6} dependence of the PRE on distance, making information from state B still detectable.

When applying the method, several cautions should be kept in mind. First, as shown by the SB equation, the magnitude of the PRE is proportional to the square of the gyromagnetic ratio. This means in biological molecules, protons are most sensitive to the PRE, while nuclei such as ^{15}N and ^{13}C are not sensitive enough to give accurate PRE values. From our experimental data, the ^1H -PRE, Γ_2 , ranges from 3 to 70 s^{-1} ; while the largest magnitude of ^{15}N is around 4 s^{-1} . Second, Γ_2 is more often used in structure calculation or refinement, because Γ_2 is less susceptible to the internal motion of molecules[77]. Third, due to flexibility of the paramagnetic labeling group, accurate positioning of the paramagnetic center cannot be represented by a single conformation of paramagnetic group[77]. In practice, conformational ensembles of labeling groups are used in calculation of distances between the paramagnetic center and the nucleus of

interest. Also, paramagnetic samples should be freshly prepared to minimize diamagnetic contaminants, which can result from breaking of the disulfide bond[78].

1.6.4 Small Angle X-ray Scattering

Recent years have witnessed a surge in application of small angle X-ray scattering (SAXS) to bio-molecules. Compared with other biophysical methods, SAXS is superior to NMR for proteins with high molecular weight, to crystallography for proteins that are too flexible to obtain crystals, or proteins whose function can only be understood in the context of structural ensemble.

The physical principles and experimental setup of SAXS is the same as those for X-ray crystallography. A 1D scattering curve is obtained between scattering intensity and scatter angle. The different scattering appearance between SAXS and X-ray diffraction derives from the internal order of sample [79]. Unlike crystallography, which is acquired in the crystalline state, SAXS data are collected in the solution state in which molecules rotate and diffuse freely. Structural information given by SAXS therefore is time and orientation averaged. For mathematical simplification, the SAXS scattering curve is usually described by scattering intensity, I and momentum transfer, q :

$$q = \frac{4\pi \sin \theta}{\lambda}$$

where 2θ is the diffraction angle and λ is the wavelength of incident X-ray beam. The scattering intensity $I(q)$ is related to molecule structure by the following equation [80]:

$$I(q) = \left\langle \left| \int (\rho(\vec{r}) - \overline{\rho_s}) e^{i\vec{q} \cdot \vec{r}} d\vec{r} \right|^2 \right\rangle$$

in which $\langle \rangle$ represents the rotational average; $\rho(\vec{r}) - \overline{\rho_s}$ is the scattering density difference between particles and solvent, and will be shown as $\Delta\rho$ thereafter.

Though scattering intensity is correlated with molecular shape, it does not provide structural information in a straightforward way. A more intuitive way to extract particle structure information is given by the pair distribution function $P(r)$, which can be obtained by reverse Fourier transformation of following equation[79]:

$$I(q) = 4\pi \int_0^{D_{\max}} P(r) \frac{\sin(qr)}{qr} dr,$$

where D_{\max} is the maximum distance that can be found in a molecule. The pair distribution $P(r)$ is a counterpart of the Patterson function in crystallography. The pair distribution function basically describes the frequency at which a distance pair can be found in a molecule. The pair distribution function can also be obtained from a protein structure, as[79]:

$$P(r) = r^2 \left\langle \int_V \Delta\rho(r) \Delta\rho(u+r) du \right\rangle,$$

where the integral is carried out over all volume of the molecule. The PDF contains structural information such as radius of gyration, maximum diameter and molecular shape. The PDFs of different molecular shapes have been well exemplified by Svergun[81]. Although for a certain molecular structure, a unique PDF is defined, the reverse is not true. For a given PDF, different structural models can be deduced. For example, PDF cannot distinguish enantiomers.

Usually there are two ways to build a structural model using SAXS. The first is an *ab-initio* method [82, 83]. For *ab-initio* method, the protein chain is simplified as a thread of spherical beads. The string of beads is folded at random to form a compact sphere. The SAXS

curve of the model is calculated and evaluated by comparing with experimental SAXS data. The other way is to build a structural model using rigid body modeling [84, 85], which is particularly powerful for solving structures of multi-domain proteins given individual domain structures. Compared with *ab-initio* methods, rigid body docking overcomes the problem of over-parameterization. Usually models built in this way are more converged. However, due to the dynamic nature of some multiple proteins, a single conformation is not sufficient to yield acceptable fitting of experimental SAXS data. The problem is solved by the ensemble optimization method (EOM) [86]. In this method, a pool of conformations ($> 10,000$ structures) is first generated, and then the best combination of conformations is selected by a genetic algorithm[86].

To obtain usable scattering data, several requirements on protein samples should be met and procedural cautions should be taken. First, SAXS requires sample monodispersity. The most deleterious and often encountered problem is protein aggregation or oligomerization. A seriously aggregated sample can be immediately distinguished by the so-called Guinier plot, i.e. $\log I$ and q^2 . A monodispersed sample yields a linear region up to $R_g q < 1.3$, while an aggregated sample shows a curved region that is tilted up at low q [80]. However, even the Guinier plot is unable to sense subtle aggregation. To probe subtle aggregation, SAXS data at different concentrations are required. For an ideal sample, R_g calculated from different sample concentrations is constant, while slightly aggregated or oligomerized sample have increased R_g with increasing concentration[79]. Therefore, it is routine to prepare SAXS samples of concentrations ranging from 0.5 to 5 mg/ml. Second, SAXS is in essence a contrast method. This requires that the background scattering from solvent has to be subtracted

precisely. To this end, samples must be prepared using either size exclusion chromatography or lengthy dialysis. At the same time, size exclusion column equilibration buffer and dialysate should be used for determining the background scattering which needs to be subtracted off. Third, high intensity of X-ray generates large amount of radicals and could result in radiation damage of protein sample. The radiation damage degrades protein samples or incurs protein aggregation. The radiation damage can be detected by the gradual change in scattering curves. Scavengers, such as DTT or ascorbic acid are useful to reduce radiation damage[87].

Chapter 2

Phosphorylation of a PDZ domain extension modulates binding affinity and interdomain interactions in the PSD-95 MAGUK

2.1 Introduction

Phosphorylation is the most common covalent modification made to proteins in eukaryotes. Depending on the protein substrate, it can regulate the gain or loss of activity through a variety of mechanisms. Most mechanisms studied to date appear to work via a change in steric geometry at the active site or a global conformational change in the protein [88-90], although a few recent examples indicate modulation of protein dynamics that can yield a graded response [91, 92]. Overall, the extent of structural characterization of phosphorylation mechanisms is scarce given the ubiquity of this post-translational signaling mechanism and the large diversity of effects observed upon phosphorylation. A greater understanding of how phosphorylation(s) modulate protein activity is essential to understand signal transduction processes such that they may be manipulated for desired effect.

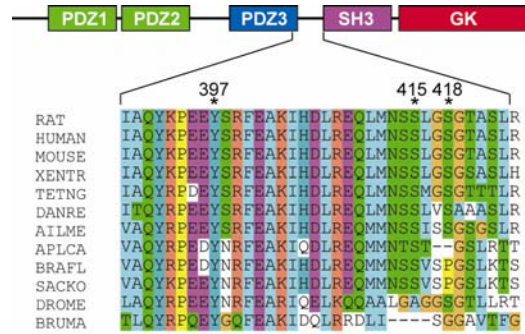


Figure 2.1: Domain architecture of PSD-95. The five domains of PSD-95 are shown, and sequences of $\alpha 3$ region and PDZ3/SH3 linker in MAGUK family from different organisms are aligned. The conserved tyrosine (Y397) and two serine phosphorylation sites (S415 and S418) are denoted by “*”. The alignment was done using ClustalX 2.0.12.

Many phosphorylated proteins are multi-domain, modular proteins [89-91].

MAGUK (membrane-associated guanylate kinase) family proteins are multi-domain scaffolding proteins that play roles in signal transduction and cellular adhesion at cell-cell junctions [93]. The defining MAGUK signature is the PDZ-SH3-guanylate kinase “supradomain” architecture. The best known MAGUK protein is postsynaptic density-95 (PSD-95), which is found on the cytoplasmic side of post-synaptic terminals. PSD-95 is a non-catalytic scaffolding protein that assembles macromolecular complexes for signal integration at excitatory neurons. It consists of three PDZ (PSD-95/Discs large/Zo-1) domains, an SH3 domain, and a non-catalytic guanylate kinase (GK) domain (Figure 2.1). PDZ domains are ~90 residues, globular, protein interaction domains that have a conserved fold comprised of two α -helices and five β -strands. The function of PDZs is typically to bind the C-terminal 4-5 residues of target proteins, which bind in a groove between $\alpha 2$ and $\beta 2$ of the PDZ. PDZ domains are often found in tandem copies and are common to proteins that function as scaffolds for assembling signaling complexes or trafficking components at cell-cell junctions. In PSD-95, its PDZ domains bind many

proteins ranging from NMDA and adrenergic receptors to neuronal nitric oxide synthase (nNOS), Pyk2, SynGAP, and microtubule assemblies [6]. Structural work has been carried out on individual PDZs of PSD-95 [9, 94], as well as the SH3-GK module [35, 36]. However, little is known about how MAGUK PDZ domains associate/function with the SH3-GK module. A role for PDZs beyond their normal C-terminal ligand binding function has emerged from examples in which intermolecular (or interdomain) contacts occur on novel PDZ interfaces [14, 95] or binding is regulated allosterically [14, 63, 96-98].

Previous work suggests that the third PDZ domain (PDZ3) in PSD-95 family proteins regulates activity at SH3-GK, indicating that this PDZ domain may have additional regulatory function on top of its C-terminal binding function. MAP1A binds to the GK domain of PSD-95; however, this interaction is weakened by the presence of PDZ3 (and abolished by the presence of all three PDZ domains) and restored by PDZ binding peptides such as APC, NR2B and CRIPT [28]. Interdomain interactions were also characterized in the *drosophila* homologue of PSD-95, Dlg-1, in which the domain interaction between PDZ3 and SH3 was regulated by PDZ3 binding peptide [29]. The region linking PDZ3 and SH3 is vital to the interdomain communication between these two domains. Replacement of the conserved linker region with flexible Gly-Ser repeats disrupts the influence that PDZ3 has on binding of SH3 to its interaction partner, GukHolder [29]. Thus, a major question regarding MAGUKs is what is the role of the PDZ domain preceding SH3-GK and how might it participate in intramolecular, interdomain interactions?

Interestingly, PSD-95 is known to be phosphorylated at up to a ~dozen sites, with several of these sites being at linker positions in-between structured domains as well as one in a C-terminal helical extension to PDZ3 (Figure 2.1). To date, phosphorylation has received modest attention as a means of regulating PDZ domain function in general. One exception is the PDZ protein NHERF1, for which phosphorylation has been shown to regulate PDZ-mediated autoinhibition[99]. Although studies of phosphorylated PDZ domains are rare, there are numerous instances of phosphorylation of PDZ C-terminal ligands which can either decrease [100-105] or increase [106-108] affinity to their cognate PDZs. Recently, we showed that folding of a C-terminal extension to PDZ3 into an α -helix (α 3) increases binding affinity to PDZ3 ligand via an allosteric mechanism rooted in changes in picoseconds-nanosecond side-chain dynamics [63]. The α 3 helix is not part of the conserved PDZ fold and hence appeared as an unusual auxiliary element whose function had been unclear. Within the α 3 helix, Y397 can be phosphorylated [30], which in principle could either increase or decrease α 3 interactions with the PDZ core. In addition to Y397, the nearby residues S415 and S418 can also be phosphorylated [31, 32]. This dense collection of phosphorylation sites suggests that this region (C-terminal extension of PDZ3 and the PDZ3-SH3 linker) is a hot spot for MAGUK regulation. Interestingly, structured “extensions” to PDZ domains are now being discovered in more PDZ domains [109].

To probe the role of the third PDZ domain (PDZ3) in the PSD-95 MAGUK and its transition into the linker leading into the SH3 domain, we have chosen to study by NMR the effect of phosphorylation at three sites in the C-terminal region of PDZ3 and how such phosphorylations modulate PDZ3 structure, function, and its interaction with SH3-

GK. A construct of PDZ3 spanning residues 304-402 was phosphorylated at Y397 (p³⁹⁷-PDZ3) and characterized for structural effects. A combination of chemical shift analysis, hydrogen exchange, ¹⁵N relaxation, and isothermal titration calorimetry showed that phosphorylation induces a fast equilibrium between a docked conformation in which $\alpha 3$ is packed against the PDZ core and an undocked, flexible state of $\alpha 3$ which has reduced affinity for PDZ3 ligands. We also show that the effect of $\alpha 3$ is not specific to the classic PDZ3 C-terminal ligand from CRIPT, as it influences binding to other C-terminal ligands. In a second construct of PSD-95 spanning PDZ3-linker-SH3, phosphorylation at all three sites (397, 415 and 418) was shown to increase mobility of PDZ3 relative to SH3. These studies provide insight into how phosphorylation affects structure and dynamics of an intrinsically flexible, multidomain system. They also show for the first time that PDZ3's association with the SH3 domain in PSD-95 is weakened by multiple phosphorylations.

2.2 Experimental Procedures

2.2.1 Protein expression and purification

The third PDZ domain (PDZ3, 304-402) and PDZ3-SH3 tandem (304-532) from rat PSD-95 were sub-cloned into pET21a vector with a TEV cleavable N-terminal histidine tag. The PDZ3-SH3 tandem was stabilized by adding the sequence **SGSGSGPYIWVP-AREERL** to its C-terminus, where bold residues are from residues 713-724, which form the F-strand of the SH3 domain. PDZ3-SH3 single mutant (PDZ3-SH3 Y397E) and triple mutant (Y397E/S415E/S418E) were made by multiple-site mutagenesis PCR [110]. Transformed *E. coli* BL21 (DE3) cells were grown at 37 °C in LB medium or minimal medium containing appropriate isotopes. When cell density reached an OD₆₀₀ of 0.6,

IPTG was added to a final concentration of 1 mM and the cells were grown for another 16 hours at 22 °C. The cells were harvested by centrifugation and stored at -80 °C until use.

To purify PDZ3, the cell pellet was re-suspended in 50 mM Tris-HCl, pH 8.0, 200 mM NaCl, 0.1% triton X-100, 25 mM imidazole and 1 mM lysozyme. The re-suspended cells were frozen and thawed for three cycles and applied to sonication. The centrifuged cell lysate was loaded to a nickel affinity column and eluted with 500 mM imidazole. The fractions containing PDZ3 were pooled and subjected to overnight TEV cleavage at 4 °C. A 100% cleavage was achieved as suggested by SDS-PAGE. Cleaved samples were further purified by Source Q ion exchange chromatography, followed by a G50 size exclusion column equilibrated in a buffer containing 22 mM NaPO₄, pH 6.8, 55 mM NaCl and 1.1 mM EDTA. p³⁹⁷-PDZ3 was separated from PDZ3 using a source-Q resin with a 260 ml linear gradient from 0-500 mM NaCl in 20 mM Tris-HCl pH 7.0 (Figure 2.2A). The identity and purity of the protein were verified by mass spectrometry and SDS-PAGE. The protein concentration is determined by UV with an extinction coefficient of $\epsilon_{280}=2980 \text{ cm}^{-1}\text{M}^{-1}$. Phosphorylation changes the UV absorbance profile of tyrosine with an extinction coefficient of $593 \text{ cm}^{-1}\text{M}^{-1}$ at 268 nm [111]. Taking the other unphosphorylated tyrosine (Y392, $\epsilon_{268}=1114 \text{ cm}^{-1}\text{M}^{-1}$) into account, the concentration of p³⁹⁷-PDZ3 was determined using an extinction coefficient of $1707 \text{ cm}^{-1}\text{M}^{-1}$ at 268 nm.

PDZ3-SH3 single and triple mutants were purified using the aforementioned protocol with modification at the size exclusion chromatography step, where elution buffer contained 50 mM Tris-HCl, pH 7.5, 200 mM NaCl and 1 mM DTT.

The plasmid encoding c-Src kinase was a gift from John Kuriyan (UC Berkeley) and Sharon Campbell (University of North Carolina at Chapel Hill). The c-Src kinase domain was purified as described [112].

2.2.2 Peptide synthesis

A 7-mer CRIPT peptide (Ac-NYKQTSV-COOH) was synthesized and purified as reported [63]. The identity and purity of the peptide were verified by mass spectrometry. The peptide concentration is determined using UV with an extinction coefficient of $1490 \text{ cm}^{-1}\text{M}^{-1}$.

2.2.3 Isothermal Titration Calorimetry experiments

ITC experiments were carried out on a MicroCal VP-ITC microcalorimeter and repeated twice to estimate error. PDZ3 and p³⁹⁷-PDZ3 ITC measurements were performed by titrating 1 mM CRIPT peptide into 0.1 mM protein. In total, 280 μl of CRIPT peptide was titrated into 1.4 ml protein solution by 40 steps with a 3-minute interval between injections. The dilution effect was estimated by performing the same titration procedure without protein. Both peptide and proteins were dissolved in the same buffer containing 20 mM NaPO₄, pH 6.8, 50 mM NaCl and 1 mM EDTA. Data were integrated and analyzed using Origin version 5.0 (MicroCal). K_d , ΔH , ΔS and N were fitted with a single binding site model. For PDZ3-CRIPT and p³⁹⁷-PDZ3-CRIPT titrations, c -values were 27.8 and 7.2 respectively.

2.2.4 NMR assignments and relaxation experiments

PDZ3 and p³⁹⁷-PDZ3 NMR samples were dissolved in 20 mM NaPO₄, pH 6.8, 50 mM NaCl, 1 mM EDTA and 10% D₂O at a protein concentration of 1 mM. NMR spectra were acquired on a 500 MHz magnet equipped with a ¹H/¹⁵N/¹³C probe and z-axis pulsed field gradients. Backbone resonance assignments for p³⁹⁷-PDZ3 were obtained using 3D HNCACB and CBCA(CO)NH experiments [113]. Backbone relaxation experiments were carried out as described on a 500 MHz magnet[63]. *T*₂ relaxation data of wild-type PDZ3-SH3, Y397E PDZ3-SH3 and Y397E/S415E/S418E PDZ3-SH3 mutants were acquired on a 500 MHz magnet with cryoprobe at a protein concentration of 0.5 mM. Wild-type and mutant PDZ3-SH3 constructs were dissolved in a buffer containing 50 mM Tris-HCl, pH 7.5, 200 mM NaCl, 10% D₂O and 1 mM DTT. All NMR spectra were processed by NMRPipe and analyzed by NMRViewJ.

2.2.5 SEA-HSQC experiments

Solvent exposed amide-HSQC spectra were collected on a 500 MHz magnet equipped with a ¹H/¹⁵N/¹³C probe and z-axis pulsed field gradients at 298 K. The original SEA-HSQC pulse sequence was developed by Lin et al. using CLEANEX-PM mixing scheme. In this study, a Biopack version of SEA-HSQC pulse sequence was used. The inter-transient delay was to 1.5 seconds, and mixing time 0.1 second. The spectra of PDZ3 and p³⁹⁷-PDZ3 were collected at protein concentration of 1 mM with 16 transients. NMR intensity is a function of several factors such as protein concentration, nuclear relaxation time, solution conductivity and protein tumbling time. Of these factors, protein tumbling time is significantly influenced by phosphorylation (see Results). This necessitates a method to scale the SEA-HSQC intensities of PDZ3 and p³⁹⁷-PDZ3 to allow direct comparison. The scaling procedure used the residues that are not affected by

phosphorylation, i.e., those residues that experience slight or nearly no chemical shift perturbation as shown in Fig. 2.3A. The SEA-HSQC peak intensities of p³⁹⁷-PDZ3 for these residues were scaled to match those of PDZ3.

2.3 Results

2.3.1 Phosphorylation of Y397 and purification of phosphorylated PDZ3

From the crystal structure of PDZ3 [9], the side chain of Y397 is partially buried between $\alpha 3$ and the core domain of PDZ3. This tyrosine residue is phosphorylated in mouse brain, although it is unknown which kinase *in vivo* is responsible for its phosphorylation. Using the Group-based Prediction System [114], Src kinase was predicted to be capable of phosphorylating Y397. After treatment of ¹⁵N-labeled PDZ3 with c-Src, a new set of resonances were observed in the NMR HSQC spectrum of PDZ3. The relative peak intensities suggested that only 10% of PDZ3 was phosphorylated. The reaction went to further completion after removing ADP by dialysis and adding fresh ATP, which was repeated four times. This yielded ~40% p³⁹⁷-PDZ3. Mass spectroscopy further confirmed a single phosphorylation of PDZ3 at Y397.

Ion exchange chromatography was used to purify p³⁹⁷-PDZ3 based on the additional negative charge introduced by phosphorylation. The elution profile displayed five discrete species, three of which tested positive for protein (Figure 2.2A). The first peak was confirmed to be PDZ3 from HSQC, and the third peak as pure phosphoPDZ3. An overlay of HSQC spectra of PDZ3 and putative p³⁹⁷-PDZ3 shows peaks shifting in regions of PDZ3 consistent with modification at Y397 (Figure 2.2B). The identity and purity of the third peak was also confirmed to be phosphorylated PDZ3 at Y397 by mass

spectrometry. We note that the PDZ3 construct used has only one other tyrosine at position 392, thereby increasing the probability that singly phosphorylated PDZ3 can be obtained. The above procedure was used to obtain milligram quantities of p³⁹⁷-PDZ3 for further biophysical characterization.

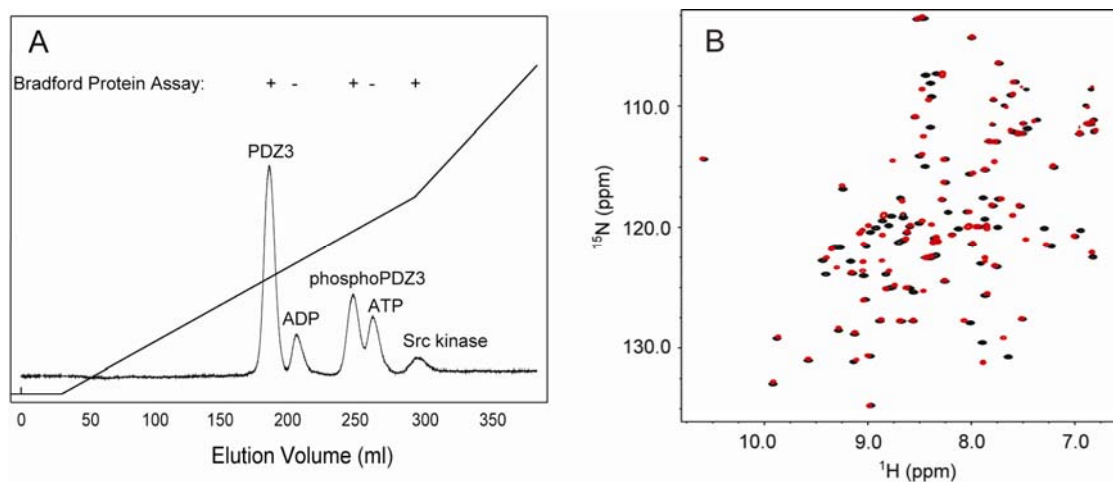


Figure 2.2: Purification of phosphoPDZ3. (A) Ion exchange chromatography elution profile of phosphoPDZ3 purification, monitored by UV absorbance at 280 nm. The NaCl elution gradient is shown as straight lines. (B) ¹⁵N-HSQC of phosphoPDZ3 (red) and wild type PDZ3 (black).

2.3.2 Phosphorylation-induced undocking of $\alpha 3$ lowers affinity for CRIP1 ligand

To determine the effect of phosphorylation at Y397 on PDZ3 structure, the backbone chemical shifts of p³⁹⁷-PDZ3 were assigned and compared to unphosphorylated PDZ3. Chemical shift perturbations (CSP) were quantified by measuring the difference between the chemical shifts of PDZ3 and p³⁹⁷-PDZ3 (Figure 2.3A), and these CSPs were mapped onto the structure of PDZ3 (Figure 2.3B). Phosphorylation results in CSPs radiating out from Y397 to include all of $\alpha 3$ and its surrounding regions. While the perturbation pattern is consistent with the general site of phosphorylation, the extent and

specific nature of any structural change accompanying phosphorylation is more difficult to assess strictly from CSPs.

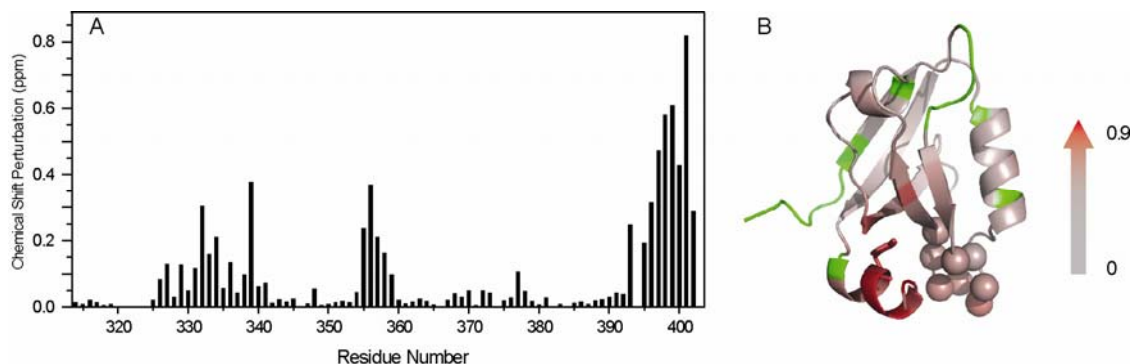


Figure 2.3: Chemical shift perturbation of Y397 phosphorylation. The ^{15}N -HSQC of PDZ3 and phosphoPDZ3 are compared and average chemical shift changes of ^1H and ^{15}N were plot versus residue number (A) and onto crystal structure of PDZ3 (B) using color scale. The average chemical shift perturbations were calculated as $|\Delta\delta^1\text{H}|+0.1*|\Delta\delta^{15}\text{N}|$. The Y397 is shown by sticks and the residues without perturbation data are color in green.

In unphosphorylated PDZ3, the side chain of Y397 packs into side chains of $\beta 2$, $\beta 3$ and the $\alpha 1$ - $\beta 4$ loop of the PDZ core. These hydrophobic interactions help to define how $\alpha 3$ packs against the PDZ core (Figure 2.3B). One possible consequence of phosphorylation is therefore destabilization/unfolding of $\alpha 3$, since the phosphate group might occlude proper packing of $\alpha 3$. In this sense, phosphorylation of Y397 would effectively convert PDZ3 into a C-terminally truncated form, much like PDZ³⁰³⁻³⁹⁵ characterized previously and referred to as $\Delta 7\text{ct}$ [63]. To test this idea, we compared ^1H and ^{15}N amide chemical shifts of PDZ3, p³⁹⁷-PDZ3 and $\Delta 7\text{ct}$ by superimposing HSQCs of the three proteins. Nearly all residues experiencing significant CSPs in p³⁹⁷-PDZ3 (Figure 2.3) display a linear trend of HSQC peaks in the order PDZ3, p³⁹⁷-PDZ3, and $\Delta 7\text{ct}$ (Figure 2.4A). To quantitatively demonstrate linearity of these three sets of resonances, correlation values (adjusted R-values) of linear fitting were calculated and

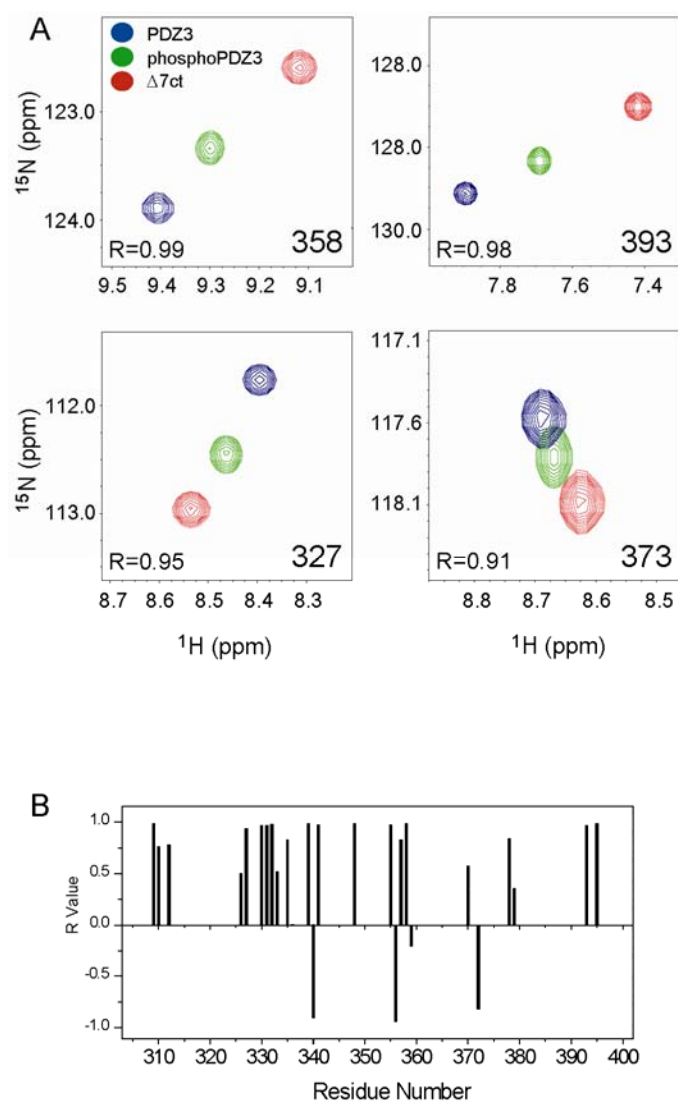


Figure 2.4: Linear resonance pattern of PDZ3, phosphoPDZ3 and $\Delta 7\text{ct}$ ^{15}N -HSQCs. (A) Four representative residues were selected to show the HSQC resonance pattern of PDZ3, phosphoPDZ3 and $\Delta 7\text{ct}$. HSQC peaks of PhosphoPDZ3 (green) fall onto the line defined by PDZ3 (blue) and $\Delta 7\text{ct}$ resonances. Adjusted correlation value (R-value) for each example residue is given in each panel. (B) Adjusted correlation values (R-values) of the resonances with significant chemical shift changes upon phosphorylation. Only the residues with CSP>0.05 ppm were analyzed and R-values were showed.

plotted (Figure 2.4B). Most R-values are around 1, suggesting high linearity. Several outliers are found for residues near the phosphoryl group on Y397, as expected since chemical shifts arise from both conformational and chemical perturbations. The collective collinear pattern of PDZ3, $\text{p}^{397}\text{-PDZ3}$ and $\Delta 7\text{ct}$ peaks indicates fast exchange

between two conformations for p³⁹⁷-PDZ3: one in which $\alpha 3$ is packed as in native PDZ3, and one in which $\alpha 3$ is undocked, and makes no contributions to chemical shifts in PDZ core residues. Thus, p³⁹⁷-PDZ3 exists as an equilibrium of two dynamically exchanging states, represented by PDZ3 and $\Delta 7\text{ct}$, respectively. The fraction of undocked $\alpha 3$ is ~50% and the exchange takes place on a sub-millisecond timescale.

It was shown previously that truncation of $\alpha 3$ decreases binding affinity of PDZ3 with CRIPT peptide by 21-fold [63]. If p³⁹⁷-PDZ3 is indeed a mixture of PDZ3- and $\Delta 7\text{ct}$ -like states, an intermediate binding affinity to CRIPT peptide should be observed. To test this, we performed ITC experiments to measure the binding affinity of p³⁹⁷-PDZ3 to CRIPT C-terminal peptide. The binding affinity of p³⁹⁷-PDZ3 was found to be approximately 4 times weaker than PDZ3, falling in between PDZ3 and $\Delta 7\text{ct}$ (Table 1). Importantly, this change in ΔG due to phosphorylation is mainly attributed to entropy, which is the same signature observed for $\Delta 7\text{ct}$ [63].

Table 2.1: ITC binding parameters for PDZ3 and phosphoPDZ3. CRIPT peptide (NYKQTSV) were titrated in and each experiment was repeated twice. The K_d between $\Delta 7\text{ct}$ and CRIPT is 81 μM

Binding Parameters	PDZ3	phosphoPDZ3
Stoichiometry	0.98 \pm 0.03	0.99 \pm 0.02
K_d (μM)	3.60 \pm 0.28	14.00 \pm 0.47
ΔH (Kcal/mol)	-8.57 \pm 0.31	-8.80 \pm 0.29
$-T\Delta S$ (Kcal/mol)	-1.16 \pm 0.26	-2.18 \pm 0.31

2.3.3 Phosphorylation of Y397 increases disorder in $\alpha 3$

Phosphorylation of Y397 disrupts the packing of $\alpha 3$ with the core domain of PDZ3 as described above. It is, however, unknown how phosphorylation affects local structure of $\alpha 3$. Does $\alpha 3$ still maintain its secondary structure when $\alpha 3$ is undocked from PDZ3?

To answer this question, we analyzed ^{13}C chemical shifts, amide exchange rates, and ^{15}N backbone relaxation in phosphorylated and unphosphorylated PDZ3.

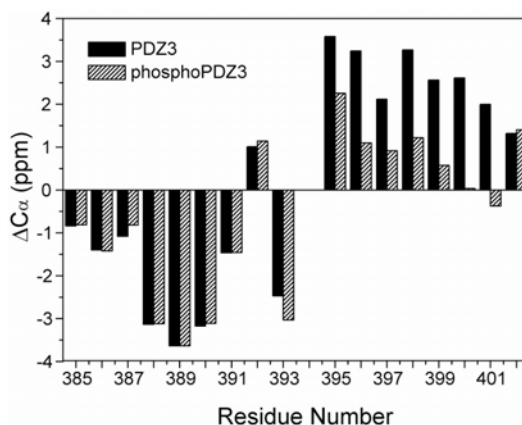


Figure 2.5: C_α chemical shift differences of PDZ3 and phosphoPDZ3 relative to random coil. The C_α chemical shift differences were calculated by subtraction of random coil C_α chemical shifts from those of PDZ3 or phosphoPDZ3. Only $\beta 5$ and $\alpha 3$ were shown in this plot for clarity. The random coil chemical shifts were used as reported by Wishart and Sykes [115].

The $^{13}\text{C}^\alpha$ chemical shift, relative to random coil values, is a sensitive indicator of secondary structure [115]. These relative chemical shift values for unphosphorylated PDZ3 and p³⁹⁷-PDZ3 are shown for the C-terminal residues that include $\beta 6$ ³⁸⁵⁻³⁹² and $\alpha 3$ ³⁹⁴⁻³⁹⁸ (Figure 2.5). Phosphorylation clearly diminishes helicity in $\alpha 3$ as determined from $^{13}\text{C}^\alpha$ chemical shift, whereas it has no effect on $\beta 6$ structure.

Amide proton exchange was characterized by SEA-HSQC (solvent exposed amides HSQC) experiments. This approach was used knowing that amides in the $\alpha 3$ region exchange rapidly (data not shown). In a SEA-HSQC spectrum, the intensity of an amide resonance is proportional to the extent to which it is solvent exposed [116]. As shown in Fig. S2.1A, only surface exposed residues of PDZ3 are observed. The undocking of $\alpha 3$ is expected to increase solvent exposure, which should be evident from SEA-HSQC

intensity changes. It is, however, not appropriate to directly compare SEA-HSQC intensities of PDZ3 and phosphoPDZ3 samples, as intensities are differentially affected by protein concentration and tumbling times. Therefore, intensities were normalized (see Experimental Procedures) to facilitate direct comparison. SEA-HSQC peak intensities of PDZ3 and p³⁹⁷-PDZ3 are plotted against one another in Fig. S2.1B. A good correlation is obtained as indicated by R-value of 0.98, and a scaling factor of 0.74 (for p³⁹⁷-PDZ3 relative to PDZ) was observed, indicating increased amide exchange in p³⁹⁷-PDZ3. As expected, α 3 and its docking region display increased solvent exchange (Figure S2.1C, D), while other regions have no significant changes in solvent accessibility.

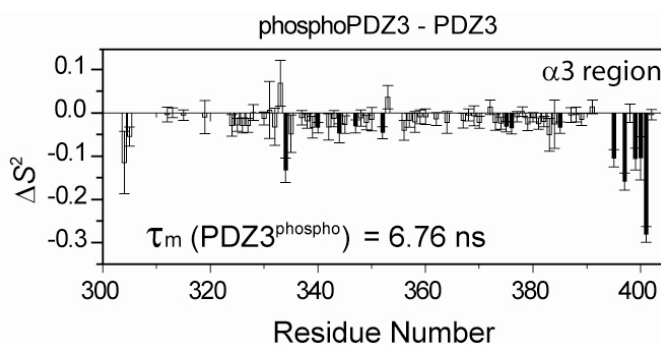


Figure 2.6: Backbone amide order parameters (S^2). The ΔS^2 was calculated by subtraction of phosphoPDZ3 order parameter from PDZ3 order parameter. The residues with significant order parameter changes ($\Delta S^2 > 2\sigma$) are shown by filled bars. The data were acquired on a 500 Varian magnet.

To directly determine the degree of flexibility in p³⁹⁷-PDZ3, we employed ¹⁵N backbone relaxation coupled with model-free analysis [117] to yield an order parameter, S^2 , for each residue. The most significant change in S^2 upon phosphorylation is in the α 3 region, showing decreases of 0.1-0.3 (Figure 2.6). Given that the undocked fraction is only 50% and assuming that the docked state yields high values of S^2 , this represents a dramatic increase in ps-ns flexibility in α 3, and strongly suggests that in the undocked

state it is unfolded and highly dynamic. In addition, a slight overall decrease in S^2 is observed throughout the PDZ core, which is suggestive of an overall small increase in backbone dynamics in p³⁹⁷-PDZ3. These results are similar to that found in $\Delta 7\text{ct}$, which showed large increases in side-chain dynamics and subtle increases in backbone dynamics [63]. It is noteworthy that the protein tumbling is greatly retarded by the unfolding of $\alpha 3$, as indicated by the increased global tumbling correlation time, τ_m , which increases from 5.9 to 6.7 ns upon phosphorylation at Y397.

2.3.4 Phosphorylation disrupts PDZ3-SH3 association

In vivo, phosphorylation does not occur in the specific PDZ construct used here (304–402), but rather, it occurs in the context of full-length PSD-95 (Figure 2.1). While it may not be feasible to probe this 73 kD protein for phosphorylation effects by NMR, we hypothesized that some full-length behavior might be captured in shorter multidomain constructs. Thus, we set out to characterize the behavior of PDZ3 in a construct that spans residues 304–532, which includes the SH3 domain and the linker preceding it. In addition, the F-strand from the GK domain (residue numbers 713–724) was added to the C-terminus to enhance stability [35]. This PDZ3-SH3 construct yielded reasonable quality HSQC spectra from which the effects of phosphorylation could be monitored.

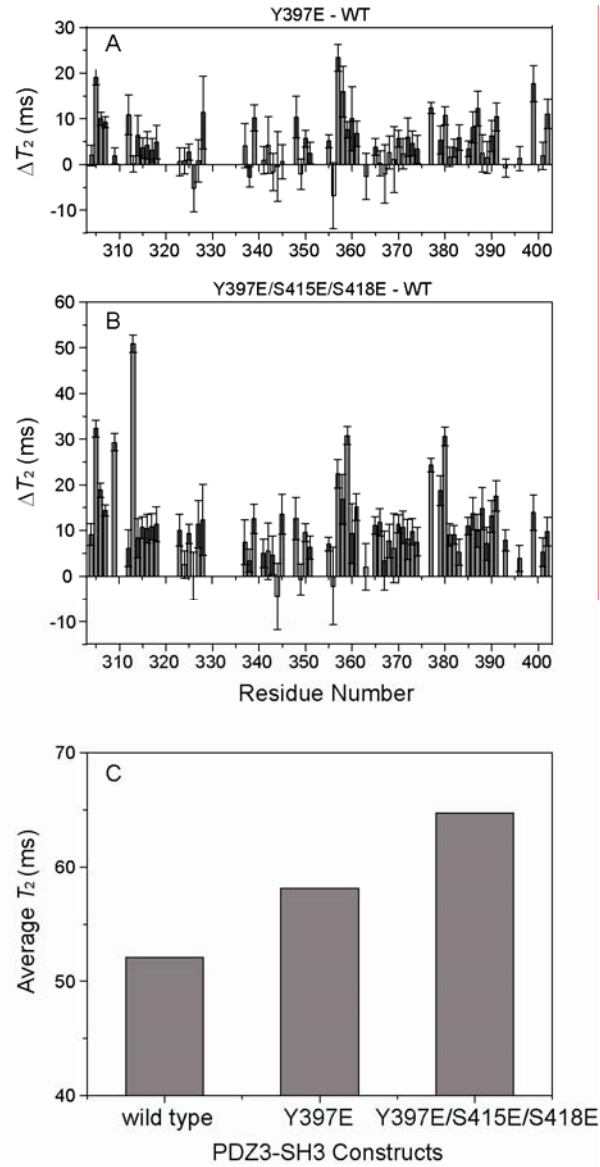


Figure 2.7: T_2 analysis of PD3-SH3, Y397E and Y397E/S415E/S418E mutants. (A) T_2 difference between PDZ3-SH3 Y397E single mutant and wild type PDZ3-SH3. (B) T_2 difference between PDZ3-SH3 Y397E/S415E/S418E triple mutant and wild type PDZ3-SH3. (C) The average T_2 values for wild type, single and triple mutants. The residues with significant T_2 increases were shown by filled bars.

In PDZ3 alone, phosphorylation at Y397 increases $\alpha 3$ undocking and unfolding. In the intact MAGUK, because $\alpha 3$ precedes a ~20 residue linker, much of which is highly conserved, one possibility is that phosphorylation will weaken or enhance putative

domain packing between PDZ3 and SH3. To test this, ^{15}N backbone transverse relaxation times (T_2) were measured in PDZ3-SH3. These T_2 times are highly sensitive to the rate of tumbling experienced by individual sites. An overall increase in T_2 is expected for a reduced degree of domain-domain packing since loss of packing would lead to more time spent tumbling as a dissociated domain. For these experiments, phosphorylation at 397 in PDZ3-SH3 was mimicked by the Y397E mutation. T_2 values for this and wild-type constructs were measured and their differences are shown in Figure 2.7A. In general, PDZ3-SH3 Y397E shows 3~25 ms longer T_2 values relative to wild type. It is noteworthy that phospho-tyrosine is not perfectly mimicked by glutamic acid. Thus, it is reasonable to expect an even larger increase in T_2 for authentic phosphorylation of Y397. The increase in T_2 at virtually all residues suggests that phosphorylation at Y397 reduces the interaction between PDZ3 and SH3, which is stabilized by the presence of $\alpha 3$ secondary structure.

Two additional serine phosphorylation sites (S415 and S418) within the PDZ3-SH3 linker region have been reported [48]. The fragment where S415 and S418 are located corresponds to a fragment which was shown to contribute to communication between PDZ3 and GK in the PSD-95 homolog Dlg-1 [29]. Specifically, deletion of or replacement of this “ $\Delta 2$ ” fragment with random coil abolishes SH3’s PDZ3-dependent interaction with GukHolder. Because of these residues’ proximity to $\alpha 3$ and their conserved nature (Figure 2.1B), we created a triple “phosphorylation” mutant to test the effect of phosphorylation at these two additional sites. ^{15}N T_2 measurements were made on Y397E/S415E/S418 triple mutant of PDZ3-SH3. Compared with the Y397E single

mutant, the triple mutant exhibits even higher T_2 values (Figure 2.7B), suggesting further dissociation of PDZ3 and SH3 domains.

2.4 Discussion

2.4.1 Regulation in PDZ domains

When PDZ domains are excised from their parent proteins, they typically behave as simple binders of C-termini, which is documented by the many determined structures of individual PDZs and their cognate ligands [118]. Current evidence indicates, however, that PDZ function can be influenced by flanking sequences and/or domains, as well as intermolecular interactions [109]. The PDZ domain of Par6 alters its binding affinity for ligand upon binding of Cdc42 to the semi-Crib motif, which is immediately N-terminal to the PDZ domain, and augments its β -sheet [14]. In another example, “PDZ proteases” are in turn regulated by changes in PDZ structure [96]. PDZ function has also been shown to be regulated by redox events within the PDZ domain [119]. The idea that PDZ domains are involved in higher-order regulatory events is consistent with their locations (often in tandem) in proteins involved in organization of signaling complexes, sub-cellular transport, and cell-cell adhesion [16, 118].

Here, we show how PDZ3 from PSD-95 is regulated by phosphorylation of Y397, which lies outside the strict PDZ boundary in a C-terminal extension that augments the PDZ core structure [9, 63]. Although phosphorylation was shown to regulate function of the PDZ protein NHERF1, the phosphorylation sites are far from the PDZ domains and their precise mechanism of release of autoinhibition remains to be elucidated [99]. In contrast to phosphorylation of PDZ domains themselves, there are numerous examples of

phosphorylation of PDZ substrates [100-108]. Phosphorylation typically occurs at positions (-2) to (-4), and though this usually results in weakening of the PDZ-ligand interaction, there are examples of phosphorylation strengthening the interaction [106-108]. Thus, phosphorylation appears to be a recurring regulatory mechanism in PDZ mediated interactions. Though there is currently little direct characterization of how phosphorylation influences PDZ domains, proteomic work suggests that phosphorylation in PDZ core or flanking sequences is relatively common. As collected in the UniProt database (www.uniprot.org), numerous phosphorylation sites have been experimentally confirmed (mostly in murine proteins) for the PDZ proteins Zo-1, GRIP1, MAGI2, MAGI3, and Par3, for example. Many of these phosphorylation sites exist in short “linkers” between domains, as observed here in PSD-95, but also within the PDZ domains.

2.4.2 Phosphorylation at Y397 allosterically regulates C-terminus binding

We successfully phosphorylated at Y397, a construct of PDZ3 that includes an α -helical C-terminal extension that ends at position 402. A combination of chemical shift analysis, amide hydrogen exchange, and ^{15}N relaxation showed that phosphorylation partially undocks the $\alpha 3$ helix from the PDZ3 core. The chemical shifts (Figure 2.4) convincingly show that $\text{p}^{397}\text{-PDZ3}$ exists as a rapid equilibrium between a docked state in which $\alpha 3$ is natively packed (~50%) and an undocked, unfolded state (~50%). This conclusion was only possible because of previous work on $\Delta 7\text{ct}$, which eliminates native $\alpha 3$ by truncation of residues 396-402 [63]. In that study, $\alpha 3$ was shown to confer a 21-fold increase in binding affinity to CRIPT peptide. Without $\alpha 3$, the PDZ3 core has

enhanced side-chain dynamics which are quenched upon CRIPT binding. This confers an entropic penalty to binding, which was detected through isothermal titration calorimetry. Interestingly, because $\alpha 3$ does not contact CRIPT peptide, this was considered a novel “dynamic” allosteric mechanism. Here, we show that this dynamic mechanism has biological significance and is minimally induced by phosphorylation at Y397. The 4-fold reduction in CRIPT binding affinity (as opposed to 21-fold) is consistent with the 50% population of unfolded $\alpha 3$. The behavior of p³⁹⁷-PDZ3 also confirms that $\Delta 7\text{ct}$ serves as an excellent proxy for phosphorylated PDZ3 constructs.

2.4.3 Phosphorylation tunes interdomain interactions in the PDZ3-SH3-GK MAGUK core

A caveat of the results on p³⁹⁷-PDZ3 (residues 304-402) here is that the construct remains artificial as an excised domain. One reason in support of using this construct is that phosphorylation at Y397 became less efficient upon further extension of the C-terminus (data not shown). Nevertheless, the role of the linker may be important. Although there is no crystal structure of full-length PSD-95 or the PDZ-SH3-GK supradomain from any MAGUK, there is evidence for interaction between PDZ3 and SH3-GK. From electron microscopy, intact PSD-95 appears as a “C-shaped” arrangement of domains [21]. In other work, binding assays on various constructs of PSD-95 family MAGUKs suggest interdomain allostery between PDZ3 and the SH3-GK module. In the case of PSD-95, PDZ3 (as well as PDZs 1 and 2) was shown to influence binding of Map1a, which binds to the GK domain [28]. In the case of the PSD-95 homologue Dlg1 from *drosophila*, PDZ3 influences binding of GukHolder, which binds to the SH3

domain [29]. Structural insight into how PDZ3 and its following linker interact with SH3-GK is needed to unravel the basis for these interactions and how they are regulated.

To gain insight into how PDZ3 interacts with SH3-GK and whether phosphorylation plays a role, we studied a PDZ3-linker-SH3 construct. ^{15}N T_2 measurements within the PDZ3 domain for wild-type, as well as for a Y397E phosphomimic and a triple phosphomimic construct, Y397E/S415E/S418E. S415 and S418 have also been confirmed to be phosphorylated [31, 32], and therefore a combination of these sites may be phosphorylated under different signaling and cell contexts. Phosphorylation at Y397 increased the mobility of PDZ3, and this effect was increased further for the triple mutant (Figure 2.7). This is consistent with a model in which PDZ3 interacts with SH3-GK via the SH3 domain and phosphorylation at 397 in $\alpha 3$ and 415/418 in the linker disrupt this interaction (Figure 2.8). To our knowledge, these are the first reported physical data that relate PDZ3 to SH3 for any MAGUK; there are no reported structures for any construct containing PDZ3 and SH3 domains, although structural models of PDZ3-SH3-GK have been proposed [120]. The T_2 results suggest that additive phosphorylation interferes with the putative PDZ3-SH3 interaction. It is currently unknown in which order these three sites are phosphorylated, but it is possible that phosphorylation of S415/S418, which are seated in a putatively flexible fragment (SSLGSG), precedes phosphorylation of Y397 which is mostly buried. Phosphorylation of S415/S418 may then facilitate Y397 phosphorylation by loosening the domain packing between PDZ3 and SH3, or providing binding sites for the kinase that phosphorylates Y397. Overall, our NMR relaxation measurements suggest that phosphorylation of Y397, S415 and S418 cooperate together to regulate inter-domain communication of PSD95.

It is currently unclear how conserved these phosphorylation events are. The PSD-95 family of proteins is comprised of PSD-95, PSD-93, SAP97, and SAP102. Although there is high sequence conservation in the $\alpha 3$ and linker among these proteins, phosphorylation at Y397 has only been confirmed for PSD-95 and PSD-93, and phosphorylation at 415/418 has only been observed so far in PSD-95. While it may be possible that differences in phosphorylation patterns in this region contribute to functional differences between these MAGUKs (which also have functional redundancies), this issue may not be clear until more in-depth phosphorylation mapping is carried out.

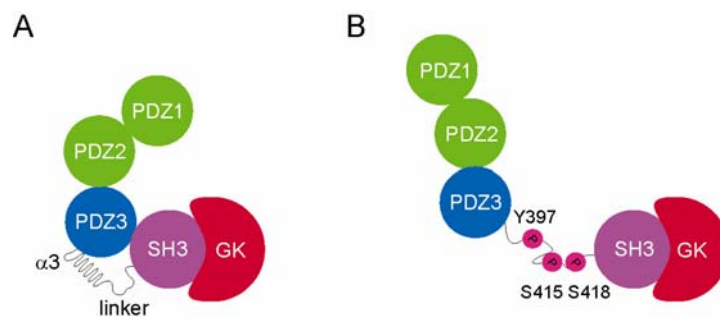


Figure 2.8: Schematic explanation of function of Y397, S415 and S418 phosphorylation in PSD-95. The third α -helix is unfolded upon phosphorylation, which consequently interrupts the domain packing between PDZ3 and SH3.

2.5 Concluding remarks

PDZ domains are primarily appreciated for their simple function of binding C-terminal sequences. However, PDZs are typically embedded in lengthy protein sequences characterized by multiple other structured domains and significant stretches of unknown structure/flexibility. Understanding native PDZ function therefore often requires consideration of these additional elements. There are now a number of examples of PDZ

domains whose core structures are augmented by N- or C-terminal, and a recent review predicts that one-third of PDZ domains contain such structural augmentations. We show here that the effects of such additional segments can be dynamically modulated by phosphorylation, which builds upon previous work that showed that the external segments can regulate PDZ function. In many multidomain proteins, the role of interdomain linkers is not well understood. By mimicking phosphorylation at Y397 and in the linker of the PDZ3-linker-SH3 construct from PSD-95, we detected progressive increases in mobility in PDZ3 due to linker phosphorylation. This suggests that the linker plays a key role in supradomain assembly. We propose that linkers in MAGUKs and in other PDZ proteins can adopt varying degrees of structure\flexibility that serves to tune interdomain communication.

2.6 Acknowledgements

We thank Jennifer Cable (UNC-CH, Department of Biochemistry and Biophysics), Karl Koshlap (UNC-CH Eshelman School of Pharmacy, NMR Facility), Ashutosh Tripathy (UNC-CH Macromolecular Interactions Facility), Dan Cline (UNC-CH Eshelman School of Pharmacy) and Brenda Temple (UNC-CH, Structural Bioinformatics Facility) for technical assistance. We also thank John Kuriyan for providing the expression plasmid for Src kinase. This research was funded by NSF grant MCB-0344354 (to A.L.L.) and bridge funding provided by UNC and the Eshelman School of Pharmacy.

Chapter 3

NMR study of allostery within PSD-95

3.1 Introduction

Cell signaling is of central importance for all cellular activities, from cell division and metabolism to programmed death. In metazoa, one of the protein families fulfilling cell-cell communication is known as membrane associated guanylate kinases (MAGUKs), whose function is to organize signaling complexes at cell or synaptic junctions[17, 121]. As a sophisticated type of cell communication, neuronal signaling is transmitted by a highly specialized apparatus, the synapse. The MAGUK subfamily responsible for stabilizing the neuron synaptic junction is known as the postsynaptic density proteins (PSD) or PSD-MAGUKs, which contain four homologues, PSD-95, SAP97, SAP102 and PSD-93[121, 122]. These proteins have the same domain architecture characterized by three PDZ domains (PDZ1-3), an SH3 and GK, of which the C-terminal three domains, PDZ3-SH3-GK, comprise the MAGUK core shared throughout MAGUK family[121]. All four PSD proteins are highly enriched in the central nervous system [122, 123], and share similar spectrum of binding specificities, but they are distributed at different cell compartments and expressed at different stages of neuron development. For example, PSD-95 and PSD-93 are concentrated in the post-synaptic density and expressed at a later stage, while SAP97 and SAP102 are mainly found in dendrites and axons, expressed at early stages of neuron development [6, 124].

The functions PSD-MAGUKs are involved in synapse genesis, organization, stability, and membrane protein trafficking[121]. Malfunctions of MAGUK proteins have been found to be related to reduced performance in learning and memory, Alzheimer's Disease, and Huntington's Disease[125]. Due to the vital functions conferred and multiple diseases implicated, MAGUK proteins have drawn attention as a promising pharmacological target[125]. The comprehensive understanding and pharmaceutical relevance of MAGUK proteins requires studies at the structural level.

Currently, structural studies of PSD-MAGUK proteins are mainly focused onto individual domains. In summary, all five domains of PSD-95 homologue proteins are protein interacting modules. PDZ and SH3 domains are well known protein interaction modules. Interestingly, the GK domain, which is a guanylate kinase homologue, has no catalytic activity[126]. The guanylate binding site, as suggested by Reese et al., is used to accommodate protein ligands, such as MAP1A and GKAP[43]. It is therefore not surprising that PSD proteins are associated with so many targets and involved in so many functions. However, what is unknown is how the binding events of different domains are coordinated in an appropriate temporal sequence. What is more relevant to the function of signal complex organizer is how a desired signal complex is selected among large pools of target candidates. There is no answer to these questions yet, but some hints have emerged from accumulated studies.

Interdomain allostery is a potential approach to regulation of PSD proteins. Several instances of interdomain allostery have been reported for PSD proteins or their homologues. A study on SAP97 suggests that the Hook domain of SH3 interacts with calmodulin[39]. Interestingly, this interaction is enhanced by the presence of PDZ

binding peptides, such as CRIPT and NR2B[38]. Interdomain allostery is also reported in PSD-95, in which association of GK with MAP1A is promoted by PDZ3 binding peptides, CRIPT, APC, Kv1.4 and NR2B[28]. Interdomain communication is found in a PSD homologue in *drosophila*,Dlg1[29]. In this protein, the PDZ domain is indispensable for interaction of SH3-GK with Gukholder, whereas the PDZ binding peptide abolishes the interaction between SH3-GK and Gukholder[29]. The interdomain allostery within MAGUK proteins implicates that binding events of different domains follows a strict order and interplays each other. From the perspective of evolution, the interdomain communication seems to be encoded into primary sequences of PSD-MAGUKs. Compared with the canonical domains, PDZ3 and SH3 of PSD proteins are “modified” or “customized” in that a conserved C-terminal extension is present at PDZ3, and an α -helix/loop insertion, known as the Hook domain, is found in SH3. Qian et al. suggested that the C-terminal extension between PDZ3 and SH3 is important for interdomain communication of PDZ3 and SH3-GK[29]. The replacement of the linker region by Gly-Ser repeats ceased the allostery of PDZ3 and SH3-GK[29]. However, the structural basis by which this allostery exists is still unknown.

Considering the critical roles of PSD-MAGUKs in synapse function, it is expected that this family of proteins is under tight regulation. Two dominant approaches of PSD-MAGUK regulation are at working via palmitoylation and phosphorylation[121]. In PSD-95, palmitoylation transfers a fatty acid group to the N-terminal Cys3 and Cys5, and is related to dimerization of PSD-95[24, 25]. Phosphorylation of PSD-MAGUKs, however, is observed throughout the entire primary sequence[121]. Of relevance to this research, many phosphorylation sites of MAGUKs are located at the linker regions of

subdomains. For example, Ser295 located at PDZ2/PDZ3 linker of PSD-95 is phosphorylated. It has been suggested that phosphorylation of Ser295 regulates the expression level of PSD-95[127]. In SAP97, phosphorylation of PDZ2/PDZ3 linker disrupts the association of GK with GKAP[45]. In PSD-95, another hot phosphorylation region is the PDZ3/SH3 linker, where Y397, S415 and S418 are phosphorylated. In the previous chapter, we suggested that phosphorylation of these sites increases domain flexibility of PDZ3 and SH3, indicating a disruption of domain packing.

Because of the multiple domain and linker involved, the structural mechanism of interdomain allostery and phosphorylation regulation of PSD proteins cannot be understood by the divide-and-conquer strategy used on excised domains. Of the few structural studies on tandem domain of PSD proteins, the role of the PDZ3 domain was always neglected, although the PDZ3 domain is known as an indispensable component of MAGUK core [43, 44]. In this research, we have studied the structure and dynamics of PSD-95, in an attempt to understand the PDZ-nonPDZ interaction. We first determined the orientation of PDZ3 relative to SH3 using PRE and chemical shift perturbation. We further find that CRIPT binding changes the relative orientation of PDZ3 and SH3. Consistent with reported results, the replacement of the PDZ3/SH3 linker reorients PDZ3 relative to SH3 in the same way as CRIPT binding. Finally, SAXS data on PDZ3-SH3-GK were used to build the structure of the MAGUK core. The SAXS model suggests PDZ3 is docking to the SH3 region adjacent to the Hook domain, which is consistent with our study on PDZ3-SH3 construct. We also monitored the motions of Hook domain, and infer the function of Hook in mediating allostery between PDZ3 and GK domain. Finally, we carried out Rosetta simulations to obtain higher resolution

structural models of the MAGUK core. We found that PDZ3 binds the PDZ3/SH3 linker, which brings PDZ3 close to SH3.

3.2 Experimental Procedures

3.2.1 Plasmid constructs.

Rat PSD-95 with the first 60 residue truncated (61-724) was used as a template to make all constructs of this study. All constructs were sub-cloned into a pET21a vector with a TEV cleavable N-terminal histidine tag. The amino acid sequences of all constructs are as following: PDZ3-SH3-F (304-530 plus F strand 712-724, which is connect to rest part of PDZ3-SH3 by 3 GS repeats), SH3-GK (430-724) and PDZ3-SH3-GK (304-724). To prepare constructs for PRE experiments, undesired native cysteines were mutated to serines by quick change mutagenesis PCR. The cysteines were reintroduced into desired sites for MTLS labeling purpose. The constructs for MTSL labeling were PDZ3-SH3-F C445C, PDZ3-SH3-F W507C, PDZ3-SH3-F W499C, PDZ3-SH3-F Δ 1 Δ 2 (in which two regions corresponding to EYSRFE and LMNSSLGSGTASLR were replaced by GS repeats), PDZ3-SH3-GK C445C, PDZ3-SH3-GK Y604C and PDZ3-SH3-GK S699C.

3.2.2 Protein expression and purification.

Transformed *E. coli* BL21 (DE3) cells were grown at 37 °C in LB medium or minimal medium containing appropriate isotopes. When cell density reached an OD₆₀₀ of 0.6, IPTG was added to a final concentration of 1 mM and the cells were grown for

another 16 hours at 22 °C. The cells were harvested by centrifugation and stored at -80 °C until use.

All proteins were purified using the following protocol. The cell pellets were re-suspended in 50 mM Tris-HCl, pH 8.0, 200 mM NaCl, 0.1% triton X-100, 25 mM imidazole and 1 mg/ml lysozyme. The re-suspended cells were subjected to three freeze-thaw cycles and applied to sonication. The centrifuged cell lysate was loaded to a nickel affinity column and eluted with 500 mM imidazole. The fractions containing proteins were pooled and subjected to overnight TEV cleavage at 4 °C. TEV was added to a final concentration of 25 µg/ml. A 100% cleavage was achieved as suggested by SDS-PAGE. The cleaved sample were further purified by Source Q ion exchange chromatography, followed by a G75 size exclusion column equilibrated in a buffer containing 50 mM Tris-HCl, pH 7.5, 200 mM NaCl and 2.0 mM DTT. The identity and purity of proteins were verified by SDS-PAGE. The protein concentrations were determined by UV using extinction coefficients obtained by ExPASy-ProtParam tool.

3.2.3 Peptide synthesis.

The 7-mer CRIPT peptide (Ac-NYKQTSV-COOH) was synthesized and purified as reported [63]. The identity and purity of the peptide are verified by mass spectroscopy. The peptide concentration is determined using UV with an extinction coefficient of 1490 cm⁻¹M⁻¹.

3.2.4 NMR experiments.

All NMR samples, except those for PRE measurement, were dissolved in 50 mM Tris-HCl, pH 7.5, 200 mM NaCl, 2 mM DTT and 10% D₂O. The proteins for PRE measurements were dissolved in the same buffer without DTT. MTSL labeled samples were prepared by mixing appropriate proteins with MTSL in a protein: MTSL ratio of 1:5. The mixture was placed at 4 °C for overnight or room temperature for 2 hrs. Surplus MTSL was removed by loading sample to a size exclusion column Sephadex G25. The MTSL labeled protein samples were concentrated to 0.4 mM. The diamagnetic samples were made by adding 5 µl of 1M ascorbic acid stock solution into paramagnetic samples. Paramagnetic and diamagnetic spectra were recorded on a 600 or 700 MHz magnet equipped with ¹H/¹⁵N/¹³C probe and z-axis pulsed field gradient. Proton transverse relaxation rates of paramagnetic and diamagnetic states were measured using pulse sequence as reported [78, 128]. The delays were set to 0.013, 0.02, 0.03 and 0.04 s⁻¹. The pure PRE rates were calculated by subtraction of diamagnetic rates from paramagnetic rates. All NMR spectra were processed by NMRPipe and analyzed by NMRViewJ.

3.2.5 Small angle X-ray scattering experiments.

Protein samples for SAXS experiments were exchanged into a buffer containing 50 mM Tris-HCl, 200 mM NaCl, 5 mM DTT and 1.25% glycerol by 48 hours dialysis. All samples were prepared at least at three different concentrations ranging from 0.5 to 4 mg/ml to detect subtle aggregation or oligomerization. SAXS data for PSG were collected at protein concentrations of 0.84, 1.68, 2.69 and 5.64 mg/ml. The dialysis buffer was used for background scattering. SAXS data for CRIPT bound PSG were collected at concentrations of 0.81, 1.61 and 3.55 mg/ml. CRIPT peptide (Ac-NYKQTSV-COOH) was added into PSG samples to a final concentration of 0.5 mM. The protein-peptide

mixture was applied to a spin column with a 10 kD molecular weight cut-off membrane. The filtration solution from the spin column was put back to upper reservoir and repeated two times to wash the membrane. Then the filtration solution was used as blank for SAXS scattering. SAXS data of SG were collected at concentrations of 0.70, 1.71 and 2.84 mg/ml. The samples were centrifuged for 5 minutes at 13000 rpm immediately before scanning. The data were collected at 12ID-B at Advanced Photon Source using a wavelength of 1.033 Å. Each sample was scanned 20 times with 10 seconds exposure for each shot. No radiation damage was detected during scanning. The buffer subtraction was performed using PRIMUS, and the coefficient for buffer subtraction is given by $1 - c\phi$, where ϕ is the protein partial specific volume (0.0073 cm³/g)[129] and c is protein concentration in mg/ml. The Guinier analysis was performed using autorgqw in Atsas up to region $R_g q$ 1.3[130].

The model of PDZ3-SH3-GK was built using the ensemble optimization method. The SAXS data collected at lowest concentrations (0.84 mg/ml and 0.81 mg/ml for apo and CRIPT bound PSG) were used to carry out modeling. The crystal structures of PDZ3 (1BFE, residue 304-402) and SH3-GK (1KJW, residue 430-724) were used as input domains for EOM. The region between PDZ3 and SH3, residue 403-429 was treated as a flexible linker. 10,000 structures were first generated by RanCh, and the following genetic algorithm was carried out by GAJOE to select the ensemble which fits the experimental SAXS data best [86].

3.2.6 Rosetta molecular dynamics simulation.

To build a PDZ3-SH3-GK structural model, FloppyTail protocol in Rosetta framework was used[131]. During the modeling process, unambiguous and ambiguous constraints were used. Unambiguous distance constraints were derived from the proton transverse PRE rates measured with PSG C445 and PS W499C MTSL labeling. The bleached resonances or these with low para- and dia-magnetic intensity ratios ($I^{\text{para}}/I^{\text{dia}} < 0.15$) were assigned an upper distance of 12 Å. The distances were calculated using SB equations. The errors in distance constraints were derived either from the errors in transverse relaxation rates, or arbitrarily assigned to be ± 4 Å, whichever were larger. Ambiguous constraints were from the residues on PDZ3 experiencing chemical shift perturbations. These residues must be in vicinity of the residues from the PDZ3/SK3 linker or SH3-GK, to incur chemical shift perturbation. Only solvent exposed residues in the PDZ3/SK3 linker and SH3-GK are competent candidates for PDZ3 docking. The solvent accessibility of residues on SH3-GK was analyzed using NACCESS [132, 133], and only those with solvent exposed surface area >10% were selected. The ambiguous constraints have an upper boundary of 7 Å.

The PDZ3 crystal structure (1BFE, 304-402) and the SH3-GK crystal structure (1KJW, 430-724) were used in modeling. In the PDZ3 crystal structure, the third α -helix end at residue A402. Our chemical shift data of long PDZ3 construct (304-427) indicate that the α -helix end K403. Therefore, we extended helicity to K403 by constraining backbone C_{α} position of K403. With all these constraints, 5,000 structures were generated and the 20 best scored structures were analyzed.

3.3 Results

3.3.1 PDZ3 is adjacent to SH3 in tertiary structure and brought away by CRIPT peptide binding.

At the end of Chapter 2, I showed that the mutations (Y397E, S415E and S418E) in the linker region of PDZ3/SH3 increase the T_2 relaxation time, suggesting that perturbation of the linker region promotes interdomain flexibility. This result hinted that there must be some interdomain packing between PDZ3 and SH3 to be disrupted. The most straightforward way to confirm interdomain packing is to compare the chemical shifts of PDZ3-SH3 tandem with isolated PDZ3 domain. The interdomain packing perturbs chemical shifts of the residues located at the domain interface. With the

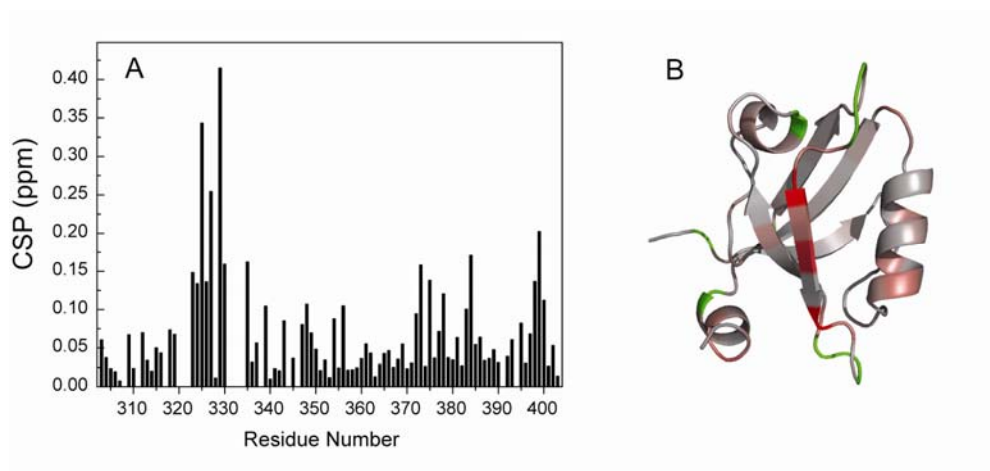


Figure 3.1: Minimal chemical shift perturbation on PDZ3 by PDZ3-SH3 packing. (A) The histogram of minimal chemical shift perturbation. (B) Mapping of minimal chemical shift perturbation onto PDZ3 structure. The magnitudes of CSP were shown in color scale from gray (small) to red (large). The PDZ3 resonances in PDZ3-SH3 construct were assigned based on isolated PDZ3⁴²⁷ assignments. The residues with chemical shift changes were assigned by moving PDZ3 peaks to the nearest ones. The chemical shift perturbation values were calculated using $0.1|\Delta\omega^{15N}| + |\Delta\omega^{1H}|$.

chemical shift assignments of PDZ3 available, we plot the chemical shift perturbation by comparing isolated PDZ3 with PDZ3 coupled with SH3. As shown in Fig. 3.1, the

chemical shift changes caused by presence of SH3 are mainly located around PDZ3 peptide binding groove and the $\beta 2/\beta 3$ loop.

To further probe the interdomain packing of PDZ3 and SH3, we employed paramagnetic relaxation enhancement (PRE). Compared with the NOE, which provides short distance information ($< 6 \text{ \AA}$), the PRE allows detection of long distance constraints up to 25 \AA . The PDZ3-SH3 tandem only has one native cysteine, C445, which is solvent accessible, making it suitable for MTSL labeling. We collected a “paramagnetic” HSQC spectrum of PDZ3-SH3 with MTSL labeling, and diamagnetic HSQC spectrum with MTSL quenched by ascorbic acid. Because the two spectra were acquired at the same protein concentration using identical parameters, the intensity ratios of para- and diamagnetic spectra is reciprocally correlated to the PRE, and positively correlated to the

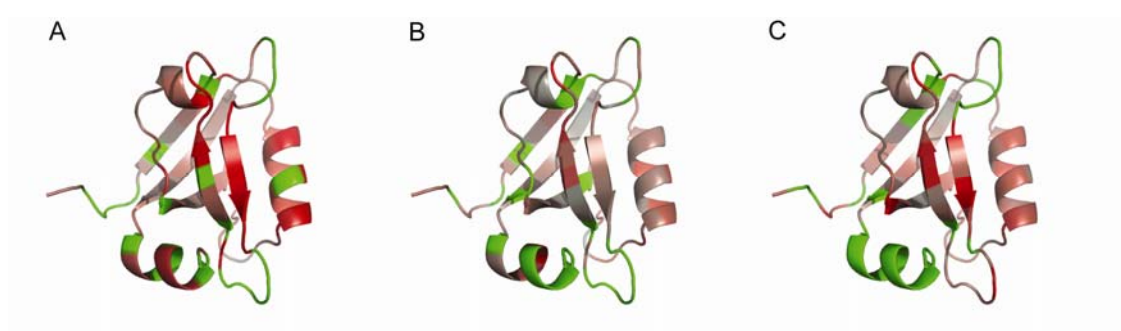


Figure 3.2: PRE perturbation on PDZ3 by C445 MTSL labeling of PDZ3-SH3. The magnitudes of PRE perturbation on PDZ3 with C445 was labeled by MTSL. (A) apo PDZ3-SH3 (B) CRIPT bound PDZ3-SH3 (C) PDZ3-SH3- $\Delta 1\Delta 2$. The magnitudes of PRE are shown using color scale from gray (small) to red (large). The magnitudes of PRE were calculated by $1-I^{\text{para}}/I^{\text{dia}}$. The residues whose data are unavailable are shown green.

distance between the labeling site and the amide of interest. Here we define the intensity ratio of para- and diamagnetic spectra as “PRE”. Labeling of C445 mainly perturbs the PDZ3 peptide binding groove, which is consistent with the chemical shift perturbation

analysis (Fig. 3.2). Subtle perturbation is also observed at the opposite side of the PDZ3 peptide binding face, which may result from the domain flexibility of PDZ3-SH3. These results suggest that PDZ3 is adjacent to SH3 and its peptide binding groove is facing SH3 domain.

The interdomain allostery between PDZ3 and SH3 was reported in a study on PSD-95 homologue in *drosophila*, Dlg1, in which interaction between SH3-GK and Gukholder was abolished by the presence of PDZ3 binding peptides, CRIPT and neuroligin. The mechanism of this interdomain allostery was not investigated. Herein, we investigated the impact of CRIPT binding on the PDZ3-SH3 interaction. Using the above method, we collected para- and diamagnetic spectra of PDZ3-SH3 in the presence of CRIPT peptide. We found that, upon CRIPT binding, the PRE effect that was observed around the PDZ3 peptide binding groove for apo PDZ3-SH3 disappeared, as shown by Fig. 3.2B. The difference in peak intensity ratios ($I_{\text{para}}^{\text{CRIPT}}/I_{\text{dia}}^{\text{CRIPT}} - I_{\text{para}}^{\text{APO}}/I_{\text{dia}}^{\text{APO}}$) for apo and CRIPT bound PDZ3-SH3 is also shown in Fig. 3.3A and 3.3B. The large positive differences are around the peptide binding groove (Figure 3.3 A, B), suggesting this side becomes further from the SH3 domain, while some subtle negative values, whose magnitudes are smaller than the positive ones, are found at the opposite of the peptide binding groove. It is clear that CRIPT binding tends to move the peptide binding face of PDZ3 away from SH3.

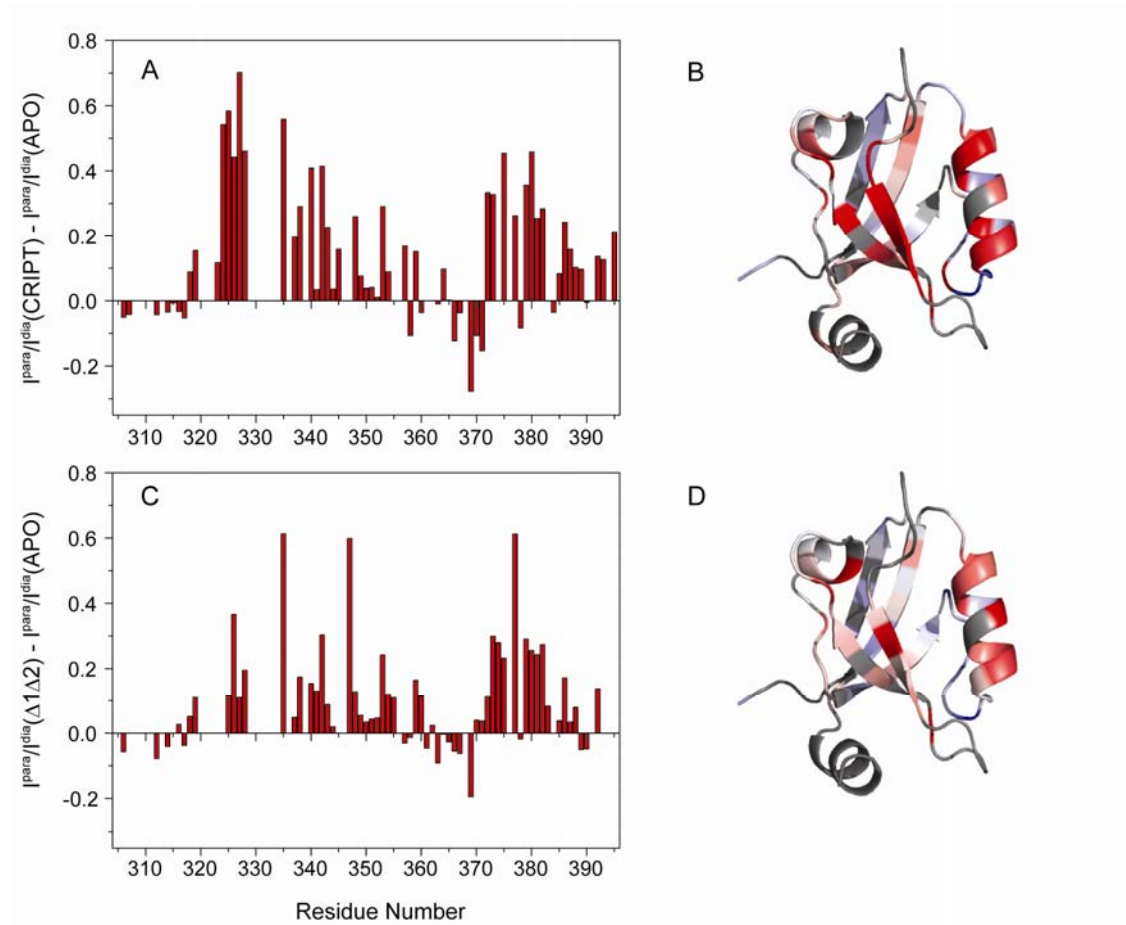


Figure 3.3: PRE perturbation changes by the CRIPT peptide binding (A, B) and the PDZ3/SH3 linker replacement (C, D). The gradient of color scales in B and D is from blue to red, corresponding to the negative to positive values of A and C.

As suggested by the study on Dlg1, the interdomain allostery of PDZ3 and SH3 was also disrupted by deletion or replacement of PDZ3-SH3 linker region by random coli. To quantify the impact of the linker replacement, we made a PDZ3-SH3 construct in which two fragments in linker region were replaced by Gly-Ser repeats. As shown by Fig. 3.2C and 3.3B, the disruption of the PDZ3-SH3 linker region moves PDZ3 away from SH3, similar to the effect of CRIPT peptide binding. The effects of CRIPT peptide

binding and linker region replacement on PRE pattern suggest that two events share a similar way to affect interdomain interactions between PDZ3 and SH3.

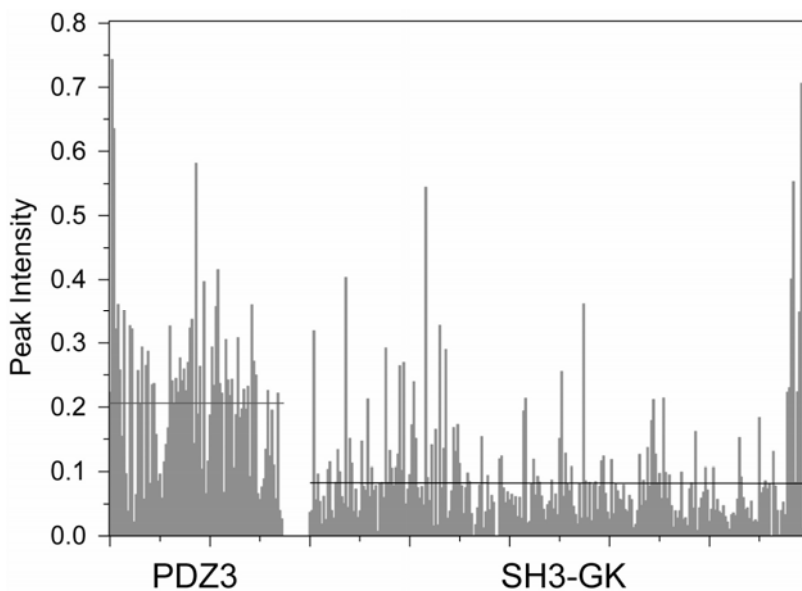


Figure 3.4: HSQC peak intensity statistics of PDZ3-SH3-GK. The PDZ3 resonances were assigned based on isolated PDZ3. The residues that were not assigned in the spectrum were assumed to be from SH3/GK domain. The black bars indicate the average peak intensities of PDZ3 (0.21) and SH3-GK (0.08).

3.3.2 PDZ3 does not form stable and static complex with SH3-GK.

The above studies on PDZ3-SH3 showed that the peptide binding groove of PDZ3 faces the SH3 domain. Still unknown is the relative orientation between PDZ3 and GK. To this end, we further focused our studies onto the PDZ3-SH3-GK (PSG) triple domain construct. From TROSY-HSQC of PSG, 330 peaks were picked out of 420 residues (Fig. 3.4). Over 80% of the PDZ3 resonance peaks were assigned based on isolated PDZ3. Noticeably, the resonances of PDZ3 dominate the HSQC spectrum of PSG. As shown in Fig. 3.4, the average peak intensity of PDZ3 is 0.21, whereas the average value for SG is 0.08. For static complex, individual components are expected to have similar tumbling

times, and consequently comparable peak intensities. This peak intensity difference between PDZ3 and SG suggests PDZ3 is not tightly complexed with SH3-GK (SG).

3.3.3 PDZ3 is not docked into MAP1A binding groove.

As suggested by the previous section, domain flexibility within PSG enables PDZ3 to sample multiple conformations or orientation relative to SG. It is of special interest to know whether PDZ3 is sampling the conformation in which PDZ3 is docked into the MAP1A binding groove of GK, because docking of PDZ3 to MAP1A binding groove provides a possible mechanism by which interdomain communication between PDZ3 and GK is affected. To test this hypothesis, we silenced native cysteines of PSG (C445, C562, C626 and C687), and introduced a mutant cysteine to the MAP1A binding site, Y604. We labeled Y604 using MTSL, and collected paramagnetic and diamagnetic spectra. By comparing the peak intensities of the two spectra, no severe peak intensity attenuation was found on PDZ3 (Fig. 3.5). It indicates that PDZ3 is not close to MAP1A binding site. Thus, interdomain interaction between PDZ3 and GK must be communicated allosterically.

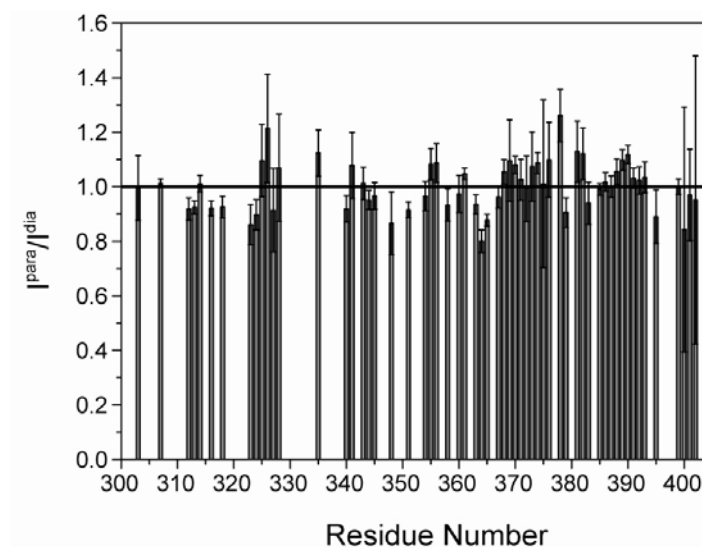


Figure 3.5: Intensity ratio of paramagnetic and diamagnetic spectrum of PSG Y604C. The black bar indicate ratio of 1.

3.3.4 PSG Structural modeling by SAXS.

To understand the interdomain communication between PDZ3/SH3 and PDZ3/GK, a structural model of PSG is required. Isolated domain structures of PDZ3 and SG have been solved by crystallography, making it suitable for SAXS rigid body modeling. High quality SAXS is a prerequisite for reliable modeling results. To detect subtle aggregation and verify data quality, SAXS data at different protein concentrations were scanned (Fig 3.6 and Table 3.1). As shown by table 3.1, radius gyrations calculated at different concentrations yield similar values, indicating samples were well mono-dispersed at low concentrations.

Table 3.1: Radius of gyration at different concentrations			
PSG		PSG+CRIPIT	
Concentration (mg/ml)	R_g (Å)	Concentration (mg/ml)	R_g (Å)
0.8	30.5 ± 0.1	0.81	32.1 ± 0.8
1.7	30.8 ± 0.1	1.61	30.7 ± 0.7
2.7	30.8 ± 0.1	3.55	31.2 ± 0.6

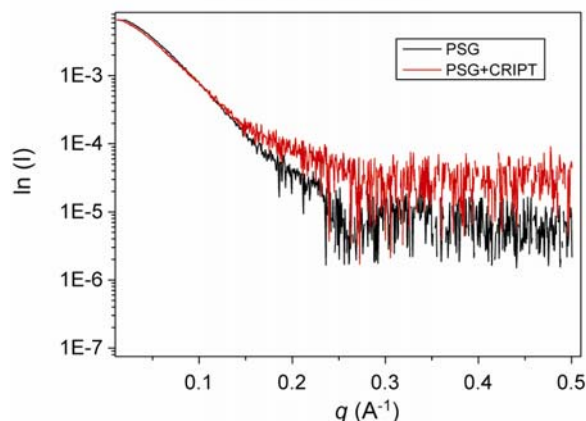


Figure 3.6: SAXS scattering curves of apo and CRIPT bound PSG.

Since PSG may exist as a conformation ensemble, it is appropriate to fit SAXS data using the ensemble optimization method [86]. Crystal structures of PDZ3 and SG were used as input structures and the linker region was treated as a flexible loop. From 10,000 randomly generated structures, an ensemble containing 20 structures which fit SAXS best was selected. The probability distribution (or sampling frequency) of radius gyration for apo PSG and CRIPT bound are shown in Fig. 3.7. In this plot, the integration of all curves is 1. The structure pools created for apo and bound PSG are essentially the same; however, the *selected* conformations of the two samples are distinct. For apo PSG, basically three populated species are identified: a compact conformer with R_g of 25 Å, a major one with medium R_g of 29.5 Å and a lowly populated extended conformer with R_g of 36 Å. Although the similar three conformers are also found for CRIPT bound PSG, there are three distinctions. First, populations of compact and medium forms for CRIPT bound PSG are decreased but the extended form becomes more populated. Second, the peak distribution of medium and extended forms are so broadened that two species become less distinctive. Third, relative to apo PSG, all distribution centers of CRIPT

bound PSG are shifted to larger values. Fig. 3.8 shows the superimposition of 20 structures for PSG in both states. From the structure ensemble, three clusters can be identified, consistent with R_g distribution. The largest cluster consisting of 13 structures is docked to SH3 around the Hook domain. Due to the spherical shape of PDZ3, it is impossible for SAXS to distinguish the orientation of PDZ3 relative to SH3-GK. The other important information from SAXS data is the population of different clusters, which is reflected by the number of structures of each cluster. In contrast, as shown in Fig. 3.8 D and F, no clearly defined cluster can be found for the structural ensemble of CRIPT bound PSG. PDZ3 is evenly distributed around SH3 domain. This observation is consistent with what we found in the previous study on PS construct, in which CRIPT peptide binding somehow disrupts the domain interaction between PDZ3 and SH3.

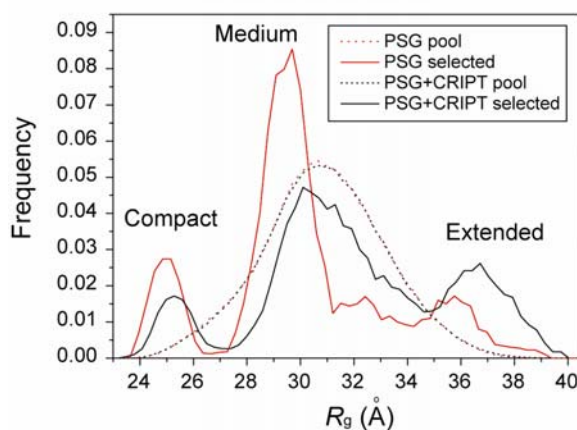


Figure 3.7: Radius gyration distributions of apo and CRIPT bound PSG.

Another interesting finding in SAXS modeling is that PDZ3 is adjacent to the Hook domain. This implies that the presence of PDZ3 could affect Hook domain

conformation, whereas CRIPT peptide binding which releases PDZ3 from SH3 may redistribute the conformation of the Hook domain.

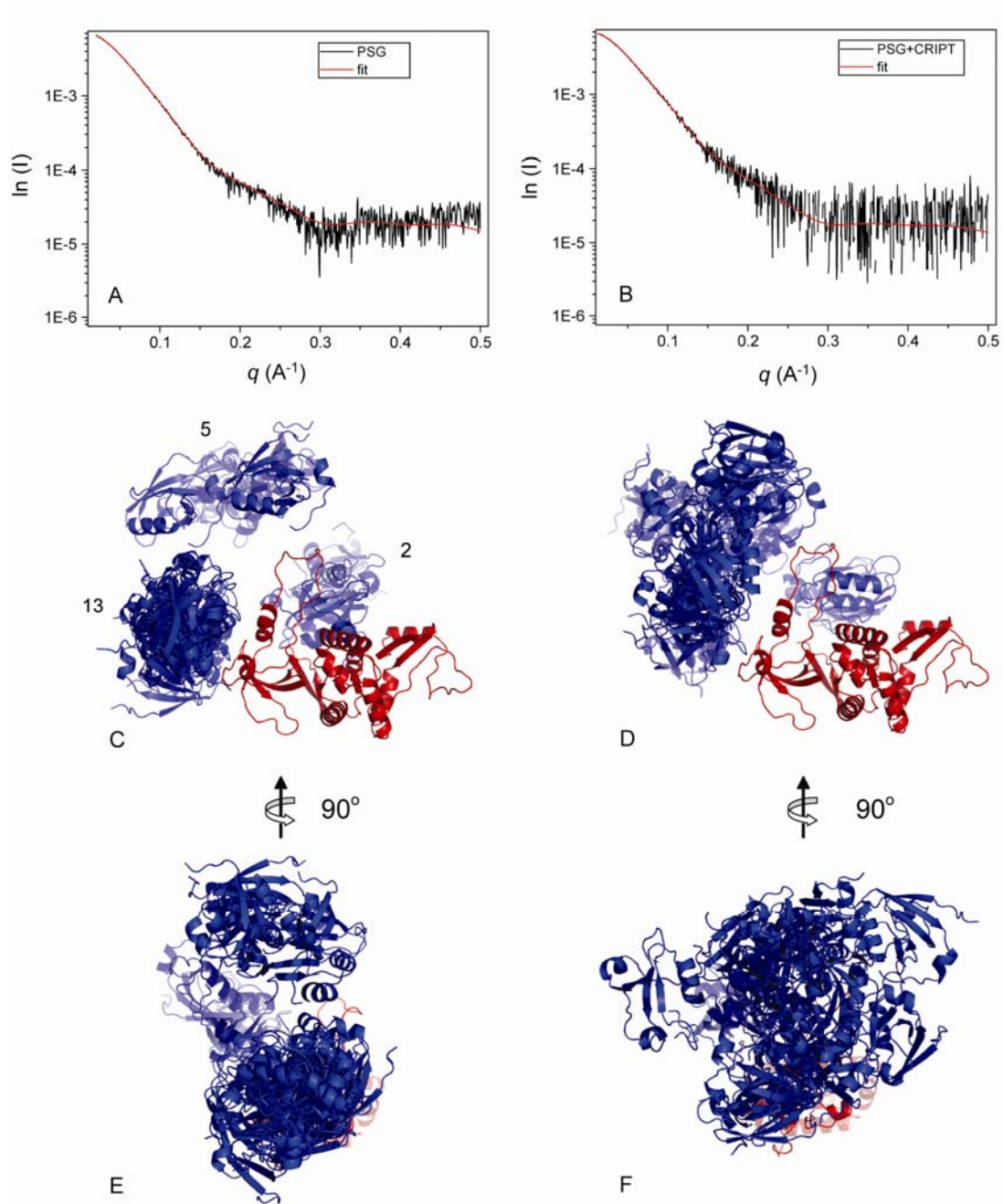


Figure 3.8: EOM fitting results. Apo PSG data and EOM models are shown in left column (A, C, E) and CRIPT bound data and fitting models are shown in right one (B, D, F). PDZ3 domain is represented by blue cartoons and SH3-GK by red ones. E and F rotate 90 degrees relative to C and D.

3.3.5 Intradomain Flexibility of SH3-GK.

MAGUK proteins have low sequence homology in their Hook domains. It is inferred that the Hook domain may be the key component to differentiate functions of different MAGUK proteins. In the SH3-GK crystal structure, the Hook domain displays high B-factors and possesses few contacts with the rest part of the protein. Indeed, our results also suggest that Hook domain is highly flexible. Two distinctive residues in the Hook domain are W499 and W507, whose side-chain ϵ amide proton can be identified by high intensities and characteristic chemical shifts. We further confirmed our speculation by mutating these two tryptophans into cysteines individually (Fig. 3.9A). Interestingly, the peak intensity of W499 and W507 were dramatically attenuated by paramagnetic labeling of C445, Y604 or S696 (Fig. 3.9B, C, D), which are separated far away from each other and from W499 or W507 in the static crystal structure (Fig. 3.10).

As shown in Fig. 3.10, the distances between W499 or W507 and the MTSL labeling centers are beyond the spatial range of strong paramagnetic perturbation (25 Å). One possible explanation is that the Hook domain samples a large spatial range of conformations. W507 located on the flexible loop is able to move freely due to the lack of restraints. The W499, however, is located in an α -helix, whose motions are more restrained than W507. The distance between W499 and Y604C is 38.7 Å. It is unlikely to bring W499 to vicinity of Y604 by just moving W499 while keeping Y604 fixed. It is known that the MAP1A binding groove experiences an open-to-close transition during

peptide binding [43]. Therefore it is possible that the bleaching of W449 resonance results from motions of both Hook domain and GK lid domain where Y604 is located.

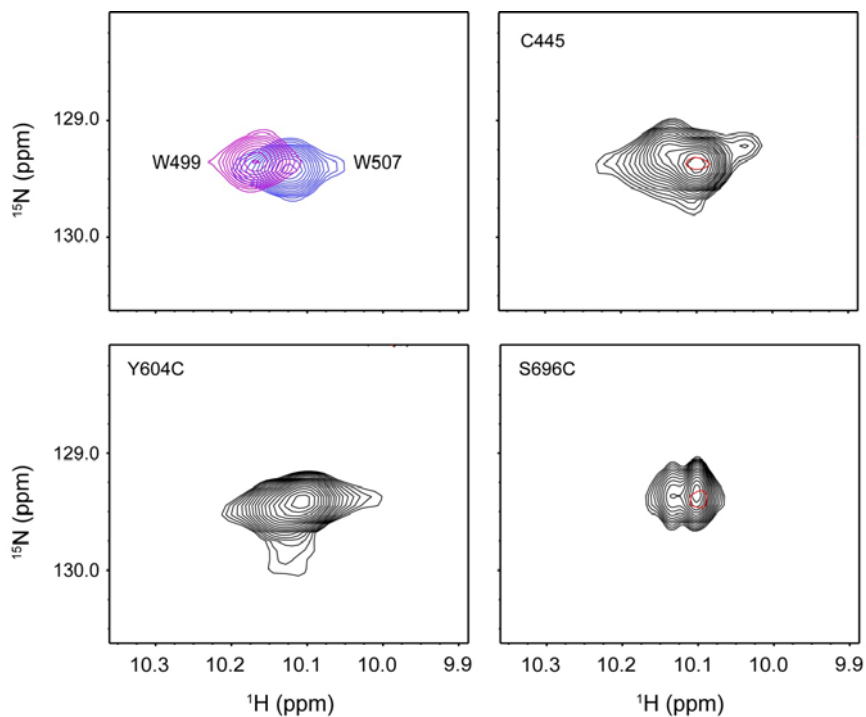


Figure 3.9: Paramagnetic perturbations on W507 and W499. Paramagnetic and diamagnetic spectra are superimposed to display paramagnetic perturbation. Paramagnetic spectra were shown in red and diamagnetic ones in black. (A) HSQC spectra of W507C (magenta) and W499C (blue). Therefore two peaks were assigned as W499 and W507 respectively. Paramagnetic perturbation of the Hook domain by MTSL labeling of (B) C445, (C) Y604C, and (D) S696C.

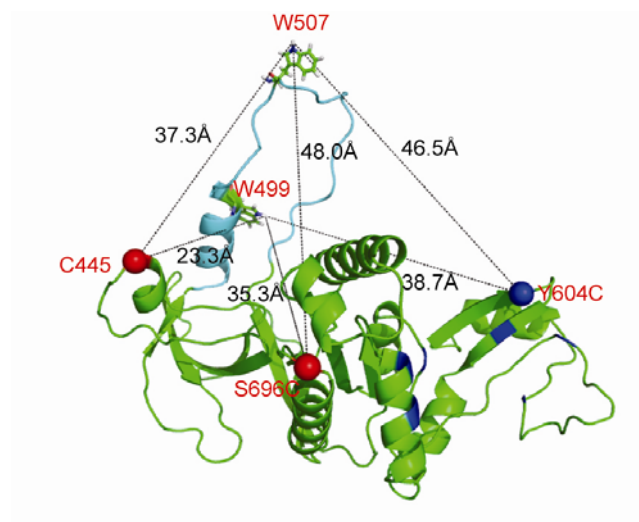


Figure 3.10: Location of paramagnetic labeling sites. The MTSL labeling sites C445, S696C and Y604C are shown as spheres, and W507 and W499 are shown in green sticks. The Hook domain is colored cyan. The residues responsible for MAP1A binding are colored blue. The distances between labeling centers and observation sites are denoted by black lines.

3.3.6 Preliminary modeling results of PSG using Rosetta.

We have shown the orientation of PDZ3 relative to SH3 in a semi-quantitative way using PRE information, and modeling of PSG at low resolution using SAXS. However, the questions still remain: how does PDZ3 interact with SH3-GK and why can CRIPT binding change the conformational distribution of PSG? We also want to know how the domain packing between PDZ3 and SH3 is disrupted by the replacement of the PDZ3/SH3 linker and phosphorylation of Y397, S415 and S418. To answer these questions, we need a high resolution structural model.

To this end, FloppyTail protocol based on Rosetta frame was used in combination of unambiguous and ambiguous distance constraints. The unambiguous constraints were obtained from the PRE data. C445 of the PSG construct and W499C of the PDZ3-SH3 construct were labeled by MTSL, and the PRE rates were calculated as described in

Chapter 1.6.3. The distances are calculated using the SB-equation, and the error range is estimated as described in experimental procedure. The ambiguous distance constraints were obtained from the chemical shift perturbations on PDZ3, as shown in Fig. 3.1. These residues were constrained in such a way that they are set in vicinity of 7 Å to any one of solvent exposed nonPDZ3 residues.

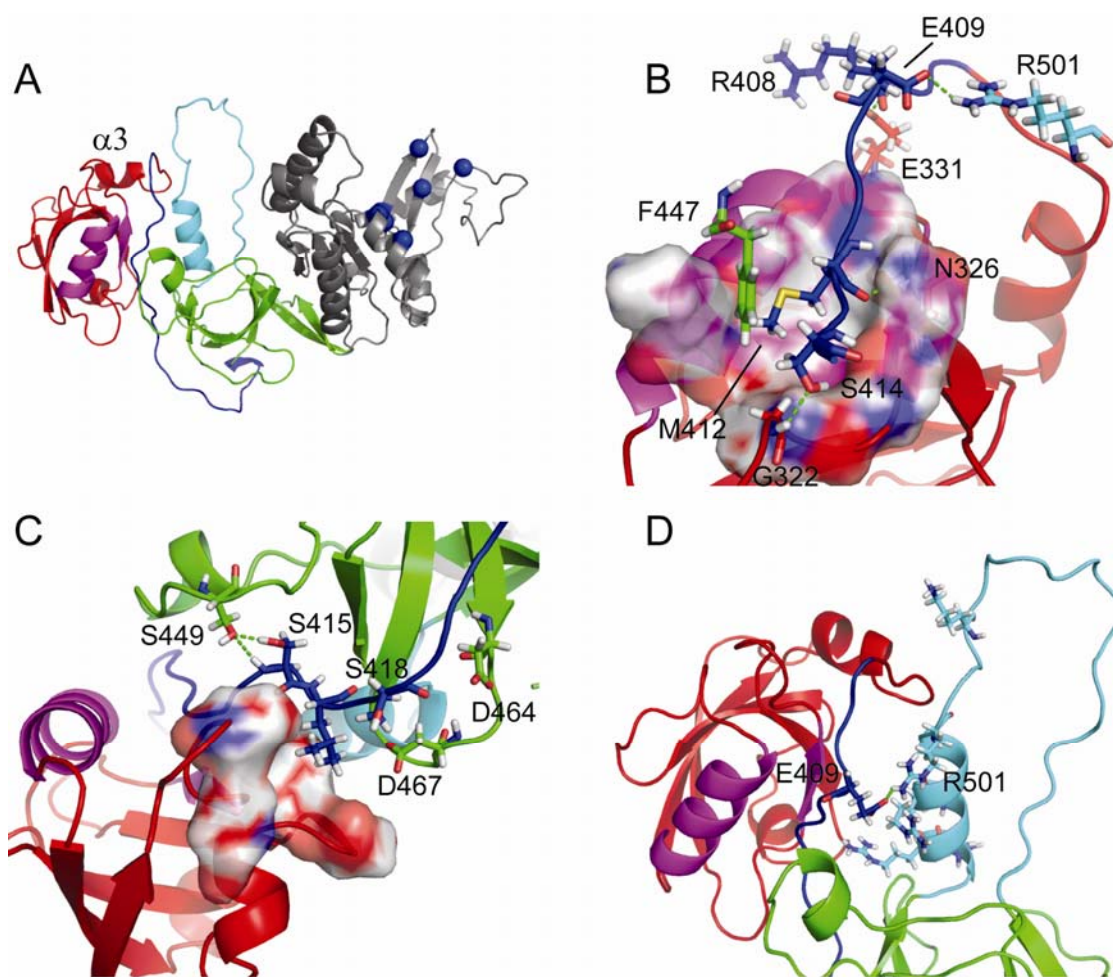


Figure 3.11: Rosetta modeling of PSG. (A) Overview of PDZ3-SH3-GK. PDZ3 is shown in red, the $\alpha 2$ and $\beta 2$, which constitute the peptide binding groove is shown in magentas, the PDZ3/SH3 linker in blue, SH3 in green, the Hook domain in cyan and GK in gray. The residues on MAP1A binding groove are shown in blue spheres. H-bonds are shown in green dotted lines. The following panels use the same color scheme. (B) Docking of the PDZ3/SH3 linker into the PDZ3 peptide binding groove. The PDZ3 peptide binding pocket is represented by surface. Sidechains of M412 and F447 are docked into the hydrophobic pocket of PDZ3. (C) Interactions S⁴¹⁵LGS⁴¹⁸ fragment with PDZ3 and SH3. S415 forms H-bonds with S449 of SH3, and L416 is packed to the hydrophobic of PDZ3 formed by L342, A343, T321 and P346. D464 and D467

around S418 are shown in green sticks. (D) Sequestration of the Hook domain. Basic residues on the Hook domain are shown in cyan sticks. A H-bond is formed between the linker residue E409 and the Hook domain residue R501.

Typically, 5,000 structures were calculated by FloppyTail, and the 20 best scored structures were analyzed. Fig. 3.11 shows a representative of PSG modeling results. The most interesting finding in this model is that the PDZ3 peptide binding groove is sealed by the PDZ3/SH3 linker. A highly conserved residue M412 is docked into the hydrophobic patch of PDZ3. Canonically, this hydrophobic patch accommodates the hydrophobic C-terminus of PDZ3 binding peptides. This hydrophobic pocket is further filled by the sidechain of F449. Similar to the canonical PDZ-peptide interaction, a network of H-bonds is weaved between S414-G322, M412-N326, E331-R408 and R501-E409. It is noteworthy that this internal peptide binding mode is short of the H-bonds formed between the C-terminus carboxyl group and the binding pocket. Therefore, the binding between PDZ3 and the PDZ3/SH3 linker is expected to be weaker than the canonical PDZ-peptide interactions. The binding of PDZ3 to the PDZ3/SH3 linker shortens the linker and therefore brings PDZ3 closer to SH3. More importantly, binding of CRIPT peptide expels the PDZ3/SH3 linker from the binding groove and consequently disrupts the domain association of PDZ3 with SH3/GK.

Another interesting finding in the PSG model is that the S⁴¹⁵LGS⁴¹⁸ fragment, which bears two *in vivo* phosphorylation sites S415 and S418, interacts with both PDZ3 and SH3. S415 forms H-bonds with S449, and L416 is docked to a hydrophobic of PDZ3 formed by L342, A343, T321 and P346. In the vicinity of S418, there are two negatively charged residues D464 and D467. In the previous chapter, we showed that phosphorylation of S415/S418 disrupted domain packing of PDZ3/SH3. It is possible that

when S415 and S418 are phosphorylated, the H-bond between S415 and S449 is broken and the phosphoryl group of phosphoS418 creates a repulsive force against the negative charge cluster of D464 and D467. All these perturbations destroy the interaction between SLGS linker and SH3, and consequently promote domain flexibility.

This model also suggests that the Hook domain is involved into PDZ3 and SH3 association. A hydrogen bond is form between E409 of the PDZ3/SH3 linker and R501 of the Hook domain. The calmodulin binding face of the Hook domain consists of positively charged residues. As shown in Fig. 3.11D, those residues are sequestered by PDZ3 and the PDZ3/SH3 linker.

3.4 Discussion

Biological functions of PSD-95 and other MAGUK proteins have been intensively studied for the last two decades. Overall, PSD-95 has been found to associate with numerous targets, performing diverse biological functions. One can imagine that more PSD-95 target proteins and functions will be identified. The extensive interaction and functional spectrum of PSD-95 is feasible considering that all component domains of PSD-95 are protein interacting modules. Thus, PSD-95 can fulfill its function as a scaffold by integrating multiple protein interacting domains into one amino acid chain. However, it is illusive how PSD-95, as a signaling organizer, ensures the binding events of different subdomains to take place in the proper context, which is usually required for the directionality of cellular signaling, and how PSD-95 ensures a signaling complex to contain the right combination of target molecules, which is required for fidelity of

cellular signaling. To answer these questions, insight into interdomain communication and allosteric regulation of PSD-95 is needed.

3.4.1 Interdomain contacts between PDZ3 and the Hook domain

Here, we integrate PDZ3 into our study of PSD-95, and find that PDZ3 forms a dynamic complex with SH3-GK. Chemical shift perturbation and PRE data suggest that the peptide binding groove of PDZ3 faces SH3. This orientation of PDZ3 relative to SH3-GK is changed by CRIPT peptide binding, as indicated by PRE. Our SAXS data suggest PDZ3 is mainly docked to the Hook region of SH3 domain. The Rosetta model also indicates that the PDZ3 masks the basic amino acids of Hook domain, which is a known calmodulin binding face. Moreover, CRIPT binding redistributes PDZ3 around the SH3 in a random pattern. These results hint at the complex allosteric mechanism between CRIPT binding of PDZ3 and Hook/calmodulin interaction[38]: Docking of PDZ3 around the Hook domain sequesters binding sites for calmodulin interaction or renders the Hook domain in a conformation unsuitable for calmodulin binding. Whereas binding of CRIPT releases PDZ3 from the SH3/Hook region, enabling the Hook domain to adapt a conformation for calmodulin interaction.

3.4.2 The Roles of the PDZ3/SH3 linker

The linker region of PDZ3/SH3 is conserved throughout different MAGUK proteins. In this research, we replaced two fragments of the linker region with Gly-Ser repeats, which are expected to lack stable structure. Our PRE data suggest that replacement of the linker region results in the disruption of PDZ3/SH3 domain orientation. This result is consistent with, and correlates to interdomain allostery of

PDZ3/SH3 in Dlg1 as reported[29]. The Rosetta simulation, though preliminary, further suggests that PDZ3 binds to its own internal linker sequence, which is akin to auto-inhibitory scenario. The hydrophobic residue (M412) at the linker region is docked to the hydrophobic patch within the PDZ3 peptide binding groove. According to sequence alignments, this residue is highly conserved, implying its significance in MAGUK family. The binding of the linker to the PDZ3 binding groove brings PDZ3 closer to SH3, whereas binding of CRIPT competes with the linker binding and moves PDZ3 away from SH3.

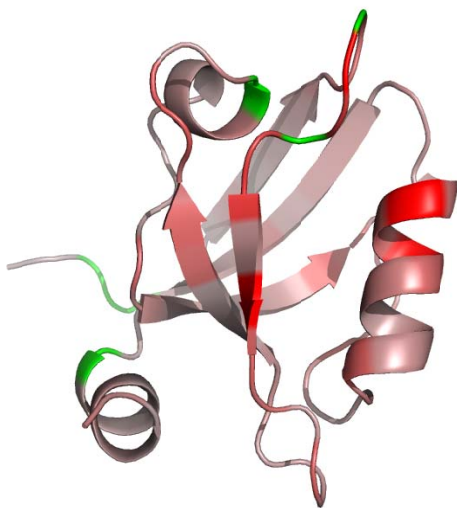


Figure 3.12: Paramagnetic perturbation on PDZ3^{S414C} by S414C MTLS labeling. The magnitude of proton transverse PRE is shown by color gradient of gray (small) to red (large). The residues whose PRE data are unavailable are shown in green.

Our study on PDZ3³⁰⁴⁻⁴¹⁴ (construct of PDZ3 and first half of the linker) also confirms the binding of the PDZ3/SH3 linker to PDZ3 peptide binding groove. The C-terminus of PDZ3⁴¹⁴ was labeled by MTSL and residues along the PDZ3 peptide binding groove were bleached (Fig. 3.12), suggesting the C-terminus is close to PDZ3 peptide

binding groove. It is noteworthy that the binding of the PDZ3/SH3 linker to the PDZ3 binding groove is different from canonical PDZ-peptide interaction. In canonical PDZ-peptide interaction, both hydrophobic contact and extensive H-bonding interactions are present. From the complex structure of PDZ3 and CRIPT (Fig. 1.1), 9 H-bonds are found. However, the interaction between C-terminus PDZ3/SH3 linker and PDZ3 is mainly mediated by hydrophobic packing and 4 hydrogen bonds. This may explain why a dynamic ensemble, instead of static and stable association of PDZ3 with SH3-GK is obtained.

According to the Rosetta modeling results, the linker region is further rigidified by interaction of S⁴¹⁵LGS⁴¹⁸ with PDZ3 and SH3. This interaction is mediated by hydrophobic packing of L416 with PDZ3 and hydrogen bond between S415 and S449 (Fig. 3.11C). Around these two residues, negatively charged residues, D464, D467 are found. Phosphorylation of these residues incurs electronic repulsion and breaks the H-bond, which is consistent with the increased domain flexibility suggested in the previous chapter.

3.4.3 Allostery of PDZ3/GK and putative function of Hook domain

Based on our PSG models built by SAXS and PRE data, PDZ3 is far away from the MAP1A binding groove located in the GK domain. Although the mechanism by which PDZ3/GK allostery is carried out is still elusive, our data provide a hint at this long distance interdomain allostery. We speculate that the Hook domain is a putative candidate to transfer the interdomain communication between PDZ3 and GK. A tryptophan at the Hook domain (W507) experiences strong paramagnetic perturbation

when C445, Y604C or S696C were labeled by MTSL. C445 is near to the PDZ3 docking site, while Y604 is at the MAP1A binding groove. These results indicate Hook domain is sampling various conformations spreading from MAP1A binding site to the PDZ3 docking site. Moreover, the strong PRE on W499 suggests that to create the paramagnetic perturbation, the lid domain of GK also has to adjust its conformation. It is known that binding of MAP1A requires the large scale transition of GK lid domain from open to close conformation. This conformational transition could be synchronized with Hook motions. A recent study suggested that mutations in the Hook domain and hinge of Hook domain results in a continuous activation of GK[44]. This study indicates the presence of an allosteric pathway between SH3 and GK. As suggested by research herein, the conformation of the Hook domain could be modulated by PDZ3. It is reasonable to speculate that allosteric information can be transferred to GK from PDZ3 via the Hook domain. From an evolutionary perspective, the sequence divergence of four PSD-MAGUKs, i.e. PSD-95, SAP97, SAP102 and PSD-93 in neuron cells mainly occur within the Hook domain. Except for this sequence difference, binding specificities of PSD-MAGUKs identified by excised domains are very similar. It is possible that the Hook domain is a key component to differentiate PSD-MAGUKs. The putative regulatory role of the Hook domain may therefore endow different members of MAGUK family with different outcomes.

3.5 Acknowledgements

We thank Rafael Garcia-Mata (Cell & Developmental Biology, UNC-CH) for providing the PSD-95 plasmid. We thank Greg Young (UNC Biomolecular NMR

Laboratory), Karl Koshlap (UNC Eshelman School of Pharmacy, NMR facility) and Ashutosh Tripathy (UNC Macromolecular Interactions Facility) for technical assistance. We thank Finith Jernigan and Qunzhao Wang in David Lawrence lab (UNC Chemistry Department) for peptide synthesis. We thank Xiaobing Zuo (Advanced Photon Source) for technique support in SAXS data collection. We thank Nicholas Anthis and Nicholas Fawzi in G. Marius Clore lab (NIDDK, National Institutes of Health) for useful advice in PRE, Lewis Kay for sending PRE pulse sequence.

Chapter 4

Crystallographic and NMR evaluation of the impact of peptide binding to the second PDZ domain of PTP1E

4.1 Introduction

The PDZ (PSD95/Discs large/ZO-1) domain family is one of the most abundant protein interacting modules found from bacteria to humans, with over 200 PDZ domains encoded in the human genome [5-7]. While they influence diverse functions in the cell, they are typically involved in targeting and assembly of multiprotein signaling complexes at synapses or other membrane proximal loci. PDZ domains fulfill this function through their facility in binding C-termini sequences (4-7 amino acids) of target proteins. They are often found in tandem arrays within a PDZ-containing protein, consistent with their role as scaffolds for association with membrane receptors, enzymes and ion channels [6]. They share a common fold, consisting of 2 α -helices and 6 β -strands, with the second α -helix ($\alpha 2$) and second β -strand ($\beta 2$) forming the canonical peptide binding groove [13].

In addition to scaffolding, numerous studies indicate that PDZ domains can have more direct regulatory functions. In particular, a subset of PDZs has now been characterized as displaying allostery [14, 63, 95, 96, 134, 135]. This is exemplified by the PDZ domain from Par6, which, upon binding CDC42 to the adjacent semi-CRIB motif

contacting the PDZ at an interface away from the peptide binding groove, undergoes a conformational change at the binding groove [14]. There is also recent evidence for interdomain allostery with PDZs [29, 135, 136]. Thus, while all PDZs have the capacity to serve as “passive” scaffolds, at least a subset appear to possess higher-order functional roles [137]. A central question in the PDZ field is, what distinguishes allosteric PDZs from simple scaffold PDZs, and to what degree are allosteric properties conserved? Further, although only some PDZs have “active” functions, are some properties related to these functions found in all PDZs because they either derive from a common descendent or those properties are intrinsic to the PDZ fold? Interestingly, although many PDZ structures have been determined in the absence and presence of ligands, observations of large conformational changes in PDZ domains have been rare [119]. Thus, much of the exploration of potential allosteric effects in PDZs has focused on more subtle origins than gross conformational change (see below).

As a result of such questions, during the last decade PDZ domains have been selected for biophysical study of their internal signaling properties. In 1999, Ranganathan and coworkers used sequence co variation analysis to reveal an evolutionarily conserved energy transmission pathway that connected to a key residue in the peptide binding site [138]. Specific PDZ domains were subsequently tested for intramolecular energy propagation using perturbation-response approaches [2, 3, 139], and analogous computational methods were developed that revealed PDZ-specific communication pathways [140-144]. These studies demonstrated that perturbation at localized positions in PDZ domains cause changes in dynamic fluctuations that propagate to more distal regions of the domain. They also have typically focused on two specific PDZ domains:

PDZ3 from postsynaptic density-95 (PSD-95), and PDZ2 from the protein tyrosine phosphatase PTP1E/PTPL1. Hence, “PDZ3” and “PDZ2” have emerged as the preferred PDZ domains for biophysical studies. Because of their representative status, gaining complete structural, dynamic, and biochemical information on these systems is highly desirable for fundamental understanding of PDZ domain function.

Historically, long-range effects (e.g. allostery) have been associated with conformational change. Thus, to understand how certain PDZ domains carry out their active functions, it is necessary to evaluate both structural and dynamic features of these systems. The archetypal PDZ domain is the third PDZ domain (“PDZ3”) from PSD-95. Early structural studies demonstrated a lack of significant structural change upon binding C-terminal peptide ligand [9]. Recently, Petit et al. showed that PDZ3 is indeed allosteric and that the mechanism of allostery is not structural, but resides in the conformational entropy of side-chain dynamics [63, 145]. In the case of PDZ2 (second PDZ from PTP1E/PTPL1, human form), the issue of structural change upon ligand binding is less clear. Several NMR structures have been reported for PDZ2. Human PDZ2 was reported for the apo state [146] and bound to RA-GEF2 peptide [147]. Although the backbone RMSD (using mean structures) between these two structures is 1.3 Å, with some subtle shifting of $\alpha 2$ upon peptide binding, clear conformational changes were not mentioned [147]. Mouse PDZ2, which differs by 6 amino acid substitutions (mostly in loops), was reported for the apo state [148] and bound to the APC peptide [139]. Subtle but significant structural changes were found upon APC binding, with a change in the tilt of $\alpha 2$ of 10° [139]. One complication in interpreting these NMR structures is that the free mouse and human do not agree very well and there appear to be some statistical problems

with human PDZ2, as pointed out [148]. In addition, none of these structures agree well with residual dipolar coupling (RDC) measurements reported here. Thus, at least for human PDZ2 binding the RA-GEF2 peptide, the question of conformational change has remained unresolved. As a result, in our previous study of side-chain dynamics in PDZ2 we concluded that a substantial role of structural changes in dynamic propagation could not be excluded [2].

In addition to the role of dynamics in intramolecular signaling in PDZ domains, dynamics has also been proposed to be important for PDZ domains' binding promiscuity and specificity [149-152]. Specific PDZ domains can bind to different classes of peptide ligands, and conversely, different PDZs are known in some cases to bind the same ligand [153]. Still unknown is how specific PDZ domains achieve the optimal balance between promiscuity and specificity, an issue also important for PDZ targeted drug design [154, 155]. The origin of PDZ binding promiscuity is an active area of research.

Because of the popularity of PDZ2 for structure-based biophysical studies of folding [156-160], binding [135, 139, 151, 159], and energy transmission [2, 3, 142, 143, 161, 162], the lack of reliable structural models for free and peptide-bound PDZ2 has compromised the interpretations of these studies and threatens to discourage future work on this model system. Without good structural information, it is impossible to weigh the balance of structure and dynamics in PDZ2, and, by extension, in PDZ domains. Here, we have determined the structural coordinates of apo and RA-GEF2 bound human PDZ2 using X-ray crystallography to resolutions of 1.65 and 1.3 Å, respectively. The coordinates were found to be consistent with solution NMR RDC measurements, thus indicating that the structures also represent (time-averaged) PDZ2 faithfully in solution.

Overall, changes in PDZ2 structure upon binding RA-GEF2 peptide are very small with RMSD of 0.3 Å. In addition, to test the robustness of our previous finding of propagation of dynamic changes in PDZ2 and to gain insight into binding specificity, we also characterized dynamic propagation upon binding a C-terminal peptide from APC, using ^2H methyl relaxation. These results show that both RA-GEF2 and APC peptide binding induce highly similar long-range perturbative effects to ps-ns side-chain dynamics, and this propagation is not driven by structural changes. Finally, to gain insight into the mechanism of peptide binding, both RA-GEF2 and APC peptides were investigated for their binding kinetics at the site-specific level using NMR relaxation dispersion methods.

4.2 Experimental Procedures

4.2.1 Protein expression and purification.

The second PDZ domain (1361-1456) from human PTP1E/PTPL1 was sub-cloned into pET21 vector as described [2]. Protein was overexpressed in the BL21 (DE3) cell line in LB or M9 minimal media. Cells transformed with PDZ2 vector were induced with 1 mM IPTG and grown at either 22 or 37 °C overnight for protein expression. PDZ2 was purified using the same procedure as reported [2] and verified by mass spectroscopy. For crystallization, protein was exchanged into buffer containing 50 mM NaCl and 20 mM Tris-HCl pH 6.8. For NMR study, protein was dissolved in 150 mM NaCl and 50 mM sodium phosphate pH 6.8, and 10% D₂O. To prepare isotope-labeled samples for NMR, isotopically enriched chemicals ($^{15}\text{NH}_4\text{Cl}$, U- $^{13}\text{C}_6$ (99%) D-glucose, and D₂O) were used in the minimal media.

4.2.2 Peptide preparation.

RA-GEF2 peptide (Ac-ENEQVSAV) was a product of GenScript (Piscataway, NJ). The peptide concentrations were determined by PULCON [163, 164]. APC peptide (GSYLVTSTV) was chemically synthesized with F-MOC modified amino acids using solid phase methods [165]. The peptide product was purified by HPLC using a reversed-phase C18 column and acetonitrile gradient. The identity and purity of the resultant peptide was checked by mass spectrometry. The APC peptide stock concentration was determined by UV absorbance with an extinction coefficient of $1490 \text{ cm}^{-1}\text{M}^{-1}$ at 280 nm.

4.2.3 Crystallization.

The apo and RA-GEF2 bound PDZ2 crystals were obtained using the hanging drop diffusion method. Apo-PDZ2 was crystallized via mixing 1.5 μl of 60 mg/ml protein and 1.5 μl of well buffer containing 28% PEG 3350, 0.2 M KI, 0.2 M NaSCN, 0.1 M sodium acetic acid pH 4.5, and 5% 2-propanol at room temperature. RA-GEF2 bound PDZ2 co-crystals were obtained in 20% PEG 3350, 0.2 M NaSCN, 0.8 M $(\text{NH}_4)_2\text{SO}_4$ and 0.1 M sodium citrate pH 5.5 in the presence of 10 mM RA-GEF2 peptide at 4 °C. It should be noted that these crystallization solutions served as effective cryoprotectants. In the case of the complex, incomplete mixing of PEG and $(\text{NH}_4)_2\text{SO}_4$ likely led to high local concentrations of PEG. Therefore, the crystals of free and peptide-bound PDZ2 were directly flash-frozen using liquid nitrogen for storage without additional cryo protection step.

4.2.4 Structure determination and refinement.

The apo and peptide bound PDZ2 domain crystal diffraction data were collected in beamline X29A of the National Synchrotron Light Source at Brookhaven National Laboratory. Both data sets were collected with X-ray wavelength 1.0809 Å at 100 K (Table 4.1). Space groups were determined using xtriage [166]. The integrated and scaled data by HKL2000 [167] were applied to AMoRe integrated in the CCP4 package for molecular replacement [168]. To build the initial apo structural model, PDZ2 from SAP97 [169] (PDB ID: 2AWX) was used as a search model. The apo structure was processed further with alternating rounds of refinement by REFMAC [170] and phenix.refine [171] and manual model building by Coot [172]. TLS refinement with

Table 4.1: Data collection statistics

	Apo PDZ2 ^a	RA-GEF2 PDZ2 ^a
Wavelength (Å)	1.0809	1.0809
Resolution Range (Å)	50-1.65	50-1.3
no. of reflections	1216653	460997
no. of unique reflections	74902	34689
Completeness (%)	98.6 (73.6) ^a	99.1 (97.7)
Space group	P2 ₁ 2 ₁ 2 ₁	H32
Cell parameters (Å)	63.023 95.148 101.989	73.965 73.965 134.056
Cell angles (deg)	90 90 90	90 90 120
Average redundancy	16.2 (10.8)	13.3 (10.7)
R _{merge} (%)	11.4 (85.6) ^b	5.6 (18.0)
<I/σ>	19.232	47.456

^a The values in parentheses are for the highest resolution shell.

^b $R_{\text{merge}} = \sum_h \sum_i |I_i(h) - \langle I(h) \rangle| / \sum_h \sum_i I_i(h)$, where $I_i(h)$ is the intensity of an individual measurement of the reflection and $\langle I(h) \rangle$ is the mean intensity of the reflection.

phenix was applied with TLS parameters from the TLSMD server [173]. Densities for the iodine ions, which were added during the crystallization process, were characterized utilizing Bijvoet difference maps. For the peptide-bound structure model, the apo PDZ structure was utilized as a search model for molecular replacement, but without peptide coordinates to rule out phase bias. Peptide electron density was clearly visible after the first cycle of refinement and then filled with peptide model. The peptide-bound structure

was also processed with alternating rounds of refinement by REFMAC [170] and phenix.refine [171] and manual model building by Coot [172]. During refinement with phenix.refine, the individual anisotropic ADP refinement option was utilized. Both structures have weak additional electron densities occupying the non-protein space that are modeled with water molecules.

4.2.5 NMR spectroscopy.

All NMR experiments were carried out at 25 °C (calibrated using methanol) on 500 and/or 600 MHz Varian Inova spectrometers. The protein concentration used was 1 mM. To prepare peptide saturated protein samples, RA-GEF2 or APC peptide was added to a peptide: protein ratio of 1.8:1. Protein concentrations were determined by UV absorbance with $\epsilon_{280}=1490 \text{ cm}^{-1}\text{M}^{-1}$. All NMR spectra were initially processed by NMRPipe [174] and subsequently applied to NMRView [175] or in-house programs lab for further analysis.

4.2.6 RDC data collection and analysis.

Using the IPAP-HSQC experiment [176], ^{15}N - ^1H RDC data were collected for isotropic and anisotropic samples on a 500-MHz magnet. Proteins were aligned by axial stretching of a 6-mm polyacrylamide gel (6%) into a 5-mm NMR tube (New Era Enterprises, Inc., Vineland, NJ) [177]. The residual dipolar couplings were extracted using the RDC module of NMRPipe. Q-factors of RDC data were calculated by REDCAT [178]. The residues in flexible loops, termini together with overlapping resonances were excluded in RDC data analysis.

4.2.7 Binding affinities and populations.

The binding affinity between the RA-GEF2 peptide and PDZ2 was determined by fluorescence and further confirmed by NMR titration. The two methods produced the same K_d of 10 μ M. The APC-PDZ2 binding affinity was also measured by NMR titration, yielding a K_d of 10 μ M (Fig. S4.3). With K_d , total peptide concentration $[S_T]$, and total protein concentration $[P_T]$ known, the populations of peptide-bound $[P_B]$ and unbound PDZ2 $[P_A]$ can be calculated as:

$$[P_B] = \{(K_D + [S_T] + [P_T]) - [(K_D + [S_T] + [P_T])^2 - 4[S_T][P_T]]^{1/2}\} / 2 \quad (\text{eq. 1})$$

, and

$$[P_A] = 1 - [P_B]. \quad (\text{eq. 2})$$

4.2.8 ^{15}N Relaxation dispersion.

^{15}N Carr-Purcell-Meiboom-Gill (CPMG) relaxation dispersion experiments were carried out using compensated CPMG pulse sequence [179]. For all PDZ-peptide complexes, time delays between consecutive 180° CPMG pulses were set as 0.556, 0.652, 0.75, 0.936, 1.25, 1.5, 1.875, 2.5, 3, 3.75, 5, 7.5, and 15 ms. The total relaxation time in CPMG train was 60 ms. The RA-GEF2 bound PDZ2 relaxation dispersion data were acquired at two sub-saturated states with peptide: protein molar ratios of 1:19.6 and 1:1.97, respectively. APC bound relaxation dispersion data were collected at a single

peptide: protein ratio of 1:19.6. The relaxation dispersion data were collected on 500 and 600 MHz spectrometers in an interleaved manner.

Relaxation dispersion curves were fitted both locally (residue-specific fits) and globally using the in-house program *exrate* [1]. For global fitting, a single exchange rate k_{ex} , a single $[P_A]$, and residue-dependent $\Delta\omega$ and R_{20} values were fitted using the general Carver-Richards expression [180]. For the sample with ~5% saturation, $[P_A]$ obtained from global fitting was 94.7%, in excellent agreement with 94.8% based on known K_d and concentrations. We found that fitted $\Delta\omega$ s agreed very well with the directly observed chemical shift differences between free and fully saturated PDZ2 ($\Delta\omega_{\text{titration}}$). For local fitting of individual residues, the $[P_A][P_B]$ product was set as a known constant (based on the global fit). In the local fits, the better of the two fits between use of the general or “fast” models was determined based on agreement of $\Delta\omega_{\text{CPMG}}$ with $\Delta\omega_{\text{titration}}$.

4.2.9 ps-ns dynamics.

Backbone and side-chain dynamics of APC-bound PDZ2 was studied in the same manner as for the RA-GEF2 complex reported previously [2]. Briefly, ^{15}N backbone relaxation experiments were used to collect ^{15}N T_1 , T_2 and $\{^1\text{H}\}$ - ^{15}N nuclear Overhauser enhancement (NOE) [56] at 500 MHz and 600 MHz. Methyl bearing side-chain dynamics was extracted from ^2H relaxation within CH_2D isotopomers. I_zC_z , $\text{I}_z\text{C}_z\text{D}_z$ and $\text{I}_z\text{C}_z\text{D}_y$ relaxation experiments were collected at 500 and 600 MHz and analyzed as described previously [2].

4.3 Results and Discussion

4.3.1 Crystal structures of apo and peptide-bound PDZ2.

In order to detect conformational changes resulting from peptide binding, crystallography was employed to determine structures of PDZ2 in the absence and presence of an 8-mer C-terminal peptide ligand from RA-GEF2 [147, 181]. Crystals in both forms diffracted X-rays to reasonably high resolution, 1.65 Å for apo PDZ2 and 1.3 Å for RA-GEF2 bound PDZ2, respectively. The final R-factors for apo and peptide-bound PDZ2 are 19.7% and 16.4% respectively (Table 4.2).

Table 4.2: Structure refinement statistics

	Apo PDZ2	RA-GEF2 PDZ2
Resolution Range (Å)	39.6-1.6	29.7-1.3
no. of reflections	133400	34191
R-factor (%) ^a	19.7	16.4
R-free (%) ^b	23.7	18.9
no. of non-H atoms	4167	1040
no. of water molecules	433	238
Ramachandran ^c		
In most favoured regions	98.0	98.3
In additional allowed regions	2.0	1.7
In disallowed regions	0.0	0.0

^a $R_{\text{cryst}} = \sum_h ||F_{\text{obs}}| - |F_{\text{calc}}|| / \sum_h |F_{\text{obs}}|$, where F_{obs} and F_{calc} are the observed and calculated structure-factor amplitudes, respectively.

^b R_{free} was calculated as R_{cryst} using approximately 5% of randomly selected unique reflections that were omitted from the structure refinement. Values in parentheses are for the highest resolution shell.

^c The Ramachandran analysis is performed using Molprobity.

Apo PDZ2 crystals belong to the $P2_12_12_1$ space group. In the asymmetric unit, six monomers are packed to form two layers of three-blade propeller like structures

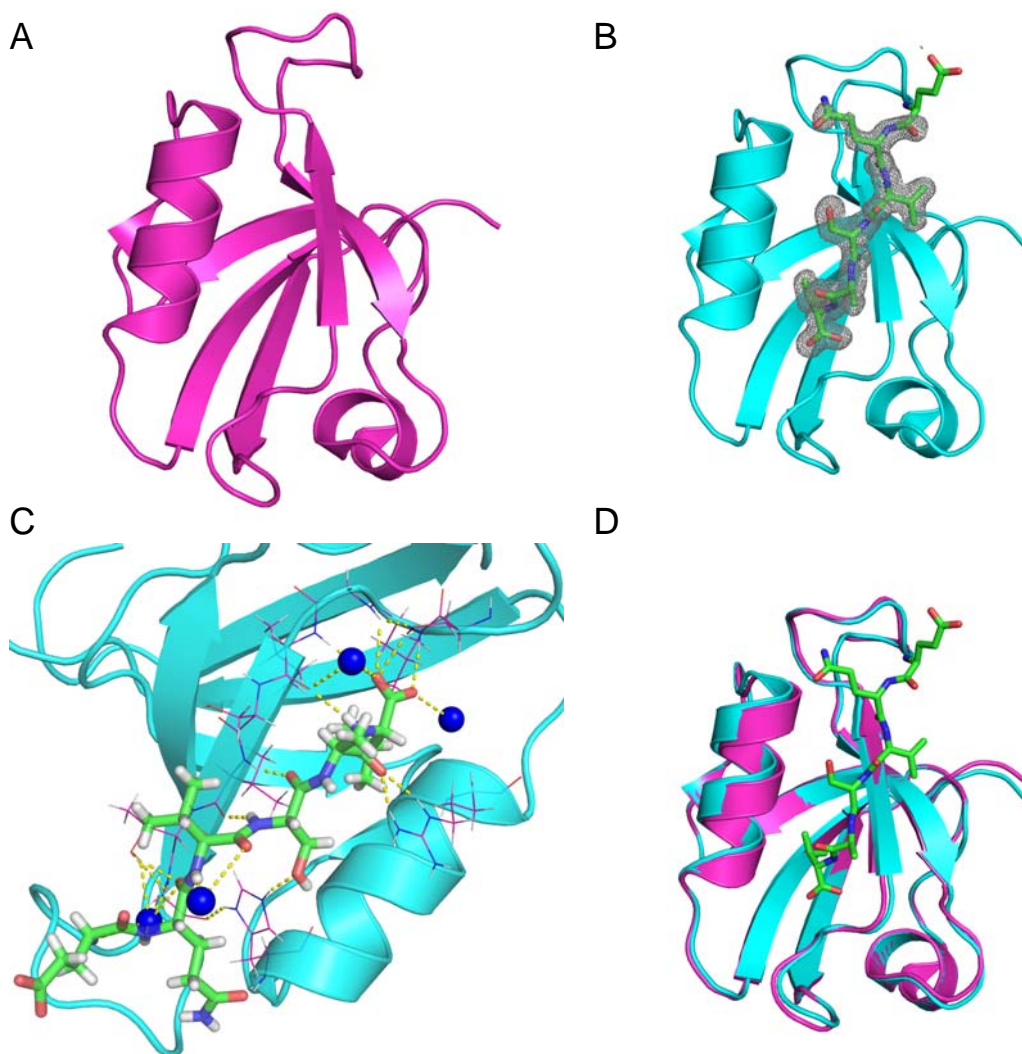


Figure 4.1: Cartoon representation of PDZ2 crystal structures. Apo (A) and RA-GEF2 bound (B) PDZ2 structures. Peptide is shown as stick model and electron density is shown as gray mesh. The density contour level is 1.5σ . Peptide residues QVSAV have visible electron density. (C) RA-GEF2 and PDZ2 interaction network. RA-GEF2 peptide is shown by stick model and surrounding PDZ2 residues involved in peptide interaction are shown as lines. Bound water molecules involved in PDZ2 peptide interaction are shown as blue balls. The hydrogen bonds relevant to peptide binding are shown by yellow dotted lines. (D) Structural Superposition of apo (magenta) and RA-GEF2 bound PDZ2 (cyan). The RA-GEF2 peptide is shown by green stick model. All structural graphics were prepared using PyMOL.

(Fig. S4.1A and S4.1B). The average pair-wise C^α RMSD of the monomers is 0.18 Å, indicating all monomers are essentially identical. As expected, the crystal structure solved here conforms to the canonical PDZ domain fold, comprising 6 β-strands and 2 α-helices (Fig. 4.1A). The second β-strand (β2) and the second α-helix (α2) constitute the peptide binding groove. The RA-GEF2:PDZ2 complex crystals belong to space group R32 (H32). One molecule appears in each asymmetric unit. A hexamer conformation (32 symmetry), generated by crystallographic symmetry, is identical to the hexamer structure in the apo form. Based on calculation of the buried surface area in the hexamer interface by PISA [182], this PDZ domain molecule is expected to exist as a hexamer in solution; however, there is no evidence of this from NMR relaxation [2], which is sensitive to the rate of molecular tumbling, nor are higher-order oligomeric species evident from size exclusion chromatography. In the peptide-bound PDZ2 structure (Fig. 4.1B), hydrogen atoms were also modeled. In the RA-GEF2 peptide, the five C-terminal residues (QVSAV) show electron density. Using PDZ ligand numbering, counting backwards from the C-terminus, these are residues (0) to (-4). The RA-GEF2 peptide fitted into the binding groove forms an anti-parallel β-strand with protein strand β2. The interaction is further strengthened by packing of the most C-terminal valine side chain with the surrounding hydrophobic patch. The interaction is also stabilized by hydrogen bonding between Ser(-2) and the conserved H71 sidechain, as well as between the backbone of Ala(-1) and R79. In the apo state, the side chain of R79 adopts different conformations in the six different monomers. Upon binding peptide, this apparent flexibility is lost by hydrogen bonding to the carbonyl of Ala(-1). Consistent with previous studies, RA-GEF2 residues back to (-4) are hydrogen bonded with the protein (Fig. 4.1C) [146]. In

establishing this intricate hydrogen bonding network, several bound water molecules are also involved (Fig. 4.1C).

All atoms of apo and bound structures have very distinct electron densities, except side-chain atoms of loop residues S29-G33 and terminal residues Q93 and S94.

Intriguingly, an irregular 3_{10} -helix is identified for residue fragment 30-33 (VRHGG), which is usually characterized as a partially structured loop in NMR structures or other PDZ2 homologues. Compared to the average temperature factor of the free protein (38 \AA^2), high temperature factors (68 \AA^2 on average) are observed for this fragment, suggesting high flexibility. Even though B-factors are high, the backbone traces are very similar for all PDZ molecules. This fragment is also involved in crystal packing for both apo and peptide-bound PDZ2, as revealed by crystal lattice packing (Fig. S4.2). It is thus possible that the 3_{10} -helix of residues 30-34 is stabilized in part by the crystal lattice. Nevertheless, in PDZ domains from HtrA proteases, non-canonical helices have been observed in the intervening residues between $\beta 2$ and $\beta 3$ [183]. Furthermore, $^{13}\text{C}^\alpha$ chemical shifts are consistent with some degree of helicity in solution for residues 31-33 (in both free and RA-GEF2 bound states), with an average (positive) deviation from random coil values of $1.6 \pm 0.4 \text{ ppm}$.

These high-resolution structures enable a new assessment of ligand induced conformational changes in PDZ2. As shown in Fig. 4.1D, no substantial conformational changes are observed: the C^α RMSD of apo and peptide-bound structures is 0.29 \AA (0.21 \AA if loop residues 26-32 are excluded). This is reminiscent of peptide binding to PDZ3 of PSD95, for which no structural change was found [9], but distinct from the previously published NMR model of APC-bound mouse PDZ2, for which a 10° rotation of $\alpha 2$ was

Table 4.3: RMSDs of published PTP1E PDZ2 structures and crystal structures						
RMSD (Å)	^b 3LNX	3PDZ	^a 1GM1	^b 3LNY ^{RA-} _{GEF2}	1D5G ^{RA-} _{GEF2}	^a 1VJ6 ^{APC}
^b 3LNX	-	1.78 ^c	0.85	0.29		
3PDZ	1.99	-	1.90		2.09	
^a 1GM1	0.98	2.28	-			1.39
^b 3LNY ^{RA-GEF2}	0.30			-	1.32	1.21
1D5G ^{RA-GEF2}		2.28		1.83	-	1.60
^a 1VJ6 ^{APC}			1.69	1.54	2.05	-

^a Mouse PTP PDZ2, which has 92% sequence identity to human PDZ2.
^b Crystal structures solved in this research.
^c The RMSD values above diagonal were calculated based on C α structure alignments; values below the diagonal were calculated based on all heavy atoms..

reported [139]. The differences between the crystal structures and previously published PTP1E PDZ2 NMR structures are compared quantitatively in Table 4.3. The RMSDs between crystal and NMR structures range from 0.9 – 2.0 Å. Upon superposition of the apo and bound crystal structures here (excluding $\alpha 2$), RA-GEF2 binding induces a reorientation of $\alpha 2$ of only 2.8°. Thus, based on RMSDs, our crystal structures appear very similar to each other, yet show significant differences from the other PDZ structures. Significant discrepancies are also found among the NMR structures (Table 4.3), which are either human or mouse forms, even though human PDZ2 (3PDZ and 1D5G) [146, 148] differs from mouse homologue (1GM1 and 1VJ6) [139, 147] by only 6 residues (including 2 conservative mutations). One possible source for these discrepancies is the different methodologies in structure determination. Despite the apparent high resolution, the crystal structures may be influenced by crystal packing effects that introduce structural artifacts and conformational trapping [184, 185]. Similarly, the NMR structures may suffer from inadequate NOE's to fully define the structure in all regions. Thus a question arises: Are the crystal structures solved here good models for PDZ2 in solution?

This prompted us to employ a solution-based approach, residual dipolar couplings (RDC), to further assess the crystal structures.

4.3.2 Structure validation through solution RDCs.

Residual dipolar couplings (RDCs) provide orientation information on internuclear vectors in biomolecules and are widely used in NMR structure calculations and domain-domain docking [186]. Alternatively, solution RDCs can be used as a powerful tool to assess the quality of structural models generated without RDC information, which includes, for example, crystal structures. Similar to the R-factor in crystallography, a quality metric called the Q-factor is calculated by fitting experimental RDC data to a structural model [187]. The Q-factor varies between 0 and 1, with low Q values indicating high consistency between RDCs and the model, and high values indicating low consistency. Thus, high Q values (> 0.3 - 0.4) are generally suggestive of low structural quality, assuming that there are no problems/artifacts in the RDCs. Due to intrinsic errors in RDC data collection, the lower limit for Q-factors in practice is around 0.1 [188].

To evaluate all deposited PDZ2 structures (none of which used RDCs in refinement), amide ^1H - ^{15}N RDC data were collected for PDZ2 in apo, RA-GEF2 bound, and APC bound states. The crystal structures of apo and RA-GEF2 bound forms fitted to their respective RDCs yield low Q values of 0.22 and 0.21 respectively (Table 4.4). This good agreement suggests that the crystalline PDZ2 structures are not significantly affected by crystal packing and conformational trapping. By contrast, the NMR structures generate significantly higher Q values (from 0.39 to 0.82, Table 4.4). We note that many of the RDCs were also collected using lipid bicelles, and the Q-factors were very similar

Table 4.4: Q-factors calculated by fitting RDC data to structural models						
RDC data ^b	Structure ^a					
	3LNX	3PDZ	1GM1	3LNY ^{RA-GEF2}	1D5G ^{RA-GEF2}	1VJ6 ^{APC}
Apo PDZ	0.22	0.82(0.82)	0.39(0.56)	0.29	-	-
PDZ2 ^{RA-GEF2}	0.26	-	-	0.21	0.67(0.71)	0.56(0.58)
PDZ2 ^{APC}	0.20	-	-	0.23	0.81(0.77)	0.69(0.75)

^a The apo and RA-GEF2 bound PDZ2 structures solved here are 3LNX and 3LNY. For NMR structures, Q-factors were obtained by fitting against the best representative structure of the ensemble. Alternatively, RDCs were fit to bond vector orientations that represent averaging over the NMR ensemble (values in parentheses). All Q-factors were calculated using REDCAT.

^b Overlapping resonances were excluded in data fitting. To make Q-factors comparable, the same set of residues from each set of RDC data were selected to fit individual structures. The residues included in the fits are given in Table S4.3, and mapped on the RA-GEF2 bound crystal structure (Figure S4.4).

(data not shown). Overall, based on the computed Q-factors, the crystal structures reported here represent the average solution features of PDZ2 (apo or bound) significantly better than the existing NMR structures. We therefore expect that these crystal structures will provide more accurate coordinates for molecular dynamics simulation starting structures or structure-based studies of PDZ2.

In addition, the RDC analysis suggests that an overall lack of change in the time-averaged conformations of PDZ2 in response to peptide binding also holds true in solution. This is evident from the low Q-factors of 0.22 and 0.21 for apo and bound PDZ2 (Table 4.4). It is also evident upon considering that the apo PDZ2 RDCs are nearly as consistent with PDZ2^{RA-GEF2} structure as with apo PDZ2 (Q-factors of 0.29 versus 0.22). Conversely, the PDZ2^{RA-GEF2} RDCs are nearly as consistent with the apo structure as with the PDZ2^{RA-GEF2} structure (Q-factors of 0.26 versus 0.21). These relatively small differences in Q-factors (0.05, 0.07) are suggestive of subtle structural and/or dynamic differences that exist between free and RA-GEF2 bound forms, although a significant

portion of the differences may be due to experimental uncertainty in the RDCs. It is interesting to note that RDCs from the APC-PDZ2 complex fit slightly better to apo-PDZ2 than the RA-GEF2 bound structure (Table 4.4). We note that the Q-factor fitting included RDCs from $\alpha 2$ and $\beta 2$ (Fig. S4.4), which form critical hydrogen bonds with peptide and should report on any structural change. The RDC data here appear to contradict a previous report of a 10° change in $\alpha 2$ orientation, in solution, upon binding the APC peptide [139]. However, that was carried out on mouse PDZ2, and it remains possible that mouse and human PDZ2s differ in this respect. We also note that there may be dynamic aspects to $\alpha 2$ in human PDZ2, as suggested from a slightly increased ^{15}N R_2 at R79 relative to the other structured regions (in the apo form, data not shown). We speculate that $\alpha 2$ may undergo segmental motion on the ns- μs timescale. In summary, the RDC data are highly consistent with the crystal structures and show that neither RA-GEF2 nor APC peptides induce significant conformational changes to human PDZ2 in solution.

4.3.3 Long-range “pure” dynamic propagation in PDZ2 also results from APC peptide binding.

In our previous study of the RA-GEF2 peptide binding to PDZ2 [2], binding was observed to perturb ps-ns dynamics of methyl-bearing side chains not only at the binding site, but also at two surfaces of PDZ2 distal to the peptide binding pocket. At that time, it was unclear to what extent the dynamic propagation was due to changes in peptide-induced structural changes in PDZ2. The combined crystallographic and NMR results here strongly suggest that conformational change does not drive the dynamic changes and that PDZ2 channels the impact of peptide binding as a relatively “pure” dynamic

response to distal surfaces 1 and 2 [2]. The emerging picture appears to be that a network of residues extends through much of PDZ2. Atom fluctuations around mean positions of the network confer variable force patterns that can transmit perturbations over distances. We note that such behavior has recently been used as a perturbation-response tool in the context of molecular dynamics simulations [141, 142, 189, 190]. Thus, a major event such as peptide binding in the PDZ active site can alter fluctuation patterns well beyond the binding site without significant changes in mean structural positions. The patterns may in some cases manifest as correlated motions, as demonstrated recently for PDZ2 [162]. This qualitative model is consistent with the ease of dynamic perturbation by both mutation and ligand binding [191].

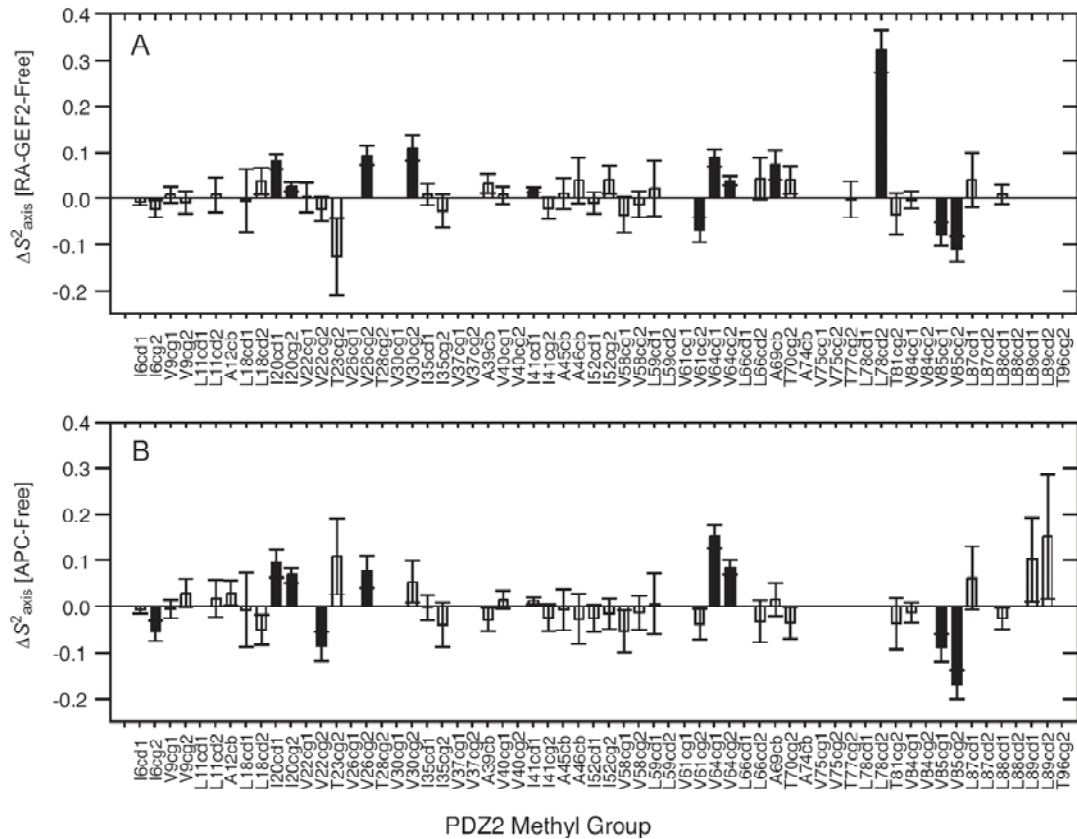


Figure 4.2: Methyl-bearing side-chain dynamics changes (ΔS^2_{axis}) induced by RA-GEF2 (A) and APC (B) binding, with respect to free PDZ2. The methyl groups with significant changes in S^2_{axis} ($\Delta S^2_{\text{axis}} > 2\sigma$) are shown in filled bars. Fig 4.2A was adapted from Fuentes et al. [2]

To further test this model and potentially increase confidence in the long-range dynamic propagation observed for RA-GEF2 binding, we characterized the methyl side-chain dynamics of PDZ2 bound to a C-terminal peptide derived from the APC protein [192] using ^2H relaxation. This peptide (GSYLVTSV) binds with $K_d \sim 10 \mu\text{M}$, similar to RA-GEF2 (Fig. S4.3). The changes in S^2_{axis} and τ_e upon APC peptide binding are very similar to those in RA-GEF2 (Fig. 4.2 for S^2_{axis} and Fig. S4.5 for τ_e). The patterns of changes in S^2_{axis} in PDZ2 upon binding either peptide are shown in Fig. 4.3. In the case of RA-GEF2 binding, propagation was previously observed out to “distal surfaces 1 and 2”, although distal surface 1 is less apparent in Fig. 4.3A because changes in τ_e are not shown.

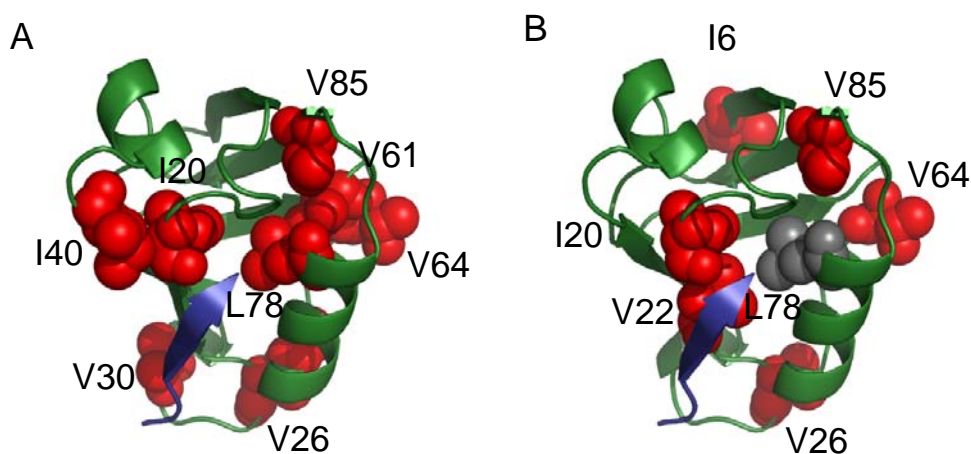


Figure 4.3: Graphical comparison of side-chain dynamic changes induced by RA-GEF2 (A) and APC binding (B). Red spheres represent residues experiencing significant ($\Delta S^2_{\text{axis}} > 2\sigma$) side-chain dynamic changes and peptide is shown as blue cartoon. The figures were prepared by PyMOL.

In the APC complex, only propagation to distal surface 1 is observed, but the pattern is near identical to that from RA-GEF2, both in terms of residues in the dynamic network and the magnitude of the dynamic response. One residue that shows a different response from the RA-GEF2 complex is at I6 at the N-terminal region of beta strand 1.

Construction of a 2-way contingency table based on the presence or absence of significant ΔS^2_{axis} values in specific methyl groups in both complexes resulted in a high level of pattern matching, with the Fisher's exact test p-value of 7.4×10^{-4} (Table 4.5).

Table 4.5: Contingency table showing a correlation between APC and RA-GEF2 induced ΔS^2_{axis}

APC	RA-GEF2		Total
	Significant	Insignificant	
Significant	7	2	9
Insignificant	4	25	29
Total	11	27	38

The p value based on Fisher's exact test is 0.00074.

This high degree of similarity in dynamic responses to RA-GEF2 and APC peptides demonstrates that the propagated dynamic responses are indeed real, reproducible, and more indicative of PDZ2 than ligand sequence (at least in these two cases). In addition, because the ^1H - ^{15}N RDCs measured for APC-bound PDZ2 agree equally well with the crystal structure of RA-GEF2/PDZ2 ($Q = 0.23$, Table 4.4), these data also support pure dynamic propagation. We suggest that these data represent one of the best examples of dynamic propagation – or dynamic signal transduction [193] – detected experimentally and site-specifically, in the absence of conformational changes [145, 194, 195].

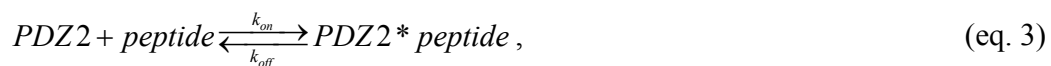
4.3.4 μs -ms timescale peptide binding dynamics.

A previous pre-steady state kinetic study of mouse PDZ2 binding to RA-GEF2 peptide showed that peptide association proceeds through an induced-fit mechanism [139]. These kinetic data suggested that PDZ2 undergoes a ligand induced conformational change with k_{obs} of $\sim 7000 \text{ s}^{-1}$. While the X-ray and RDC data presented above (on human PDZ2) do not support the existence of overall conformational change, it remains possible that conformational changes take place at low populations. To probe this possibility, we investigated μs -ms motions in PDZ2 using Carr-Purcell-Meiboom-Gill (CPMG) relaxation dispersion methods [180]. In principle, this strategy allows monitoring of the kinetics (k_{ex}) and structural effects (as interpreted through the difference in chemical shift between states, $\Delta\delta$) of conformational events at the residue level and can detect minor populations as low as 0.5-1% [196].

Microsecond-millisecond timescale dynamics are frequently associated with conformational change, enzyme catalysis, and protein folding [197]. ^{15}N CPMG relaxation dispersion experiments revealed that neither apo PDZ2 nor RA-GEF2 saturated PDZ2 exhibit significant μs -ms motion (data not shown). However, for binding interactions of moderate strength (\sim micromolar), ligand binding and dissociation can occur on this timescale and are amenable to characterization by relaxation dispersion using sub-saturated complexes [198-201]. More specifically, there is the potential for identification of dynamic events that occur during binding. Of interest here, non-two-state behavior was reported recently for peptide binding to the PDZ domain of AF-6, based on relaxation dispersion data [202]. To gain insight into the kinetics of binding and ligand specificity with site-specific resolution for PDZ2, ^{15}N CPMG relaxation dispersion experiments were carried out on both RA-GEF2 and APC peptide complexes with 5% or

50% molar amounts of peptide. The lack of μ s-ms exchange in the end states of the binding reaction is ideal for interpretation of line-broadening (i.e. relaxation dispersion) due to dynamic cycling of ligand binding and release.

To bring the peptide binding kinetics into an exchange window suitable for characterization by CPMG relaxation dispersion, PDZ2 protein was mixed with substoichiometric amounts of peptide. For dispersion curve analysis, we employed two-site exchange since the above structural studies indicated no evidence for conformational change. A two-site exchange binding process can be described by the following:



where k_{on} and k_{off} are the on-rate and off-rate of peptide binding, respectively. The exchange rate (k_{ex}) is modulated by the free peptide concentration based on the following expression:

$$k_{ex} = k_{on}[peptide] + k_{off} . \quad (\text{eq. 4})$$

Upon addition of 5% RA-GEF2 or APC peptide, relaxation dispersion was observed for residues along the binding groove and some distal regions. The high quality of the fits in Figure 4.4 is typical of the entire data sets for both peptide complexes. Local k_{ex} and $\Delta\omega$ were fit assuming a fixed p_A value of 0.95. Fits were carried out using the full Carver-Richards equation, as well as the simplified form for fast exchange [180], and we report the parameters which yielded better agreement with $\Delta\omega$ determined from titration.

Individually fitted exchange rates (k_{ex}), chemical shift changes ($\Delta\omega$) and intrinsic spin-

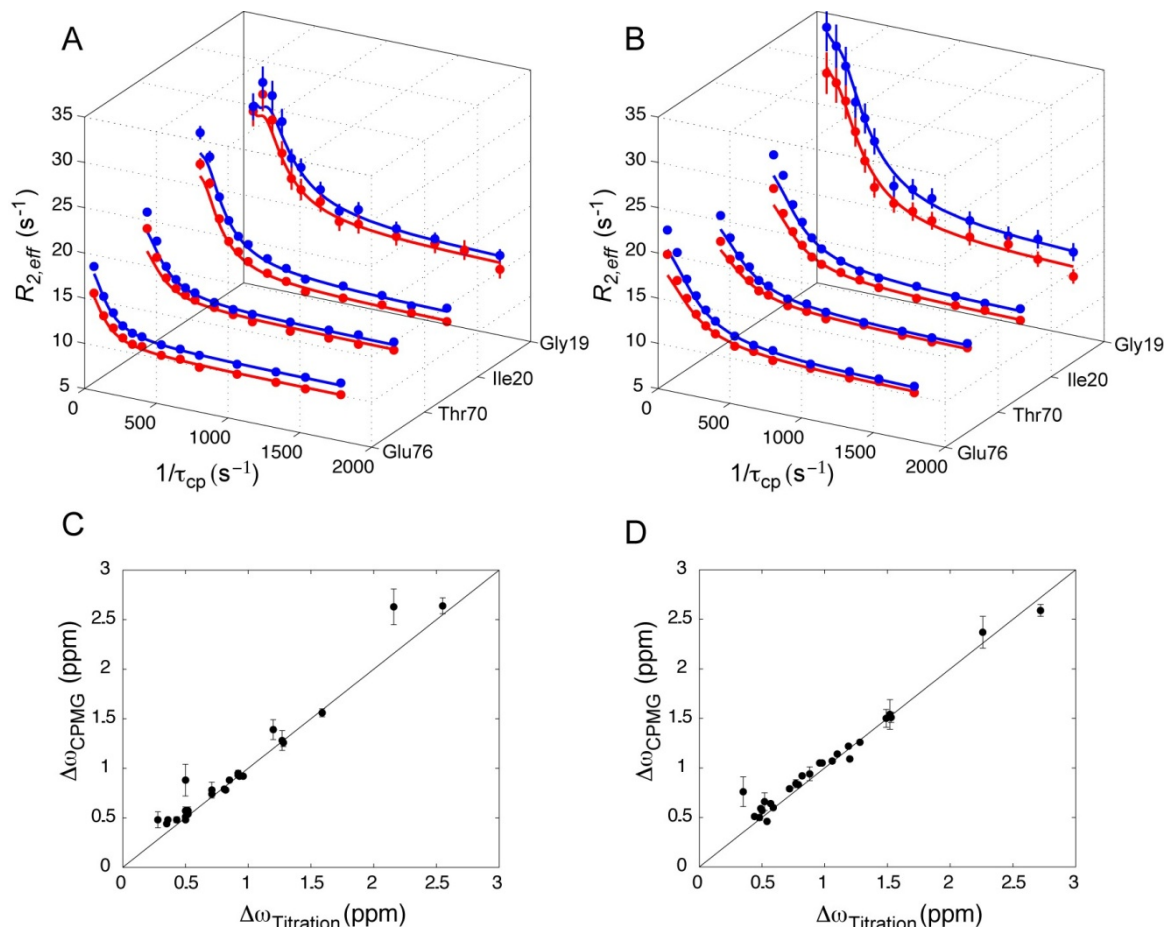


Figure 4.4: Two-state binding of RA-GEF2 and APC peptides based on ^{15}N relaxation dispersion. Relaxation dispersion curves for select resonances in PDZ2 5% saturated with RA-GEF2 (A) and APC (B) peptides. Data acquired at 500 and 600 MHz (^1H Larmor frequency) are shown in red and blue respectively. Data quality for these residues is typical of the entire dataset. In (C) and (D), correlation plots of fitted values from relaxation dispersion and ^{15}N values from peptide titration. CPMG values are from global fits, as described in the main text. Data for RA-GEF2 and APC are in (C) and (D) respectively. The line is $y = x$.

spin relaxation rates (R_{20}) for PDZ2 residues in complex with RA-GEF2 and APC are provided in Tables 4.6 and 4.7, respectively. The distribution of k_{ex} values were quite uniform, with average k_{ex} values of $408 \pm 127 \text{ s}^{-1}$ and $663 \pm 158 \text{ s}^{-1}$ for PDZ2 bound to 5% RA-GEF2 or 5% APC peptides, respectively. Given the similarity of the locally fitted exchange rates, the data for each complex were globally fit to a model in which all

residues share the same exchange rate and population, but $\Delta\omega$ and R_{20} are allowed to vary for each residue. The global fitting results are very similar to the local results (Table S4.1, S4.2). Importantly, globally fitted P_A values were determined to be 94.7% and 94.5% for RA-GEF2 and APC, respectively, in excellent agreement with the predicted fraction of free protein (95%) based on measured K_d values and reactant concentrations. In addition, fitted $\Delta\omega$ values ($\Delta\omega_{\text{CPMG}}$) for both peptides are remarkably consistent with the $\Delta\omega$ values based on peptide titrations ($\Delta\omega_{\text{titration}}$) (Fig. 4.4C and 4D). This strongly suggests PDZ2 samples two states (apo and fully bound) in the presence of peptide and these alone are responsible for dispersion. We note however, that there are a few resonances in each system for which we observe divergence between $\Delta\omega_{\text{CPMG}}$ and $\Delta\omega_{\text{titration}}$. In the case of the APC complex, all of these outliers have very small $\Delta\omega$ values. These discrepancies do not warrant further consideration since it is known that fitting relaxation dispersion with small chemical shift changes is error prone [203]. In the case of the RA-GEF2 complex, we find divergence for three residues with significant titration $\Delta\omega$ values: G19, S21, and G34. Interestingly, G19 and S21 exhibit the smallest values of k_{ex} (255 and 204 s⁻¹) in PDZ2. G19 and S21 are located at the binding pocket (in or near β_2), and G34 lies at the end of the β_2 - β_3 loop. Thus, although the majority of resonances in PDZ2 indicate simple two-state binding in the sensitivity regime for ¹⁵N CPMG relaxation dispersion, these few residues appear to hint at the existence of a RA-GEF2 binding intermediate localized to the vicinity of the peptide site. The behavior of G19, S21, and G34 is reminiscent of previously observed non-two-state behavior in ligand binding as observed from NMR relaxation dispersion [198, 200, 204]. The divergence from two-state behavior here

appears to be smaller than in those studies, yet larger than in the case of an SH3-ligand interaction [201]. Fits of the dispersion data to a 3-site exchange model was not carried out since this is advised only for when an abundance of dispersion curves is available [205].

Residue	k_{ex} (s ⁻¹)	$\Delta\omega_{\text{CPMG}}$ (ppm)	$^a R_{20}$ (s ⁻¹)	$^b R_{20}$ (s ⁻¹)	$^c \Delta\omega_{\text{titration}}$ (ppm)
17	385±40	0.93±0.02	9.96 ±0.09	10.46 ±0.10	0.92
19	255±22	2.63±0.18	12.80 ±0.38	13.44 ±0.31	2.16
20	357±21	1.56±0.04	10.39 ±0.14	11.37 ±0.13	1.59
21	204±28	1.39±0.10	10.59 ±0.14	11.36 ±0.12	1.20
22	478±369	0.48±0.08	14.69 ±0.26	14.41 ±0.22	0.28
23	438±87	0.48±0.02	10.76 ±0.09	11.70 ±0.09	0.50
24	336±98	0.57±0.04	12.49 ±0.19	12.67 ±0.18	0.50
27	446±168	1.28±0.10	17.09 ±0.52	19.95 ±0.57	1.27
31	432±154	0.78±0.08	19.42 ±0.45	20.70 ±0.38	0.71
34	926±465	0.88±0.16	14.64 ±0.42	17.68 ±0.58	0.50
35	480±48	0.95±0.03	12.72 ±0.14	13.88 ±0.16	0.92
40	358±43	0.51±0.02	9.59 ±0.07	10.04 ±0.07	0.50
45	440±39	0.74±0.02	10.43 ±0.10	11.11 ±0.10	0.71
66	482±82	0.48±0.03	10.85 ±0.08	11.49 ±0.09	0.43
67	348±29	0.54±0.01	9.83 ±0.05	10.53 ±0.05	0.52
70	434±29	0.92±0.02	11.17 ±0.10	11.67 ±0.10	0.93
71	386±67	0.48±0.02	12.94 ±0.10	13.38 ±0.09	0.36
72	319±33	1.26±0.04	10.90 ±0.13	11.19 ±0.12	1.28
74	448±20	0.92±0.01	10.07 ±0.07	10.65 ±0.07	0.96
75	412±19	0.79±0.01	10.53 ±0.05	10.98 ±0.06	0.81
76	326±32	0.88±0.02	10.06 ±0.08	11.10 ±0.08	0.85
79	285±10	2.64±0.08	11.19 ±0.16	11.84 ±0.15	2.55
80	407±27	0.78±0.02	9.43 ±0.08	9.85 ±0.09	0.82
81	445±44	0.48±0.02	7.79 ±0.05	7.83 ±0.05	0.36
82	394±109	0.57±0.04	14.01 ±0.17	13.67 ±0.16	0.52
86	384±73	0.44±0.02	10.73 ±0.07	11.30 ±0.08	0.35

^a Values at 500 MHz. ^b Values at 600 MHz. ^c ¹⁵N $\Delta\omega_{\text{titration}}$ values were calculated as the difference between apo and RA-GEF2 saturated PDZ2.

The primarily two-state relaxation dispersion behavior reported here contrasts with the CPMG-derived ligand binding dynamics in the AF-6 PDZ domain, which showed extensive discrepancies between $\Delta\omega_{\text{CPMG}}$ and $\Delta\omega_{\text{titration}}$ and hence is suggestive of an intermediate state during the binding process [202]. However, in the AF-6 PDZ, the apo

protein samples different conformations on the millisecond timescale, which complicates the interpretation of peptide binding dynamics. In the sub-saturated complexes of PDZ2,

Table 4.7: Local fitting results of 5% APC bound PDZ2 relaxation dispersion data

Residue	k_{ex} (s^{-1})	$\Delta\omega_{\text{CPMG}}$ (ppm)	$^a R_{20}$ (s^{-1})	$^b R_{20}$ (s^{-1})	$^c \Delta\omega_{\text{titration}}$ (ppm)
11	480 \pm 54	0.46 \pm 0.02	10.07 \pm 0.04	10.52 \pm 0.05	0.54
17	690 \pm 25	1.14 \pm 0.02	9.84 \pm 0.08	10.28 \pm 0.09	1.10
19	550 \pm 110	2.37 \pm 0.16	12.16 \pm 0.41	13.4 \pm 0.5	2.26
20	640 \pm 30	1.22 \pm 0.02	10.48 \pm 0.1	11.4 \pm 0.12	1.19
21	620 \pm 36	1.09 \pm 0.02	10.71 \pm 0.1	11.17 \pm 0.15	1.20
22	610 \pm 92	0.84 \pm 0.04	14.02 \pm 0.16	14.24 \pm 0.21	0.77
23	570 \pm 50	0.64 \pm 0.02	11.39 \pm 0.06	11.79 \pm 0.07	0.57
24	765 \pm 65	1.51 \pm 0.05	12.47 \pm 0.23	11.86 \pm 0.3	1.53
25	960 \pm 260	1.54 \pm 0.15	13.32 \pm 0.61	13.01 \pm 0.92	1.52
27	720 \pm 130	1.50 \pm 0.09	16.89 \pm 0.46	18.78 \pm 0.66	1.49
28	710 \pm 270	0.66 \pm 0.09	16.61 \pm 0.25	18.23 \pm 0.31	0.52
31	620 \pm 140	0.94 \pm 0.07	19.2 \pm 0.28	21.09 \pm 0.41	0.88
34	1280 \pm 580	0.76 \pm 0.15	15.49 \pm 0.26	18.32 \pm 0.4	0.35
35	610 \pm 47	0.92 \pm 0.02	13.16 \pm 0.11	14.26 \pm 0.14	0.82
45	610 \pm 46	0.79 \pm 0.02	10.67 \pm 0.07	11.24 \pm 0.09	0.72
46	510 \pm 57	0.60 \pm 0.02	10.36 \pm 0.07	10.87 \pm 0.09	0.59
54	660 \pm 56	0.51 \pm 0.02	10.94 \pm 0.05	11.19 \pm 0.06	0.44
66	490 \pm 70	0.50 \pm 0.03	11.34 \pm 0.07	11.6 \pm 0.08	0.48
70	690 \pm 33	1.05 \pm 0.02	11.2 \pm 0.08	11.56 \pm 0.11	0.96
72	620 \pm 29	1.07 \pm 0.02	10.75 \pm 0.08	11.03 \pm 0.1	1.06
74	570 \pm 20	0.83 \pm 0.01	10.38 \pm 0.04	10.8 \pm 0.05	0.79
76	680 \pm 26	1.26 \pm 0.02	10.33 \pm 0.09	10.73 \pm 0.1	1.28
78	650 \pm 69	0.59 \pm 0.02	10.54 \pm 0.06	11.06 \pm 0.07	0.49
79	690 \pm 59	2.59 \pm 0.06	10.6 \pm 0.19	10.86 \pm 0.24	2.72
80	619 \pm 23	1.05 \pm 0.01	9.71 \pm 0.06	9.86 \pm 0.08	0.98
81	616 \pm 46	0.57 \pm 0.02	7.52 \pm 0.04	8.05 \pm 0.06	0.50

^a Values at 500 MHz. ^b Values at 600 MHz. ^c ^{15}N $\Delta\omega_{\text{titration}}$ values were calculated as the difference between apo and RA-GEF2 saturated PDZ2.

chemical exchange only arises from peptide binding dynamics, leading to tight correlations between $\Delta\omega_{\text{CPMG}}$ and $\Delta\omega_{\text{titration}}$ (Figure 4.4C,D). As some PDZ domains are known to change their shape [14, 119], future studies of apo dynamics and ligand binding dynamics on the μs -ms timescale should help to determine how common alternative conformational states in PDZ domains are.

For clean two-site exchange, it is reasonable to expect the on-rate for peptide binding (k_{on}) to approach the diffusion limit. To test this, we calculated k_{on} and k_{off} from the dependence of k_{ex} on peptide concentration. To this end, an additional set of relaxation dispersion data were collected with 50% RA-GEF2. The higher ligand concentration pushed exchange rates into the intermediate regime and hence many resonances disappeared. Nevertheless, enough relaxation dispersion curves were obtained to perform global fitting (Table 4.8). Solving the two linear equations (eq. 4) at the two

Table 4.8: Global fitting results of 50% RA-GEF2 bound PDZ2 relaxation dispersion data

Residue	k_{ex} (s^{-1})	$\Delta\omega_{\text{CPMG}}$ (ppm)	$[P_A]$ (%)	$^a R_{20}$ (s^{-1})	$^c \Delta\omega_{\text{titration}}$ (ppm)
11	554±42	0.40±0.03	56.5±0.13	10±0.13	0.38
17	554±42	0.89±0.03	56.5±0.13	0.48±0.04	0.92
23	554±42	0.92±0.07	56.5±0.13	12.38±0.56	0.50
35	554±42	0.98±0.02	56.5±0.13	0.46±0.03	0.92
39	554±42	0.30±0.03	56.5±0.13	11.19±0.12	0.27
66	554±42	0.99±0.05	56.5±0.13	n ^c	0.43
74	554±42	0.25±n	56.5±0.13	n ^c	0.96

^a Values for 500 MHz field. ^b The experimental $\delta\omega$ s were calculated from apo and RA-GEF2 saturated PDZ2. ^c No reasonable fitting values can be obtained.

peptide concentrations (using globally determined k_{ex}), the on-rate was determined to be $3.6 \times 10^7 \text{ s}^{-1} \text{M}^{-1}$, which is approaching the diffusion limit, and the off-rate is 307 s^{-1} , which is very similar to the previously reported value, $270 \pm 20 \text{ s}^{-1}$. [139].

4.4 Summary

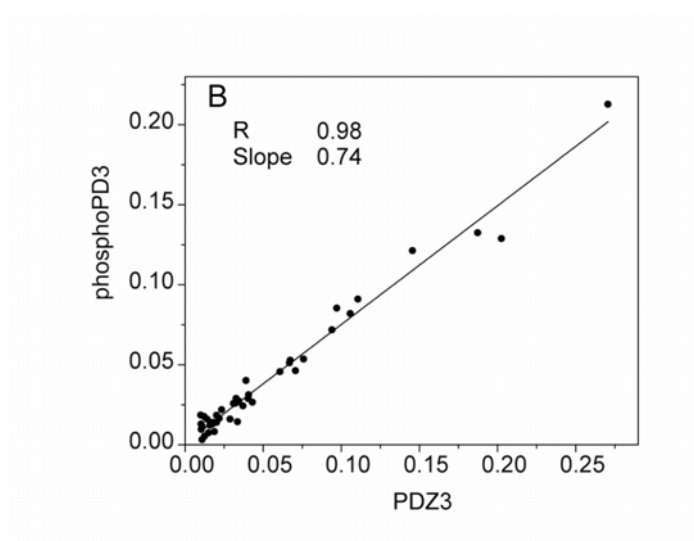
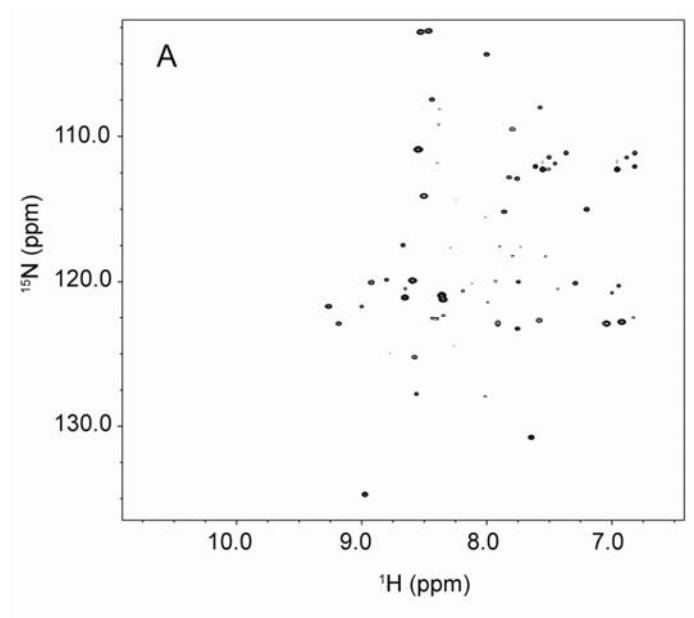
Taken together, the X-ray and NMR results reported here on RA-GEF2 and APC peptides are inconsistent with an induced-fit or conformational selection mechanism of binding to PDZ2, and highly consistent with binding via “lock-and-key”. No significant changes in PDZ2 coordinates are observed between the apo and RA-GEF2 peptide bound

crystal structures, which is supported further by ^1H - ^{15}N RDCs. The absence of significant CPMG relaxation dispersion for apo (or peptide bound) PDZ2 is consistent with lack of conformational change in the crystal structures. We note, however, that a caveat of the relaxation dispersion experiments is that processes faster than $\sim 100\ \mu\text{s}$ are not detected and hence sampling of intermediate binding states on a timescale faster than this cannot be excluded. In the context of this “rigid” PDZ2 domain, binding of both RA-GEF2 and APC peptides induce very similar patterns of changes in ps-ns side-chain dynamic fluctuations that propagate away from the binding site, forming apparent allosteric pathways. Thus, the primary physical impact of peptide binding to PDZ2 is dynamic and not structural in nature. This has implications for understanding the physical basis for long-range communication and allostery in proteins.

4.5 Acknowledgements

The authors of the paper thank Karl Koshlap of the UNC School of Pharmacy NMR facility and Greg Young of the UNC Biomolecular NMR Laboratory for technical assistance. We also thank Dan Cline for assistance with peptide synthesis and purification, and Howard Robinson (at BNL) for X-ray diffraction data collection. Use of the National Synchrotron Light Source, Brookhaven National Laboratory, was supported by the U.S. Department of Energy, Office of Science, Office of Basic Energy Sciences, under Contract No. DE-AC02-98CH10886.

Appendices



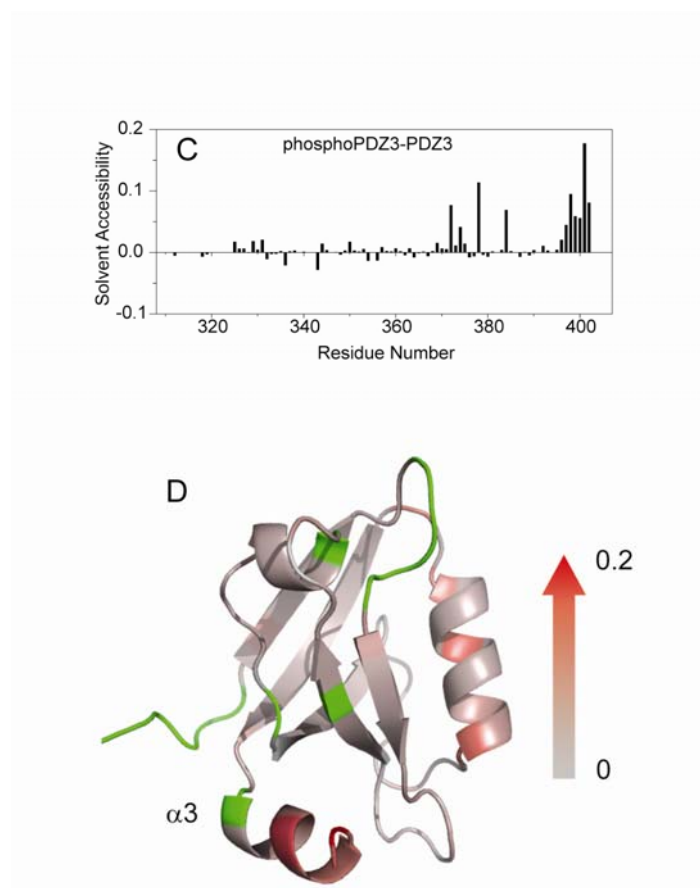


Figure S2.1: Solvent accessibility analysis by NMR. (A) SEA-HSQC spectrum of PDZ3. Only solvent exposed amides yield intense peaks in the SEA-HSQC spectrum (compare with normal HSQC in Fig 1A). (B) Correlation plot of PDZ3 and phosphoPDZ3 SEA-HSQC intensities. Only the residues which are minimally perturbed by phosphorylation (the ones have CPS < 0.05 ppm in Fig. 2A) are selected to make the plot. The scaling factor of 0.74 was obtained from the slope of the line. (C) The solvent accessibility changes by phosphorylation with reference to PDZ3 were plotted onto PDZ3 crystal structure using color scale. The Y397 was shown in stick model.

Table S4.1: Global fitting results of 5% RA-GEF2 bound PDZ2 relaxation dispersion data						
Residue	k_{ex} (s ⁻¹)	$\Delta\omega_{\text{CPMG}}$ (ppm)	$[P_A]$ (%)	^a R_{20} (s ⁻¹)	^b R_{20} (s ⁻¹)	^c $\Delta\omega_{\text{titration}}$ (ppm)
17	320.53±11.79	0.97±0.03	94.7±0.2	9.99±0.11	10.55±0.1	0.92
19	320.53±11.79	2.32±0.20	94.7±0.2	12.75±0.56	13.29±0.42	2.16
20	320.53±11.79	1.67±0.06	94.7±0.2	10.38±0.18	11.41±0.14	1.59
21	320.53±11.79	1.15±0.04	94.7±0.2	10.61±0.17	11.3±0.14	1.20
22	320.53±11.79	0.43±0.12	94.7±0.2	14.74±0.31	14.5±0.21	0.28
23	320.53±11.79	0.48±0.03	94.7±0.2	10.79±0.1	11.74±0.1	0.50
24	320.53±11.79	0.60±0.06	94.7±0.2	12.45±0.25	12.66±0.2	0.50
27	320.53±11.79	1.33±0.14	94.7±0.2	17.17±0.64	20.12±0.53	1.27
31	320.53±11.79	0.87±0.11	94.7±0.2	19.32±0.54	20.61±0.41	0.71
34	320.53±11.79	0.77±0.09	94.7±0.2	15.11±0.29	18.21±0.41	0.50
35	320.53±11.79	1.10±0.05	94.7±0.2	12.73±0.19	13.98±0.18	0.92
40	320.53±11.79	0.54±0.02	94.7±0.2	9.59±0.09	10.06±0.08	0.50
45	320.53±11.79	0.80±0.03	94.7±0.2	10.45±0.12	11.19±0.11	0.71
66	320.53±11.79	0.48±0.03	94.7±0.2	10.9±0.1	11.54±0.1	0.43
67	320.53±11.79	0.58±0.02	94.7±0.2	9.82±0.06	10.53±0.05	0.52
70	320.53±11.79	1.07±0.04	94.7±0.2	11.1±0.14	11.69±0.12	0.93
71	320.53±11.79	0.50±0.03	94.7±0.2	12.95±0.12	13.38±0.1	0.36
72	320.53±11.79	1.29±0.05	94.7±0.2	10.91±0.16	11.18±0.13	1.28
74	320.53±11.79	1.06±0.03	94.7±0.2	10.05±0.08	10.69±0.09	0.96
75	320.53±11.79	0.88±0.02	94.7±0.2	10.52±0.07	11.02±0.07	0.81
76	320.53±11.79	0.90±0.03	94.7±0.2	10.05±0.1	11.1±0.08	0.85
79	320.53±11.79	2.52±0.10	94.7±0.2	11.22±0.21	11.81±0.19	2.55
80	320.53±11.79	0.86±0.03	94.7±0.2	9.4±0.09	9.88±0.09	0.82
81	320.53±11.79	0.49±0.03	94.7±0.2	7.78±0.07	7.87±0.06	0.36
82	320.53±11.79	0.59±0.05	94.7±0.2	14.03±0.22	13.72±0.18	0.52
86	320.53±11.79	0.46±0.03	94.7±0.2	10.72±0.09	11.32±0.08	0.35

^a Values at 500 MHz. ^b Values at 600 MHz. ^c The experimental $\Delta\omega_{\text{titration}}$ values were calculated as the difference between apo and RA-GEF2 saturated PDZ2.

Table S4.2: Global fitting results of 5% APC bound PDZ2 relaxation dispersion data						
Residue	k_{ex} (s ⁻¹)	$\Delta\omega_{\text{CPMG}}$ (ppm)	$[P_A]$ (%)	$^a R_{20}$ (s ⁻¹)	$^b R_{20}$ (s ⁻¹)	$^c \Delta\omega_{\text{titration}}$ (ppm)
11	534 ±17	0.452 ±0.02	94.5 ±0.3	10.05 ±0.06	10.49 ±0.07	0.54
17	534 ±17	1.146 ±0.037	94.5 ±0.3	9.88 ±0.09	10.41 ±0.09	1.10
19	534 ±17	2.184 ±0.143	94.5 ±0.3	12.23 ±0.49	13.86 ±0.48	2.26
20	534 ±17	1.255 ±0.04	94.5 ±0.3	10.44 ±0.11	11.43 ±0.13	1.19
23	534 ±17	0.624 ±0.023	94.5 ±0.3	11.38 ±0.07	11.78 ±0.08	0.57
24	534 ±17	1.591 ±0.076	94.5 ±0.3	12.5 ±0.27	12.05 ±0.32	1.53
27	534 ±17	1.585 ±0.124	94.5 ±0.3	16.88 ±0.54	18.98 ±0.59	1.49
28	534 ±17	0.589 ±0.065	94.5 ±0.3	16.67 ±0.25	18.34 ±0.33	0.52
31	534 ±17	0.925 ±0.077	94.5 ±0.3	19.23 ±0.37	21.18 ±0.42	0.88
35	534 ±17	0.904 ±0.032	94.5 ±0.3	13.18 ±0.11	14.3 ±0.13	0.82
45	534 ±17	0.767 ±0.024	94.5 ±0.3	10.68 ±0.09	11.28 ±0.1	0.72
54	534 ±17	0.478 ±0.019	94.5 ±0.3	10.96 ±0.06	11.24 ±0.06	0.44
66	534 ±17	0.495 ±0.024	94.5 ±0.3	11.35 ±0.08	11.57 ±0.08	0.48
70	534 ±17	1.03 ±0.031	94.5 ±0.3	11.25 ±0.09	11.71 ±0.1	0.96
74	534 ±17	0.822 ±0.023	94.5 ±0.3	10.34 ±0.06	10.8 ±0.06	0.79
76	534 ±17	1.293 ±0.042	94.5 ±0.3	10.33 ±0.1	10.82 ±0.11	1.28
78	534 ±17	0.551 ±0.02	94.5 ±0.3	10.58 ±0.07	11.11 ±0.08	0.49
79	534 ±17	2.604 ±0.142	94.5 ±0.3	10.91 ±0.25	11.73 ±0.24	2.72
81	534 ±17	0.534 ±0.016	94.5 ±0.3	7.55 ±0.05	8.11 ±0.05	0.50

^a Values at 500 MHz. ^b Values at 600 MHz. ^c The experimental $\Delta\omega_{\text{titration}}$ values were calculated as the difference between apo and APC saturated PDZ2.

Table S4.3. Residues for which RDCs values were used in Q-factor calculations.		
Apo PDZ2	RA-GEF2 bound	APC bound
7	6	7
8	7	8
10	8	10
11	9	11
12	10	12
15	11	14
16	12	16
17	14	17
22	15	19
23	16	22
24	17	23
26	19	24
27	21	25
31	23	26
33	24	27
34	26	28
36	27	29
37	28	30
38	29	31
39	30	33
47	31	34
48	34	35
49	37	37
50	38	38
51	40	39
56	41	43
57	43	44
58	44	45
59	45	46
62	47	47
63	48	48
66	49	49
67	51	50
69	52	51
70	54	52
71	55	54
72	56	55
73	57	56
74	59	58
76	61	61
78	62	62
79	63	63
80	64	64
81	65	65
85	66	66
87	67	67
88	69	69
89	70	70
90	71	71
93	72	72
	74	73
	76	74
	77	76

79	77
80	78
81	79
82	80
86	81
87	85
88	87
89	88
90	89
91	90

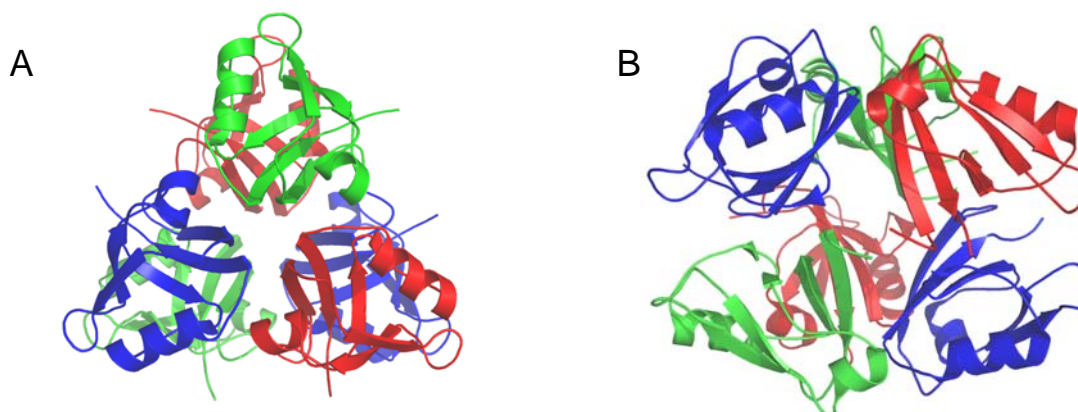


Figure S4.1: Crystal packing within the asymmetric unit for apo PDZ2. (A) top view of the asymmetric unit. The six monomers are colored red, green and blue, and three-blade propeller organization is found. (B) side view of the asymmetric unit. Two layers of three-blade propellers are visible. The figure was prepared using PyMOL.

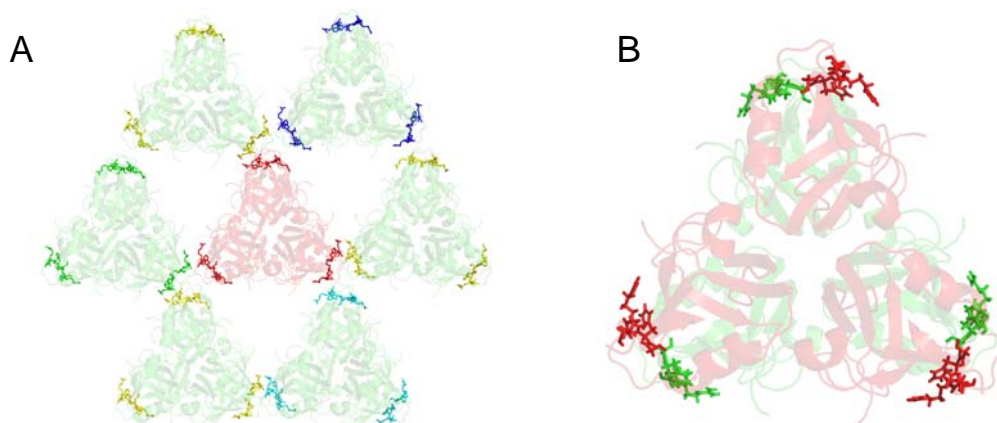


Figure S4.2: Involvement of residue 30-33 in crystal packing. (A) Apo PDZ2 crystal packing. An arbitrary asymmetric unit (colored as red) which contains six apo PDZ2 monomers is selected and six surrounding asymmetric units are also displayed. The fragment 30-33 is shown as stick model and colored the same for the fragment belonging to the same asymmetric unit. (B) RA-GEF2 bound PDZ2 crystal packing. Six molecules belonging to six different adjacent asymmetric units are shown. For clarity, fragment 30-33 was shown as stick and colored differently (red or green) for neighboring molecules. The figure was prepared using PyMOL.

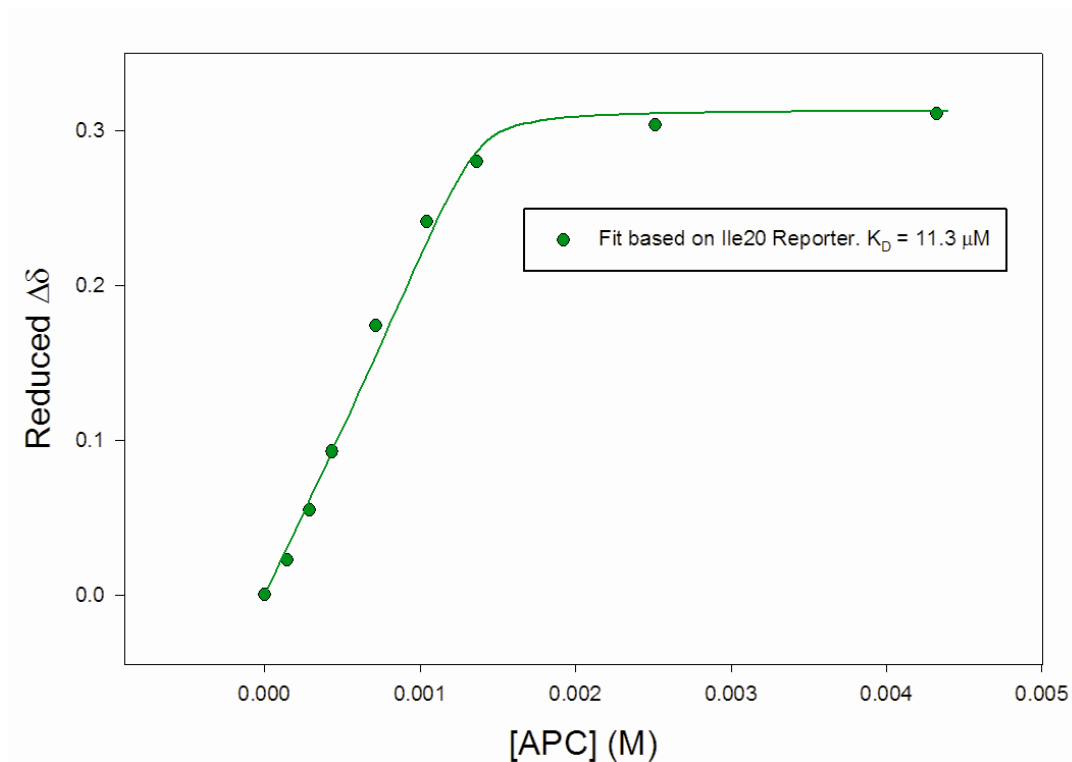


Figure S4.3: Determination of K_D for PDZ2-APC peptide interaction by NMR titration. ^1H - ^{15}N HSQC spectra were acquired at increasing APC:PDZ ratios until no further peak shifts were observed. Only data for the backbone amide at Ile20 are shown, but K_D values for the other reporters are within 10%. The ordinate axis contains the reduced chemical shift difference () between free and APC-bound PDZ as determined from HSQC spectra. The data were then fit to the standard quadratic equation for binding. The apparent irregularities in the fitted/theoretical line are due to changes in PDZ2 concentration during the titration.

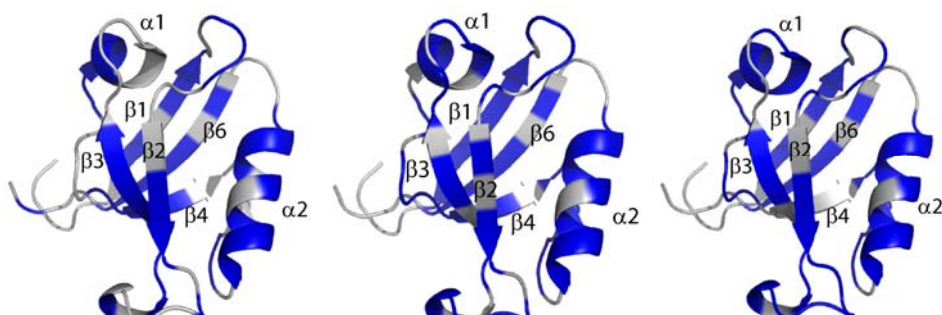


Figure S4.4: Distribution of residues used in calculation of Q-factors (shown in Table 4). Residues for which ^1H - ^{15}N RDC values were used for fitting to structural models are shown in blue on PDZ2. RDC sets are for apo PDZ2 (A), RA-GEF2 bound PDZ2 (B), and APC bound PDZ2. Secondary structural units in PDZ2 are indicated.

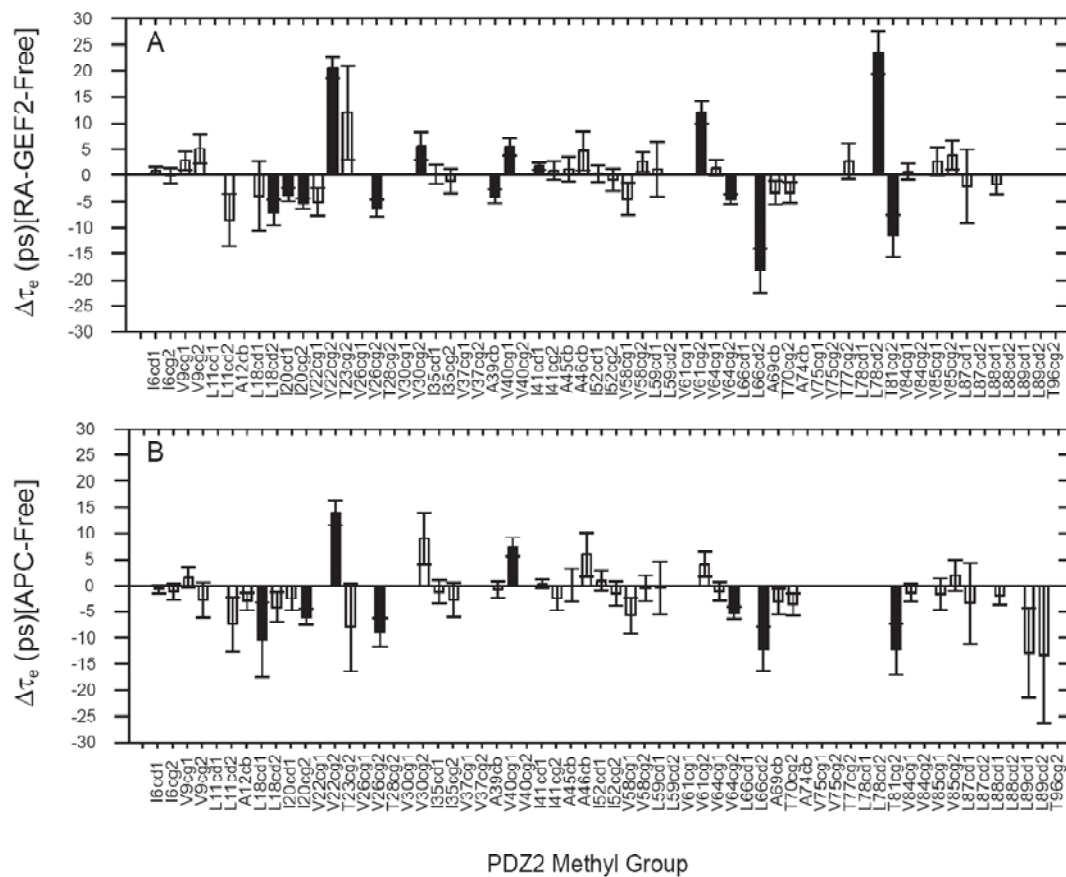


Figure S4.5: Internal correlation time (τ_e) changes induced by RA-GEF2 and APC binding with respect to free PDZ2.

Bibliography

1. Mauldin, R.V., Carroll, M.J., and Lee, A.L. (2009). Dynamic dysfunction in dihydrofolate reductase results from antifolate drug binding: modulation of dynamics within a structural state. *Structure* 17, 386-394.
2. Fuentes, E.J., Der, C.J., and Lee, A.L. (2004). Ligand-dependent dynamics and intramolecular signaling in a PDZ domain. *J Mol Biol* 335, 1105-1115.
3. Fuentes, E.J., Gilmore, S.A., Mauldin, R.V., and Lee, A.L. (2006). Evaluation of energetic and dynamic coupling networks in a PDZ domain protein. *J Mol Biol* 364, 337-351.
4. Kern, D., and Zuiderweg, E.R. (2003). The role of dynamics in allosteric regulation. *Curr Opin Struct Biol* 13, 748-757.
5. Ponting, C.P. (1997). Evidence for PDZ domains in bacteria, yeast, and plants. *Protein Sci* 6, 464-468.
6. Kim, E., and Sheng, M. (2004). PDZ domain proteins of synapses. *Nat Rev Neurosci* 5, 771-781.
7. Sheng, M., and Sala, C. (2001). PDZ domains and the organization of supramolecular complexes. *Annu Rev Neurosci* 24, 1-29.
8. de Mendoza, A., Suga, H., and Ruiz-Trillo, I. (2010). Evolution of the MAGUK protein gene family in premetazoan lineages. *BMC Evol Biol* 10, 93.
9. Doyle, D.A., Lee, A., Lewis, J., Kim, E., Sheng, M., and MacKinnon, R. (1996). Crystal structures of a complexed and peptide-free membrane protein-binding domain: molecular basis of peptide recognition by PDZ. *Cell* 85, 1067-1076.
10. Songyang, Z., Fanning, A.S., Fu, C., Xu, J., Marfatia, S.M., Chishti, A.H., Crompton, A., Chan, A.C., Anderson, J.M., and Cantley, L.C. (1997). Recognition of unique carboxyl-terminal motifs by distinct PDZ domains. *Science* 275, 73-77.
11. Harris, B.Z., Hillier, B.J., and Lim, W.A. (2001). Energetic determinants of internal motif recognition by PDZ domains. *Biochemistry* 40, 5921-5930.
12. Harris, B.Z., Lau, F.W., Fujii, N., Guy, R.K., and Lim, W.A. (2003). Role of electrostatic interactions in PDZ domain ligand recognition. *Biochemistry* 42, 2797-2805.
13. van Ham, M., and Hendriks, W. (2003). PDZ domains-glue and guide. *Mol Biol Rep* 30, 69-82.

14. Peterson, F.C., Penkert, R.R., Volkman, B.F., and Prehoda, K.E. (2004). Cdc42 regulates the Par-6 PDZ domain through an allosteric CRIB-PDZ transition. *Mol Cell* 13, 665-676.
15. Zhang, Q., Fan, J.S., and Zhang, M. (2001). Interdomain chaperoning between PSD-95, Dlg, and Zo-1 (PDZ) domains of glutamate receptor-interacting proteins. *J Biol Chem* 276, 43216-43220.
16. Sheng, M., and Hoogenraad, C.C. (2007). The postsynaptic architecture of excitatory synapses: a more quantitative view. *Annu Rev Biochem* 76, 823-847.
17. Anderson, J.M. (1996). Cell signalling: MAGUK magic. *Curr Biol* 6, 382-384.
18. Gyllys, K.H., Fein, J.A., Yang, F., Wiley, D.J., Miller, C.A., and Cole, G.M. (2004). Synaptic changes in Alzheimer's disease: increased amyloid-beta and gliosis in surviving terminals is accompanied by decreased PSD-95 fluorescence. *Am J Pathol* 165, 1809-1817.
19. Lacor, P.N., Buniel, M.C., Chang, L., Fernandez, S.J., Gong, Y., Viola, K.L., Lambert, M.P., Velasco, P.T., Bigio, E.H., Finch, C.E., Krafft, G.A., and Klein, W.L. (2004). Synaptic targeting by Alzheimer's-related amyloid beta oligomers. *J Neurosci* 24, 10191-10200.
20. Sun, Y., Savanenin, A., Reddy, P.H., and Liu, Y.F. (2001). Polyglutamine-expanded huntingtin promotes sensitization of N-methyl-D-aspartate receptors via post-synaptic density 95. *J Biol Chem* 276, 24713-24718.
21. Nakagawa, T., Futai, K., Lashuel, H.A., Lo, I., Okamoto, K., Walz, T., Hayashi, Y., and Sheng, M. (2004). Quaternary structure, protein dynamics, and synaptic function of SAP97 controlled by L27 domain interactions. *Neuron* 44, 453-467.
22. Wang, W., Weng, J., Zhang, X., Liu, M., and Zhang, M. (2009). Creating conformational entropy by increasing interdomain mobility in ligand binding regulation: a revisit to N-terminal tandem PDZ domains of PSD-95. *J Am Chem Soc* 131, 787-796.
23. Hsueh, Y.P., Kim, E., and Sheng, M. (1997). Disulfide-linked head-to-head multimerization in the mechanism of ion channel clustering by PSD-95. *Neuron* 18, 803-814.
24. Hsueh, Y.P., and Sheng, M. (1999). Requirement of N-terminal cysteines of PSD-95 for PSD-95 multimerization and ternary complex formation, but not for binding to potassium channel Kv1.4. *J Biol Chem* 274, 532-536.
25. Topinka, J.R., and Bredt, D.S. (1998). N-terminal palmitoylation of PSD-95 regulates association with cell membranes and interaction with K⁺ channel Kv1.4. *Neuron* 20, 125-134.

26. Fukata, M., Fukata, Y., Adesnik, H., Nicoll, R.A., and Brecht, D.S. (2004). Identification of PSD-95 palmitoylating enzymes. *Neuron* 44, 987-996.
27. Sainlos, M., Tigaret, C., Poujol, C., Olivier, N.B., Bard, L., Breillat, C., Thiolon, K., Choquet, D., and Imperiali, B. (2011). Biomimetic divalent ligands for the acute disruption of synaptic AMPAR stabilization. *Nat Chem Biol* 7, 81-91.
28. Brenman, J.E., Topinka, J.R., Cooper, E.C., McGee, A.W., Rosen, J., Milroy, T., Ralston, H.J., and Brecht, D.S. (1998). Localization of postsynaptic density-93 to dendritic microtubules and interaction with microtubule-associated protein 1A. *J Neurosci* 18, 8805-8813.
29. Qian, Y., and Prehoda, K.E. (2006). Interdomain interactions in the tumor suppressor discs large regulate binding to the synaptic protein GukHolder. *J Biol Chem* 281, 35757-35763.
30. Ballif, B.A., Carey, G.R., Sunyaev, S.R., and Gygi, S.P. (2008). Large-scale identification and evolution indexing of tyrosine phosphorylation sites from murine brain. *J Proteome Res* 7, 311-318.
31. Munton, R.P., Tweedie-Cullen, R., Livingstone-Zatchej, M., Weinandy, F., Waidelich, M., Longo, D., Gehrig, P., Potthast, F., Rutishauser, D., Gerrits, B., Panse, C., Schlapbach, R., and Mansuy, I.M. (2007). Qualitative and quantitative analyses of protein phosphorylation in naive and stimulated mouse synaptosomal preparations. *Mol Cell Proteomics* 6, 283-293.
32. Trinidad, J.C., Specht, C.G., Thalhammer, A., Schoepfer, R., and Burlingame, A.L. (2006). Comprehensive identification of phosphorylation sites in postsynaptic density preparations. *Mol Cell Proteomics* 5, 914-922.
33. Aghazadeh, B., and Rosen, M.K. (1999). Ligand recognition by SH3 and WW domains: the role of N-alkylation in PPII helices. *Chem Biol* 6, R241-246.
34. Mayer, B.J. (2001). SH3 domains: complexity in moderation. *J Cell Sci* 114, 1253-1263.
35. McGee, A.W., Dakoji, S.R., Olsen, O., Brecht, D.S., Lim, W.A., and Prehoda, K.E. (2001). Structure of the SH3-guanylate kinase module from PSD-95 suggests a mechanism for regulated assembly of MAGUK scaffolding proteins. *Mol Cell* 8, 1291-1301.
36. Tavares, G.A., Panepucci, E.H., and Brunger, A.T. (2001). Structural characterization of the intramolecular interaction between the SH3 and guanylate kinase domains of PSD-95. *Mol Cell* 8, 1313-1325.
37. Sweet, E.S., Previtera, M.L., Fernandez, J.R., Charych, E.I., Tseng, C.Y., Kwon, M., Starovoytov, V., Zheng, J.Q., and Firestein, B.L. (2011). PSD-95 alters microtubule dynamics via an association with EB3. *J Neurosci* 31, 1038-1047.

38. Fukunaga, Y., Matsubara, M., Nagai, R., and Miyazawa, A. (2005). The interaction between PSD-95 and Ca²⁺/calmodulin is enhanced by PDZ-binding proteins. *J Biochem* 138, 177-182.
39. Paarmann, I., Lye, M.F., Lavie, A., and Konrad, M. (2008). Structural requirements for calmodulin binding to membrane-associated guanylate kinase homologs. *Protein Sci* 17, 1946-1954.
40. Colledge, M., Dean, R.A., Scott, G.K., Langeberg, L.K., Huganir, R.L., and Scott, J.D. (2000). Targeting of PKA to glutamate receptors through a MAGUK-AKAP complex. *Neuron* 27, 107-119.
41. Hanada, T., Lin, L., Tibaldi, E.V., Reinherz, E.L., and Chishti, A.H. (2000). GAKIN, a novel kinesin-like protein associates with the human homologue of the Drosophila discs large tumor suppressor in T lymphocytes. *J Biol Chem* 275, 28774-28784.
42. Kim, E., Naisbitt, S., Hsueh, Y.P., Rao, A., Rothschild, A., Craig, A.M., and Sheng, M. (1997). GKAP, a novel synaptic protein that interacts with the guanylate kinase-like domain of the PSD-95/SAP90 family of channel clustering molecules. *J Cell Biol* 136, 669-678.
43. Reese, M.L., Dakoji, S., Bredt, D.S., and Dotsch, V. (2007). The guanylate kinase domain of the MAGUK PSD-95 binds dynamically to a conserved motif in MAP1A. *Nat Struct Mol Biol* 14, 155-163.
44. Marcette, J., Hood, I.V., Johnston, C.A., Doe, C.Q., and Prehoda, K.E. (2009). Allosteric control of regulated scaffolding in membrane-associated guanylate kinases. *Biochemistry* 48, 10014-10019.
45. Sabio, G., Arthur, J.S., Kuma, Y., Pegg, M., Carr, J., Murray-Tait, V., Centeno, F., Goedert, M., Morrice, N.A., and Cuenda, A. (2005). p38gamma regulates the localisation of SAP97 in the cytoskeleton by modulating its interaction with GKAP. *Embo J* 24, 1134-1145.
46. Morabito, M.A., Sheng, M., and Tsai, L.H. (2004). Cyclin-dependent kinase 5 phosphorylates the N-terminal domain of the postsynaptic density protein PSD-95 in neurons. *J Neurosci* 24, 865-876.
47. Gardoni, F., Polli, F., Cattabeni, F., and Di Luca, M. (2006). Calcium-calmodulin-dependent protein kinase II phosphorylation modulates PSD-95 binding to NMDA receptors. *Eur J Neurosci* 24, 2694-2704.
48. Collins, M.O., Yu, L., Coba, M.P., Husi, H., Campuzano, I., Blackstock, W.P., Choudhary, J.S., and Grant, S.G. (2005). Proteomic analysis of in vivo phosphorylated synaptic proteins. *J Biol Chem* 280, 5972-5982.

49. Sabio, G., Reuver, S., Feijoo, C., Hasegawa, M., Thomas, G.M., Centeno, F., Kuhlendahl, S., Leal-Ortiz, S., Goedert, M., Garner, C., and Cuenda, A. (2004). Stress- and mitogen-induced phosphorylation of the synapse-associated protein SAP90/PSD-95 by activation of SAPK3/p38gamma and ERK1/ERK2. *Biochem J* 380, 19-30.
50. de Arce, K.P., Varela-Nallar, L., Farias, O., Cifuentes, A., Bull, P., Couch, B.A., Koleske, A.J., Inestrosa, N.C., and Alvarez, A.R. Synaptic clustering of PSD-95 is regulated by c-Abl through tyrosine phosphorylation. *J Neurosci* 30, 3728-3738.
51. Abaan, O.D., and Toretzky, J.A. (2008). PTPL1: a large phosphatase with a split personality. *Cancer Metastasis Rev* 27, 205-214.
52. Fayer, M.D. (2009). Dynamics of liquids, molecules, and proteins measured with ultrafast 2D IR vibrational echo chemical exchange spectroscopy. *Annu Rev Phys Chem* 60, 21-38.
53. Michalet, X., Weiss, S., and Jager, M. (2006). Single-molecule fluorescence studies of protein folding and conformational dynamics. *Chem Rev* 106, 1785-1813.
54. Cavanagh, J. (2007). Protein NMR spectroscopy : principles and practice, 2nd Edition (Amsterdam ; Boston: Academic Press).
55. Jarymowycz, V.A., and Stone, M.J. (2006). Fast time scale dynamics of protein backbones: NMR relaxation methods, applications, and functional consequences. *Chem Rev* 106, 1624-1671.
56. Kay, L.E., Torchia, D.A., and Bax, A. (1989). Backbone dynamics of proteins as studied by ¹⁵N inverse detected heteronuclear NMR spectroscopy: application to staphylococcal nuclease. *Biochemistry* 28, 8972-8979.
57. Lipari, G., and Szabo, A. (1982). Model-free approach to the interpretation of nuclear magnetic-resonance relaxation in macromolecules I. Theory and range of validity. *J Am Chem Soc* 104, 4546-4559.
58. Lipari, G., and Szabo, A. (1982). Model-free approach to the interpretation of nuclear magnetic-resonance relaxation in macromolecules II. Analysis of experimental results. *J Am Chem Soc* 104, 4559-4570.
59. Muhandiram, D., Yamazaki, T., Sykes, B., and Kay, L. (1995). Measurement of ²H T1 and T1.rho. Relaxation Times in Uniformly ¹³C-Labeled and Fractionally ²H-Labeled Proteins in Solution. *J Am Chem Soc* 117, 11536-11544.
60. Clarkson, M.W., and Lee, A.L. (2004). Long-range dynamic effects of point mutations propagate through side chains in the serine protease inhibitor eglin c. *Biochemistry* 43, 12448-12458.

61. Frederick, K.K., Marlow, M.S., Valentine, K.G., and Wand, A.J. (2007). Conformational entropy in molecular recognition by proteins. *Nature* *448*, 325-329.
62. Lee, A.L., Kinnear, S.A., and Wand, A.J. (2000). Redistribution and loss of side chain entropy upon formation of a calmodulin-peptide complex. *Nat Struct Biol* *7*, 72-77.
63. Petit, C.M., Zhang, J., Sapienza, P.J., Fuentes, E.J., and Lee, A.L. (2009). Hidden dynamic allostery in a PDZ domain. *Proc Natl Acad Sci U S A* *106*, 18249-18254.
64. Rule, G.S., Hitchens, T.K., and SpringerLink (Online service) (2006). *Fundamentals of protein NMR spectroscopy*. pp. xxvi, 530 p., Springer: Dordrecht.
65. Loria, J.P., Rance, M., and Palmer, A.G., 3rd (1999). A Relaxation-Compensated Carr-Purcell-Meiboom-Gill Sequence for characterizing Chemical Exchange by NMR Spectroscopy. *J Am Chem Soc* *121*, 2331-2332.
66. Mulder, F.A., Mittermaier, A., Hon, B., Dahlquist, F.W., and Kay, L.E. (2001). Studying excited states of proteins by NMR spectroscopy. *Nat Struct Biol* *8*, 932-935.
67. Carver, J.P., and Richards, R.E. (1972). General 2-site solution for chemical exchange produced dependence of T₂ upon Car-Purcell pulse separation. *J Mag Res* *6*, 89.
68. Skrynnikov, N.R., Dahlquist, F.W., and Kay, L.E. (2002). Reconstructing NMR spectra of "invisible" excited protein states using HSQC and HMQC experiments. *J Am Chem Soc* *124*, 12352-12360.
69. Korzhnev, D.M., Religa, T.L., Banachewicz, W., Fersht, A.R., and Kay, L.E. (2010). A transient and low-populated protein-folding intermediate at atomic resolution. *Science* *329*, 1312-1316.
70. Ashcroft, N.W., and Mermin, N.D. (1976). *Solid state physics* (Philadelphia: Saunders College).
71. Otting, G. (2010). Protein NMR using paramagnetic ions. *Annu Rev Biophys* *39*, 387-405.
72. Kosen, P.A. (1989). Spin labeling of proteins. *Methods Enzymol* *177*, 86-121.
73. Clore, G.M., and Iwahara, J. (2009). Theory, practice, and applications of paramagnetic relaxation enhancement for the characterization of transient low-population states of biological macromolecules and their complexes. *Chem Rev* *109*, 4108-4139.

74. Solomon, I. (1955). Relaxation Processes in a System of 2 Spins. *Physical Review* *99*, 559-565.
75. Iwahara, J., and Clore, G.M. (2006). Detecting transient intermediates in macromolecular binding by paramagnetic NMR. *Nature* *440*, 1227-1230.
76. Tang, C., Iwahara, J., and Clore, G.M. (2006). Visualization of transient encounter complexes in protein-protein association. *Nature* *444*, 383-386.
77. Iwahara, J., Schwieters, C.D., and Clore, G.M. (2004). Ensemble approach for NMR structure refinement against (1)H paramagnetic relaxation enhancement data arising from a flexible paramagnetic group attached to a macromolecule. *J Am Chem Soc* *126*, 5879-5896.
78. Iwahara, J., Tang, C., and Marius Clore, G. (2007). Practical aspects of (1)H transverse paramagnetic relaxation enhancement measurements on macromolecules. *J Magn Reson* *184*, 185-195.
79. Putnam, C.D., Hammel, M., Hura, G.L., and Tainer, J.A. (2007). X-ray solution scattering (SAXS) combined with crystallography and computation: defining accurate macromolecular structures, conformations and assemblies in solution. *Q Rev Biophys* *40*, 191-285.
80. Jacques, D.A., and Trewhella, J. (2010). Small-angle scattering for structural biology--expanding the frontier while avoiding the pitfalls. *Protein Sci* *19*, 642-657.
81. Svergun, D.I., and Koch, M.H.J. (2003). Small-angle scattering studies of biological macromolecules in solution. *Reports on Progress in Physics* *66*, 1735-1782.
82. Svergun, D.I. (1999). Restoring low resolution structure of biological macromolecules from solution scattering using simulated annealing. *Biophys J* *76*, 2879-2886.
83. Svergun, D.I., Petoukhov, M.V., and Koch, M.H. (2001). Determination of domain structure of proteins from X-ray solution scattering. *Biophys J* *80*, 2946-2953.
84. Petoukhov, M.V., and Svergun, D.I. (2005). Global rigid body modeling of macromolecular complexes against small-angle scattering data. *Biophys J* *89*, 1237-1250.
85. Petoukhov, M.V., and Svergun, D.I. (2006). Joint use of small-angle X-ray and neutron scattering to study biological macromolecules in solution. *Eur Biophys J* *35*, 567-576.

86. Bernado, P., Mylonas, E., Petoukhov, M.V., Blackledge, M., and Svergun, D.I. (2007). Structural characterization of flexible proteins using small-angle X-ray scattering. *J Am Chem Soc* *129*, 5656-5664.
87. Kuwamoto, S., Akiyama, S., and Fujisawa, T. (2004). Radiation damage to a protein solution, detected by synchrotron X-ray small-angle scattering: dose-related considerations and suppression by cryoprotectants. *J Synchrotron Radiat* *11*, 462-468.
88. Sprang, S.R., Acharya, K.R., Goldsmith, E.J., Stuart, D.I., Varvill, K., Fletterick, R.J., Madsen, N.B., and Johnson, L.N. (1988). Structural changes in glycogen phosphorylase induced by phosphorylation. *Nature* *336*, 215-221.
89. Huse, M., and Kuriyan, J. (2002). The conformational plasticity of protein kinases. *Cell* *109*, 275-282.
90. Aghazadeh, B., Lowry, W.E., Huang, X.Y., and Rosen, M.K. (2000). Structural basis for relief of autoinhibition of the Dbl homology domain of proto-oncogene Vav by tyrosine phosphorylation. *Cell* *102*, 625-633.
91. Pufall, M.A., Lee, G.M., Nelson, M.L., Kang, H.S., Velyvis, A., Kay, L.E., McIntosh, L.P., and Graves, B.J. (2005). Variable control of Ets-1 DNA binding by multiple phosphates in an unstructured region. *Science* *309*, 142-145.
92. Lee, C.W., Ferreon, J.C., Ferreon, A.C., Arai, M., and Wright, P.E. (2010). Graded enhancement of p53 binding to CREB-binding protein (CBP) by multisite phosphorylation. *Proc Natl Acad Sci U S A* *107*, 19290-19295.
93. Funke, L., Dakoji, S., and Brecht, D.S. (2005). Membrane-associated guanylate kinases regulate adhesion and plasticity at cell junctions. *Annu Rev Biochem* *74*, 219-245.
94. Long, J.F., Tochio, H., Wang, P., Fan, J.S., Sala, C., Niethammer, M., Sheng, M., and Zhang, M. (2003). Supramolecular structure and synergistic target binding of the N-terminal tandem PDZ domains of PSD-95. *J Mol Biol* *327*, 203-214.
95. Yan, J., Pan, L., Chen, X., Wu, L., and Zhang, M. (2010). The structure of the harmonin/sans complex reveals an unexpected interaction mode of the two Usher syndrome proteins. *Proc Natl Acad Sci U S A* *107*, 4040-4045.
96. Sohn, J., Grant, R.A., and Sauer, R.T. (2007). Allosteric activation of DegS, a stress sensor PDZ protease. *Cell* *131*, 572-583.
97. Bhattacharya, S., Dai, Z., Li, J., Baxter, S., Callaway, D.J., Cowburn, D., and Bu, Z. (2010). A conformational switch in the scaffolding protein NHERF1 controls autoinhibition and complex formation. *J Biol Chem* *285*, 9981-9994.

98. LaLonde, D.P., Garbett, D., and Bretscher, A. (2010). A regulated complex of the scaffolding proteins PDZK1 and EBP50 with ezrin contribute to microvillar organization. *Mol Biol Cell* 21, 1519-1529.
99. Li, J., Poulikakos, P.I., Dai, Z., Testa, J.R., Callaway, D.J., and Bu, Z. (2007). Protein kinase C phosphorylation disrupts Na⁺/H⁺ exchanger regulatory factor 1 autoinhibition and promotes cystic fibrosis transmembrane conductance regulator macromolecular assembly. *J Biol Chem* 282, 27086-27099.
100. Cao, T.T., Deacon, H.W., Reczek, D., Bretscher, A., and von Zastrow, M. (1999). A kinase-regulated PDZ-domain interaction controls endocytic sorting of the beta2-adrenergic receptor. *Nature* 401, 286-290.
101. Chung, H.J., Huang, Y.H., Lau, L.F., and Huganir, R.L. (2004). Regulation of the NMDA receptor complex and trafficking by activity-dependent phosphorylation of the NR2B subunit PDZ ligand. *J Neurosci* 24, 10248-10259.
102. Chung, H.J., Xia, J., Scannevin, R.H., Zhang, X., and Huganir, R.L. (2000). Phosphorylation of the AMPA receptor subunit GluR2 differentially regulates its interaction with PDZ domain-containing proteins. *J Neurosci* 20, 7258-7267.
103. Massari, S., Vanoni, C., Longhi, R., Rosa, P., and Pietrini, G. (2005). Protein kinase C-mediated phosphorylation of the BGT1 epithelial gamma-aminobutyric acid transporter regulates its association with LIN7 PDZ proteins: a post-translational mechanism regulating transporter surface density. *J Biol Chem* 280, 7388-7397.
104. Parker, L.L., Backstrom, J.R., Sanders-Bush, E., and Shieh, B.H. (2003). Agonist-induced phosphorylation of the serotonin 5-HT_{2C} receptor regulates its interaction with multiple PDZ protein 1. *J Biol Chem* 278, 21576-21583.
105. Popovic, M., Bella, J., Zlatev, V., Hodnik, V., Anderluh, G., Barlow, P.N., Pintar, A., and Pongor, S. (2011). The interaction of Jagged-1 cytoplasmic tail with afadin PDZ domain is local, folding-independent, and tuned by phosphorylation. *J Mol Recognit* 24, 245-253.
106. Hegedus, T., Sessler, T., Scott, R., Thelin, W., Bakos, E., Varadi, A., Szabo, K., Homolya, L., Milgram, S.L., and Sarkadi, B. (2003). C-terminal phosphorylation of MRP2 modulates its interaction with PDZ proteins. *Biochem Biophys Res Commun* 302, 454-461.
107. Tyler, R.C., Peterson, F.C., and Volkman, B.F. (2010). Distal interactions within the par3-VE-cadherin complex. *Biochemistry* 49, 951-957.
108. Stein, E.L., and Chetkovich, D.M. (2010). Regulation of stargazin synaptic trafficking by C-terminal PDZ ligand phosphorylation in bidirectional synaptic plasticity. *J Neurochem* 113, 42-53.

109. Wang, C.K., Pan, L., Chen, J., and Zhang, M. (2010). Extensions of PDZ domains as important structural and functional elements. *Protein Cell* *1*, 737-751.
110. An, Y., Ji, J., Wu, W., Lv, A., Huang, R., and Wei, Y. (2005). A rapid and efficient method for multiple-site mutagenesis with a modified overlap extension PCR. *Appl Microbiol Biotechnol* *68*, 774-778.
111. Bradshaw, J.M., and Waksman, G. (1998). Calorimetric investigation of proton linkage by monitoring both the enthalpy and association constant of binding: application to the interaction of the Src SH2 domain with a high-affinity tyrosyl phosphopeptide. *Biochemistry* *37*, 15400-15407.
112. Seeliger, M.A., Young, M., Henderson, M.N., Pellicena, P., King, D.S., Falick, A.M., and Kuriyan, J. (2005). High yield bacterial expression of active c-Abl and c-Src tyrosine kinases. *Protein Sci* *14*, 3135-3139.
113. Muhandiram, D.R., Kay, L. E. (1994). Gradient-Enhanced Triple-Resonance Three-Dimensional NMR Experiments with Improved Sensitivity. *Journal of Magnetic Resonance, Series B* *103*, 203-216.
114. Xue, Y., Ren, J., Gao, X., Jin, C., Wen, L., and Yao, X. (2008). GPS 2.0, a tool to predict kinase-specific phosphorylation sites in hierarchy. *Mol Cell Proteomics* *7*, 1598-1608.
115. Wishart, D.S., and Sykes, B.D. (1994). The ¹³C chemical-shift index: a simple method for the identification of protein secondary structure using ¹³C chemical-shift data. *J Biomol NMR* *4*, 171-180.
116. Lin, D., Sze, K.H., Cui, Y., and Zhu, G. (2002). Clean SEA-HSQC: a method to map solvent exposed amides in large non-deuterated proteins with gradient-enhanced HSQC. *J Biomol NMR* *23*, 317-322.
117. Sapienza, P.J., and Lee, A.L. (2010). Using NMR to study fast dynamics in proteins: methods and applications. *Curr Opin Pharmacol* *10*, 723-730.
118. Zhang, M., and Wang, W. (2003). Organization of signaling complexes by PDZ-domain scaffold proteins. *Acc Chem Res* *36*, 530-538.
119. Mishra, P., Socolich, M., Wall, M.A., Graves, J., Wang, Z., and Ranganathan, R. (2007). Dynamic scaffolding in a G protein-coupled signaling system. *Cell* *131*, 80-92.
120. Korkin, D., Davis, F.P., Alber, F., Luong, T., Shen, M.Y., Lucic, V., Kennedy, M.B., and Sali, A. (2006). Structural modeling of protein interactions by analogy: application to PSD-95. *PLoS Comput Biol* *2*, e153.

121. Gardoni, F., Marcello, E., and Di Luca, M. (2009). Postsynaptic density-membrane associated guanylate kinase proteins (PSD-MAGUKs) and their role in CNS disorders. *Neuroscience* 158, 324-333.
122. Garner, C.C., Nash, J., and Huganir, R.L. (2000). PDZ domains in synapse assembly and signalling. *Trends Cell Biol* 10, 274-280.
123. Aoki, C., Miko, I., Oviedo, H., Mikeladze-Dvali, T., Alexandre, L., Sweeney, N., and Brecht, D.S. (2001). Electron microscopic immunocytochemical detection of PSD-95, PSD-93, SAP-102, and SAP-97 at postsynaptic, presynaptic, and nonsynaptic sites of adult and neonatal rat visual cortex. *Synapse* 40, 239-257.
124. El-Husseini, A.E., Topinka, J.R., Lehrer-Graiwer, J.E., Firestein, B.L., Craven, S.E., Aoki, C., and Brecht, D.S. (2000). Ion channel clustering by membrane-associated guanylate kinases. Differential regulation by N-terminal lipid and metal binding motifs. *J Biol Chem* 275, 23904-23910.
125. Gardoni, F. (2008). MAGUK proteins: new targets for pharmacological intervention in the glutamatergic synapse. *Eur J Pharmacol* 585, 147-152.
126. Kuhlendahl, S., Spangenberg, O., Konrad, M., Kim, E., and Garner, C.C. (1998). Functional analysis of the guanylate kinase-like domain in the synapse-associated protein SAP97. *Eur J Biochem* 252, 305-313.
127. Kim, M.J., Futai, K., Jo, J., Hayashi, Y., Cho, K., and Sheng, M. (2007). Synaptic accumulation of PSD-95 and synaptic function regulated by phosphorylation of serine-295 of PSD-95. *Neuron* 56, 488-502.
128. Donaldson, L.W., Skrynnikov, N.R., Choy, W.Y., Muhandiram, D.R., Sarkar, B., Forman-Kay, J.D., and Kay, L.E. (2001). Structural characterization of proteins with an attached ATCUN motif by paramagnetic relaxation enhancement NMR spectroscopy. *J Am Chem Soc* 123, 9843-9847.
129. Sober, H.A., and Chemical Rubber Company. (1970). *Handbook of biochemistry; Selected data for molecular biology*, 2d Edition (Cleveland,: Chemical Rubber Co.).
130. Petoukhov, M.V., Konarev, P.V., Kikhney, A.G., and Svergun, D.I. (2007). ATSAS 2.1 - towards automated and web-supported small-angle scattering data analysis. *J. Appl. Cryst.* 40, s223-228.
131. Kleiger, G., Saha, A., Lewis, S., Kuhlman, B., and Deshaies, R.J. (2009). Rapid E2-E3 assembly and disassembly enable processive ubiquitylation of cullin-RING ubiquitin ligase substrates. *Cell* 139, 957-968.
132. Hubbard, S.J., Campbell, S.F., and Thornton, J.M. (1991). Molecular recognition. Conformational analysis of limited proteolytic sites and serine proteinase protein inhibitors. *J Mol Biol* 220, 507-530.

133. Lee, B., and Richards, F.M. (1971). The interpretation of protein structures: estimation of static accessibility. *J Mol Biol* 55, 379-400.
134. Zhang, M. (2007). Scaffold proteins as dynamic switches. *Nat Chem Biol* 3, 756-757.
135. van den Berk, L.C., Landi, E., Walma, T., Vuister, G.W., Dente, L., and Hendriks, W.J. (2007). An allosteric intramolecular PDZ-PDZ interaction modulates PTP-BL PDZ2 binding specificity. *Biochemistry* 46, 13629-13637.
136. Li, J., Callaway, D.J., and Bu, Z. (2009). Ezrin induces long-range interdomain allostery in the scaffolding protein NHERF1. *J Mol Biol* 392, 166-180.
137. Bezprozvanny, I., and Maximov, A. (2001). PDZ domains: More than just a glue. *Proc Natl Acad Sci U S A* 98, 787-789.
138. Lockless, S.W., and Ranganathan, R. (1999). Evolutionarily conserved pathways of energetic connectivity in protein families. *Science* 286, 295-299.
139. Gianni, S., Walma, T., Arcovito, A., Calosci, N., Bellelli, A., Engstrom, A., Travaglini-Allocatelli, C., Brunori, M., Jemth, P., and Vuister, G.W. (2006). Demonstration of long-range interactions in a PDZ domain by NMR, kinetics, and protein engineering. *Structure* 14, 1801-1809.
140. Ota, N., and Agard, D.A. (2005). Intramolecular signaling pathways revealed by modeling anisotropic thermal diffusion. *J Mol Biol* 351, 345-354.
141. Sharp, K., and Skinner, J.J. (2006). Pump-probe molecular dynamics as a tool for studying protein motion and long range coupling. *Proteins* 65, 347-361.
142. Ho, B.K., and Agard, D.A. (2009). Probing the flexibility of large conformational changes in protein structures through local perturbations. *PLoS Comput Biol* 5, e1000343.
143. Kong, Y., and Karplus, M. (2009). Signaling pathways of PDZ2 domain: a molecular dynamics interaction correlation analysis. *Proteins* 74, 145-154.
144. Ho, B.K., and Agard, D.A. (2010). Conserved tertiary couplings stabilize elements in the PDZ fold, leading to characteristic patterns of domain conformational flexibility. *Protein Sci* 19, 398-411.
145. Cooper, A., and Dryden, D.T. (1984). Allostery without conformational change. A plausible model. *Eur Biophys J* 11, 103-109.
146. Kozlov, G., Gehring, K., and Ekiel, I. (2000). Solution structure of the PDZ2 domain from human phosphatase hPTP1E and its interactions with C-terminal peptides from the Fas receptor. *Biochemistry* 39, 2572-2580.

147. Kozlov, G., Banville, D., Gehring, K., and Ekiel, I. (2002). Solution structure of the PDZ2 domain from cytosolic human phosphatase hPTP1E complexed with a peptide reveals contribution of the beta2-beta3 loop to PDZ domain-ligand interactions. *J Mol Biol* 320, 813-820.
148. Walma, T., Spronk, C.A., Tessari, M., Aelen, J., Schepens, J., Hendriks, W., and Vuister, G.W. (2002). Structure, dynamics and binding characteristics of the second PDZ domain of PTP-BL. *J Mol Biol* 316, 1101-1110.
149. Niv, M.Y., and Weinstein, H. (2005). A flexible docking procedure for the exploration of peptide binding selectivity to known structures and homology models of PDZ domains. *J Am Chem Soc* 127, 14072-14079.
150. Basdevant, N., Weinstein, H., and Ceruso, M. (2006). Thermodynamic basis for promiscuity and selectivity in protein-protein interactions: PDZ domains, a case study. *J Am Chem Soc* 128, 12766-12777.
151. Gerek, Z.N., Keskin, O., and Ozkan, S.B. (2009). Identification of specificity and promiscuity of PDZ domain interactions through their dynamic behavior. *Proteins* 77, 796-811.
152. Gerek, Z.N., and Ozkan, S.B. (2010). A flexible docking scheme to explore the binding selectivity of PDZ domains. *Protein Sci* 19, 914-928.
153. Stiffler, M.A., Chen, J.R., Grantcharova, V.P., Lei, Y., Fuchs, D., Allen, J.E., Zaslavskaja, L.A., and MacBeath, G. (2007). PDZ domain binding selectivity is optimized across the mouse proteome. *Science* 317, 364-369.
154. Dev, K.K. (2004). Making protein interactions druggable: targeting PDZ domains. *Nat Rev Drug Discov* 3, 1047-1056.
155. Wang, N.X., Lee, H.J., and Zheng, J.J. (2008). Therapeutic use of PDZ protein-protein interaction antagonism. *Drug News Perspect* 21, 137-141.
156. Jemth, P., and Gianni, S. (2007). PDZ domains: folding and binding. *Biochemistry* 46, 8701-8708.
157. Gianni, S., Geierhaas, C.D., Calosci, N., Jemth, P., Vuister, G.W., Travaglini-Allocatelli, C., Vendruscolo, M., and Brunori, M. (2007). A PDZ domain recapitulates a unifying mechanism for protein folding. *Proc Natl Acad Sci U S A* 104, 128-133.
158. Calosci, N., Chi, C.N., Richter, B., Camilloni, C., Engstrom, A., Eklund, L., Travaglini-Allocatelli, C., Gianni, S., Vendruscolo, M., and Jemth, P. (2008). Comparison of successive transition states for folding reveals alternative early folding pathways of two homologous proteins. *Proc Natl Acad Sci U S A* 105, 19241-19246.

159. Milev, S., Bjelic, S., Georgiev, O., and Jelesarov, I. (2007). Energetics of peptide recognition by the second PDZ domain of human protein tyrosine phosphatase 1E. *Biochemistry* *46*, 1064-1078.
160. Rao, F., and Karplus, M. (2010). Protein dynamics investigated by inherent structure analysis. *Proc Natl Acad Sci U S A*.
161. De Los Rios, P., Cecconi, F., Pretre, A., Dietler, G., Michielin, O., Piazza, F., and Juanico, B. (2005). Functional dynamics of PDZ binding domains: a normal-mode analysis. *Biophys J* *89*, 14-21.
162. Dhulesia, A., Gsponer, J., and Vendruscolo, M. (2008). Mapping of two networks of residues that exhibit structural and dynamical changes upon binding in a PDZ domain protein. *J Am Chem Soc* *130*, 8931-8939.
163. Dreier, L., and Wider, G. (2006). Concentration measurements by PULCON using X-filtered or 2D NMR spectra. *Magn Reson Chem* *44 Spec No*, S206-212.
164. Wider, G., and Dreier, L. (2006). Measuring protein concentrations by NMR spectroscopy. *J Am Chem Soc* *128*, 2571-2576.
165. Dick, F. (1994). Acid cleavage/deprotection in Fmoc/tBu solid-phase peptide synthesis. *Methods Mol Biol* *35*, 63-72.
166. Adams, P.D., Afonine, P.V., Bunkoczi, G., Chen, V.B., Davis, I.W., Echols, N., Headd, J.J., Hung, L.W., Kapral, G.J., Grosse-Kunstleve, R.W., McCoy, A.J., Moriarty, N.W., Oeffner, R., Read, R.J., Richardson, D.C., Richardson, J.S., Terwilliger, T.C., and Zwart, P.H. (2010). PHENIX: a comprehensive Python-based system for macromolecular structure solution. *Acta Crystallogr D Biol Crystallogr* *66*, 213-221.
167. Otwinowski, Z., and Minor, W. (1997). Processing of X-ray diffraction data collected in oscillation mode. *Macromolecular Crystallography, Pt A* *276*, 307-326.
168. (1994). The CCP4 suite: programs for protein crystallography. *Acta Crystallogr D Biol Crystallogr* *50*, 760-763.
169. von Ossowski, I., Oksanen, E., von Ossowski, L., Cai, C., Sundberg, M., Goldman, A., and Keinanen, K. (2006). Crystal structure of the second PDZ domain of SAP97 in complex with a GluR-A C-terminal peptide. *Febs J* *273*, 5219-5229.
170. Murshudov, G.N., Vagin, A.A., and Dodson, E.J. (1997). Refinement of macromolecular structures by the maximum-likelihood method. *Acta Crystallogr D Biol Crystallogr* *53*, 240-255.

171. Adams, P.D., Afonine, P.V., Bunkoczi, G., Chen, V.B., Davis, I.W., Echols, N., Headd, J.J., Hung, L.W., Kapral, G.J., Grosse-Kunstleve, R.W., McCoy, A.J., Moriarty, N.W., Oeffner, R., Read, R.J., Richardson, D.C., Richardson, J.S., Terwilliger, T.C., and Zwart, P.H. PHENIX: a comprehensive Python-based system for macromolecular structure solution. *Acta Crystallogr D Biol Crystallogr* **66**, 213-221.
172. Emsley, P., and Cowtan, K. (2004). Coot: model-building tools for molecular graphics. *Acta Crystallogr D Biol Crystallogr* **60**, 2126-2132.
173. Painter, J., and Merritt, E.A. (2006). TLSMD web server for the generation of multi-group TLS models. *Journal of Applied Crystallography* **39**, 109-111.
174. Delaglio, F., Grzesiek, S., Vuister, G.W., Zhu, G., Pfeifer, J., and Bax, A. (1995). NMRPipe: a multidimensional spectral processing system based on UNIX pipes. *J Biomol NMR* **6**, 277-293.
175. Johnson, B.A., and Blevins, R.A. (1994). NMR View: A computer program for the visualization and analysis of NMR data. *J Biomol NMR* **4**, 603-614.
176. Ottiger, M., Delaglio, F., and Bax, A. (1998). Measurement of J and dipolar couplings from simplified two-dimensional NMR spectra. *J Magn Reson* **131**, 373-378.
177. Sass, H.J., Musco, G., Stahl, S.J., Wingfield, P.T., and Grzesiek, S. (2000). Solution NMR of proteins within polyacrylamide gels: diffusional properties and residual alignment by mechanical stress or embedding of oriented purple membranes. *J Biomol NMR* **18**, 303-309.
178. Valafar, H., and Prestegard, J.H. (2004). REDCAT: a residual dipolar coupling analysis tool. *J Magn Reson* **167**, 228-241.
179. Loria, J.P., Rance, M., and Palmer, A.G., 3rd (1999). A TROSY CPMG sequence for characterizing chemical exchange in large proteins. *J Biomol NMR* **15**, 151-155.
180. Palmer, A.G., 3rd, Kroenke, C.D., and Loria, J.P. (2001). Nuclear magnetic resonance methods for quantifying microsecond-to-millisecond motions in biological macromolecules. *Methods Enzymol* **339**, 204-238.
181. Gao, X., Satoh, T., Liao, Y., Song, C., Hu, C.D., Kariya Ki, K., and Kataoka, T. (2001). Identification and characterization of RA-GEF-2, a Rap guanine nucleotide exchange factor that serves as a downstream target of M-Ras. *J Biol Chem* **276**, 42219-42225.
182. Krissinel, E., and Henrick, K. (2007). Inference of macromolecular assemblies from crystalline state. *J Mol Biol* **372**, 774-797.

183. Krojer, T., Garrido-Franco, M., Huber, R., Ehrmann, M., and Clausen, T. (2002). Crystal structure of DegP (HtrA) reveals a new protease-chaperone machine. *Nature* *416*, 455-459.
184. Andrec, M., Snyder, D.A., Zhou, Z., Young, J., Montelione, G.T., and Levy, R.M. (2007). A large data set comparison of protein structures determined by crystallography and NMR: statistical test for structural differences and the effect of crystal packing. *Proteins* *69*, 449-465.
185. Wang, J., Zuo, X., Yu, P., Byeon, I.J., Jung, J., Wang, X., Dyba, M., Seifert, S., Schwieters, C.D., Qin, J., Gronenborn, A.M., and Wang, Y.X. (2009). Determination of multicomponent protein structures in solution using global orientation and shape restraints. *J Am Chem Soc* *131*, 10507-10515.
186. Bax, A. (2003). Weak alignment offers new NMR opportunities to study protein structure and dynamics. *Protein Sci* *12*, 1-16.
187. Cornilescu, G., and Bax, A. (1998). Validation of Protein Structure from Anisotropic Carbonyl Chemical Shifts in a Dilute Liquid Crystalline Phase. *J Am Chem Soc* *120*, 6836-6837.
188. Cornilescu, G., and Bax, A. (2000). Measurement of Proton, Nitrogen, and Carbonyl Chemical Shielding Anisotropies in a Protein Dissolved in a Dilute Liquid Crystalline Phase. *J Am Chem Soc* *122*, 10143-10154.
189. Stacklies, W., Vega, M.C., Wilmanns, M., and Grater, F. (2009). Mechanical network in titin immunoglobulin from force distribution analysis. *PLoS Comput Biol* *5*, e1000306.
190. Stacklies, W., Xia, F., and Grater, F. (2009). Dynamic allostery in the methionine repressor revealed by force distribution analysis. *PLoS Comput Biol* *5*, e1000574.
191. Whitley, M.J., and Lee, A.L. (2009). Frameworks for understanding long-range intra-protein communication. *Curr Protein Pept Sci* *10*, 116-127.
192. Erdmann, K.S., Kuhlmann, J., Lessmann, V., Herrmann, L., Eulenburg, V., Muller, O., and Heumann, R. (2000). The Adenomatous Polyposis Coli-protein (APC) interacts with the protein tyrosine phosphatase PTP-BL via an alternatively spliced PDZ domain. *Oncogene* *19*, 3894-3901.
193. Smock, R.G., and Gierasch, L.M. (2009). Sending signals dynamically. *Science* *324*, 198-203.
194. Wand, A.J. (2001). Dynamic activation of protein function: a view emerging from NMR spectroscopy. *Nat Struct Biol* *8*, 926-931.
195. Tsai, C.J., del Sol, A., and Nussinov, R. (2008). Allostery: absence of a change in shape does not imply that allostery is not at play. *J Mol Biol* *378*, 1-11.

196. Mittermaier, A., and Kay, L.E. (2006). New tools provide new insights in NMR studies of protein dynamics. *Science* *312*, 224-228.
197. Loria, J.P., Berlow, R.B., and Watt, E.D. (2008). Characterization of enzyme motions by solution NMR relaxation dispersion. *Acc Chem Res* *41*, 214-221.
198. Mittag, T., Schaffhausen, B., and Gunther, U.L. (2003). Direct observation of protein-ligand interaction kinetics. *Biochemistry* *42*, 11128-11136.
199. Mittag, T., Schaffhausen, B., and Gunther, U.L. (2004). Tracing kinetic intermediates during ligand binding. *J Am Chem Soc* *126*, 9017-9023.
200. Tolkatchev, D., Xu, P., and Ni, F. (2003). Probing the kinetic landscape of transient peptide-protein interactions by use of peptide (15)*n* NMR relaxation dispersion spectroscopy: binding of an antithrombin peptide to human prothrombin. *J Am Chem Soc* *125*, 12432-12442.
201. Hansen, D.F., Vallurupalli, P., Lundstrom, P., Neudecker, P., and Kay, L.E. (2008). Probing chemical shifts of invisible states of proteins with relaxation dispersion NMR spectroscopy: how well can we do? *J Am Chem Soc* *130*, 2667-2675.
202. Niu, X., Chen, Q., Zhang, J., Shen, W., Shi, Y., and Wu, J. (2007). Interesting structural and dynamical behaviors exhibited by the AF-6 PDZ domain upon Ber peptide binding. *Biochemistry* *46*, 15042-15053.
203. McElheny, D., Schnell, J.R., Lansing, J.C., Dyson, H.J., and Wright, P.E. (2005). Defining the role of active-site loop fluctuations in dihydrofolate reductase catalysis. *Proc Natl Acad Sci U S A* *102*, 5032-5037.
204. Namanja, A.T., Wang, X.J., Xu, B., Mercedes-Camacho, A.Y., Wilson, B.D., Wilson, K.A., Etzkorn, F.A., and Peng, J.W. (2010). Toward flexibility-activity relationships by NMR spectroscopy: dynamics of Pin1 ligands. *J Am Chem Soc* *132*, 5607-5609.
205. Korzhnev, D.M., Neudecker, P., Mittermaier, A., Orekhov, V.Y., and Kay, L.E. (2005). Multiple-site exchange in proteins studied with a suite of six NMR relaxation dispersion experiments: an application to the folding of a Fyn SH3 domain mutant. *J Am Chem Soc* *127*, 15602-15611.